MODELING AND ANALYSIS OF RESERVOIR RESPONSE TO STIMULATION BY WATER INJECTION

A Thesis

by

JUN GE

Submitted to the Office of Graduate Studies of
Texas A&M University
in partial fulfillment of the requirements for the degree of

MASTER OF SCIENCE

December 2009

Major Subject: Petroleum Engineering

MODELING AND ANALYSIS OF RESERVOIR RESPONSE TO STIMULATION BY WATER INJECTION

A Thesis

by

JUN GE

Submitted to the Office of Graduate Studies of
Texas A&M University
in partial fulfillment of the requirements for the degree of

MASTER OF SCIENCE

Approved by:

Chair of Committee,	Ahmad Ghassemi
Committee Members,	Stephen A. Holditch
	Benchun Duan
Head of Department,	Stephen A. Holditch

December 2009

Major Subject: Petroleum Engineering

ABSTRACT

Modeling and Analysis of Reservoir Response to Stimulation by Water Injection.

(December 2009)

Jun Ge, B.S., China University of Geosciences;

M.S., Peking University

Chair of Advisory Committee: Dr. Ahmad Ghassemi

The distributions of pore pressure and stresses around a fracture are of interest in conventional hydraulic fracturing operations, fracturing during water-flooding of petroleum reservoirs, shale gas, and injection/extraction operations in a geothermal reservoir. During the operations, the pore pressure will increase with fluid injection into the fracture and leak off to surround the formation. The pore pressure increase will induce the stress variations around the fracture surface. This can cause the slip of weakness planes in the formation and cause the variation of the permeability in the reservoir. Therefore, the investigation on the pore pressure and stress variations around a hydraulic fracture in petroleum and geothermal reservoirs has practical applications.

The stress and pore pressure fields around a fracture are affected by: poroelastic, thermoelastic phenomena as well as by fracture opening under the combined action of applied pressure and in-situ stress.

In our study, we built up two models. One is a model (WFPSD model) of water-flood induced fracturing from a single well in an infinite reservoir. WFPSD model calculates the length of a water flood fracture and the extent of the cooled and flooded

zones. The second model (FracJStim model) calculates the stress and pore pressure distribution around a fracture of a given length under the action of applied internal pressure and in-situ stresses as well as their variation due to cooling and pore pressure changes. In our FracJStim model, the Structural Permeability Diagram is used to estimate the required additional pore pressure to reactivate the joints in the rock formations of the reservoir. By estimating the failed reservoir volume and comparing with the actual stimulated reservoir volume, the enhanced reservoir permeability in the stimulated zone can be estimated.

In our research, the traditional two dimensional hydraulic fracturing propagation models are reviewed, the propagation and recession of a poroelastic PKN hydraulic fracturing model are studied, and the pore pressure and stress distributions around a hydraulically induced fracture are calculated and plotted at a specific time. The pore pressure and stress distributions are used to estimate the failure potentials of the joints in rock formations around the hydraulic fracture. The joint slips and rock failure result in permeability change which can be calculated under certain conditions. As a case study and verification step, the failure of rock mass around a hydraulic fracture for the stimulation of Barnett Shale is considered.

With the simulations using our models, the pore pressure and poro-induced stresses around a hydraulic fracture are elliptically distributed near the fracture. From the case study on Barnett Shale, the required additional pore pressure is about 0.06 psi/ft. With the given treatment pressure, the enhanced permeability after the stimulation of hydraulic fracture is calculated and plotted. And the results can be verified by previous work by Palmer, Moschovidis and Cameron in 2007.

DEDICATION

To my Family

ACKNOWLEDGEMENTS

I would like to express my deep and sincere gratitude to my advisor, Dr. Ahmad Ghassemi, for his support, guidance, encouragement and patience throughout the completion of this research project. Dr. Ghassemi introduced me to the field of Petroleum Rock Mechanics and provided me with the opportunity to learn and to do research on the hydraulic fracture. I specially thank him for his patience and careful review of this thesis. I would also like to thank Dr. Stephen A. Holditch and Dr. Benchun Duan for kindly serving as committee members and reviewing this thesis.

I would like to thank my wife, Yu Zhong, for her support throughout the course of my study. Thanks also go to my friends and colleagues in the finishing of my thesis and the department faculty and staff for making my time at Texas A&M University a great experience. I would especially like to thank my friends and colleagues including Qingfeng Tao, Chakra Rawal, Jian Huang, Wenxu Xue, Dr. Zhengnan Zhang and Dr. Xiaoxian Zhou. I really appreciate their help on my study.

Great appreciation goes to the Crisman Institute for support of this research. I also want to extend my gratitude to Texas A&M University, DOE, for providing me with financial assistance.

I thank God for empowering and guiding me throughout the completion of the degree.

TABLE OF CONTENTS

Page

Page

LIST OF FIGURES

Page

Page

Page

LIST OF TABLES

Page

1 INTRODUCTION

1.1 Hydraulic Fracturing

Hydraulic fracturing is a widely used stimulation technique to initiate a high permeability conduit of gas in a low permeability reservoir. During the hydraulic fracturing operation, a fluid is injected into a well at a pressure high enough to fracture the formation. The process also can cause opening up of natural fractures already present in the formation.

For the past 50 years, the technique of hydraulic fracturing has been widely used in energy industry. One of the most important applications of this technique is the stimulation of hydrocarbon wells for increasing oil and gas recovery (e.g., Veatch, 1983a, 1983b; Yew, 1997; Economides and Nolte, 2000). More than 70% of the gas wells and 50% of the oil wells in North America are stimulated using hydraulic fracturing (e.g., Valko and Economides 1995). Hydraulic fracturing can also be applied in the in situ stress measurement (e.g., Haimson, 1978; Shin *et al.*, 2001), and geothermal reservoir stimulations (e.g., Murphy, 1983; Legarth, Huenges, and Zimmermann 2005; Nygren and Ghassemi 2005).

Currently, the most important application of hydraulic fracturing technique is to stimulate the low permeability gas reservoirs. As the economies of most nations in the world continue to expand and the demand for energy continues to increase, more and more unconventional oil and gas resources are being developed to meet the demands for energy.

This thesis follows the style of *SPE Journal.*

Tight gas reservoirs, including tight gas sandstones (TG), gas shale (GS), and coal-bed methane (CBM), are typical unconventional gas resources that are accumulated in low-permeability geologic environments. In the 1970s, the United States government defined a tight gas reservoir as a reservoir with an expected value of permeability to gas flow of 0.1 md or less. Holditch (2006) defined a tight gas reservoir as "a reservoir that cannot produce at economical rates nor recover economic volumes of natural gas unless the well is stimulated by a larger hydraulic fracture treatment or produced by use of a horizontal wellbore or multilateral wellbores." Hydraulic fracturing is an efficient technique to enhance productions from these low permeability reservoirs.

Another application of hydraulic fracturing is to stimulate geothermal production. The production of geothermal energy from dry and low permeability reservoirs is achieved by water circulation in natural and/or man-made fractures, and is often referred to as enhanced or engineered geothermal systems (EGS) (MIT-Lead Report).

In hydraulic fracturing operations, the fracture fluid which is injected into the well can be oil-based, water-based, or acid-based (Veatch, 1983a, 1983b). However, water based hydraulic fracturing are the most common used and the least expensive. Slick-water fracturing combines water with a friction-reducing chemical additive which allows the water to be pumped at higher injection rates into the formation (Palisch *et al.*, 2008).

The process of a hydraulic fracturing operation is shown in Fig.1.1 (Veatch, 1983a). It consists of blending special chemicals to make the appropriate fracturing fluid and then pumping the blended fluid into the pay zone at high enough rates and pressures to wedge and extend a fracture hydraulically (Gidley *et al*. 1989).

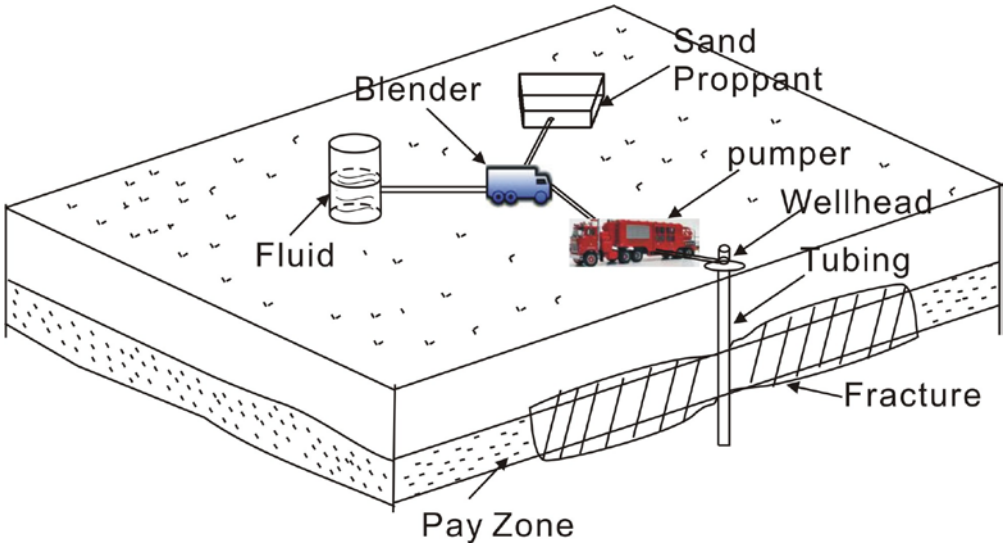

Fig.1.1 Hydraulic Fracturing Process

1.2 Fracture Mechanics

During the process of hydraulic fracturing, rock mechanics plays an important role in governing the geometry of propagating fractures (Gidley *et al*., 1989). It is important to understand the mechanisms of fluid-rock interaction in the hydraulic fracturing. In real operations, fractures can be more complicated in Geometry, and we can have complex fracturing and extremely complex fracturing in work (Fig.1.2). The long axis of the fracture network or "fairway" is referred to as the hydraulic fracture "fairway length" while the short axis is typically referred to as "fairway width" (Fisher *et al*., 2004). The volume of this fairway or the stimulated volume can be estimated using the rock mechanics methods for the hydraulic fractures. To do this, it is necessary to know the pore pressure and stress distribution around the fracture or stimulated interval which varies with the geometry of hydraulic fractures, and is affected by mechanical, thermal, and chemical conditions of the surrounding host rock, especially the mechanical properties.

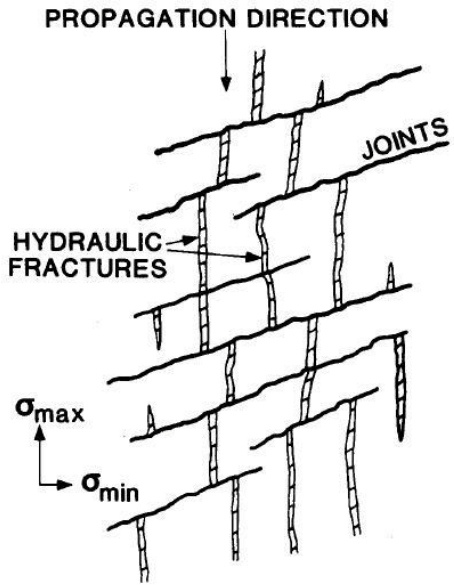

Fig.1.2 Geometry of Fracture Network (Modified from Warpinski and Teufel, 1987)

According to previous studies (Gidley *et al*., 1989), some important factors that have effects on fracture propagation include:

1) In situ stresses existing in rock: the local stress fields and variations in stresses between adjacent formations are often though to dominate fracture orientation and fracture growth. A hydraulic fracture will propagate perpendicular to the minimum principal stress.
2) Relative bed thickness of formations in the vicinity of the fracture.
3) Mechanical rock properties: such properties as elastic modulus, Poisson's ratio, and toughness will affect the fracture propagation.
4) Fluid pressure gradients in the fracture.
5) Pore pressure distributions in the formation.

1.3 Fracture Propagation Models

Over the past 50 years, many models have been developed to study fracture propagation, including two-dimensional (Perkins and Kern 1961; Geertsma and Klerk, 1969; Nordgren, 1972; Daneshy, 1973) and three dimensional models (Clifton in Gidley *et al*., 1989). For my research, the traditional 2-D models of the fluid driven fracturing process are reviewed.

1.3.1 PKN Model

Perkins and Kern (1961) developed equations to compute fracture length and width for a fixed height. Later Nordgren (1972) improved their model by adding fluid loss to the solution. The PKN model makes the assumption that the fracture has a constant height and an elliptical cross section (Fig.1.3) in both the horizontal plane and the vertical plane.

From the view of solid mechanics, the fracture height, h_f, is independent of the distance to which it has propagated away from the well. The problem is reduced to 2D by using the plane strain assumption. For the PKN model, plane strain is considered in the vertical direction, and the rock response in each vertical section along the x-direction is assumed independent of its neighboring vertical planes. Plain strain implies that the elastic deformations (strains) to open or close, or shear the fracture are fully concentrated in the vertical planes sections perpendicular to the direction of fracture propagation.

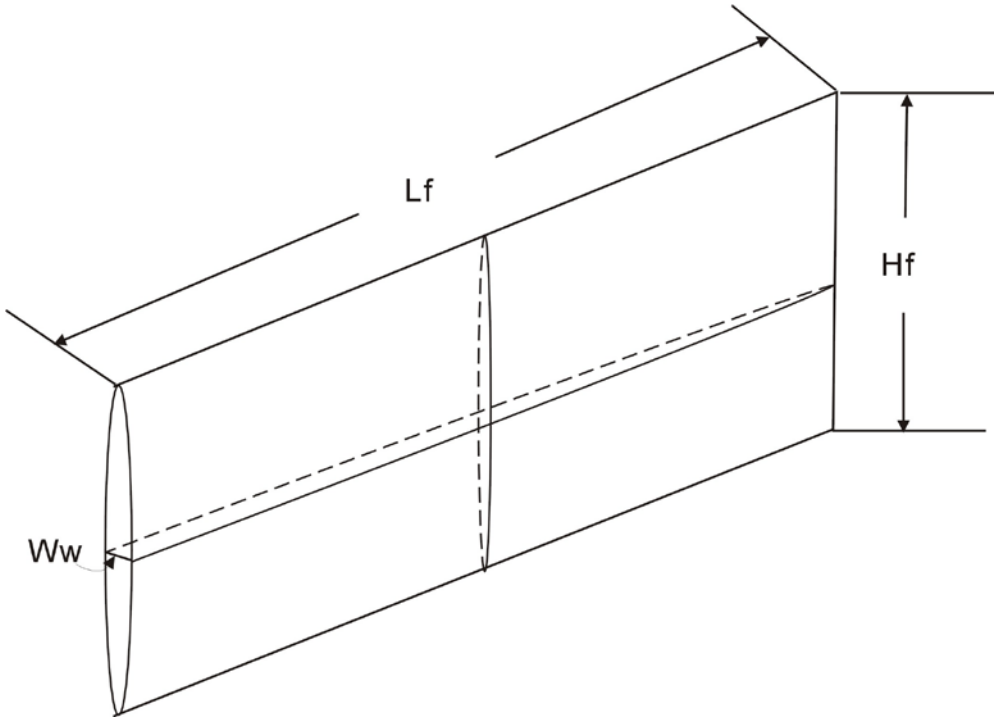

Fig.1.3 Geometry of PKN Model

From the view of fluid mechanics, the fluid flow problem in the PKN model is considered in one dimension in an elliptical channel. The fluid pressure, p_f, is assumed constant in each vertical cross section perpendicular to the direction of propagation.

1.3.2 KGD Model

The KGD model was developed by Khristianovic and Zheltov (1955) and Geertsma and de Klerk (1969). In this model, the fracture deformation and propagation are assumed to evolve in a situation of plane strain. The model also assumes that the fluid flow and the fracture propagation are one dimension. The geometry of a traditional KGD fracture propagation model is shown in Fig.1.4.

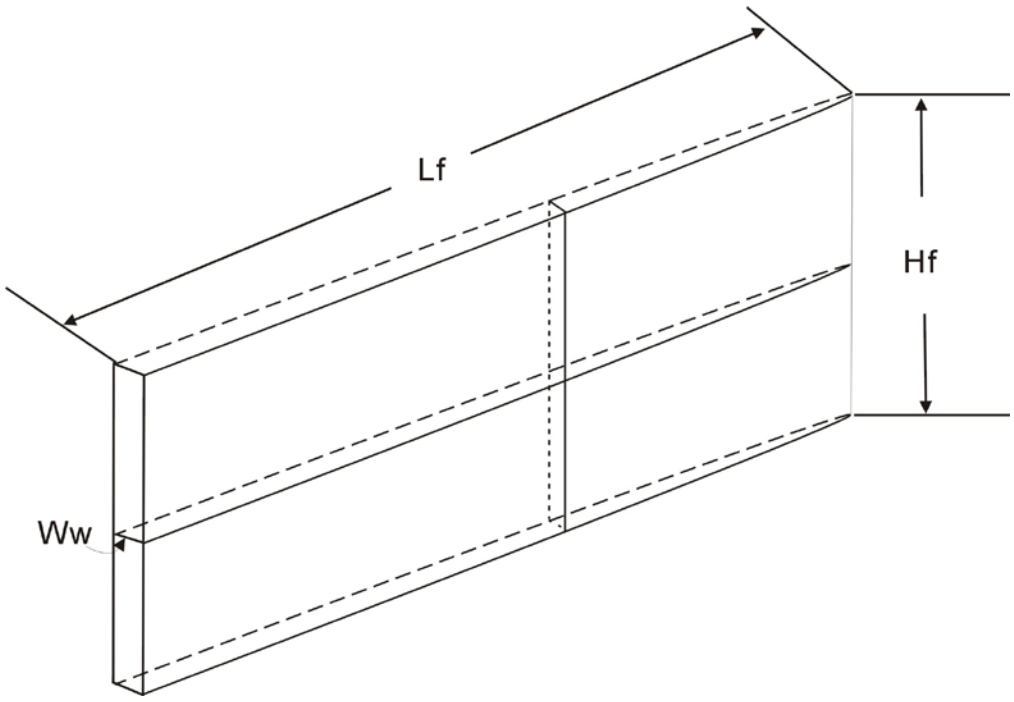

Fig.1.4 Geometry of KGD Model (Geertsma and de Klerk 1969)

The KGD model makes six assumptions: the fracture has an elliptical cross section in the horizontal plane; each horizontal plane deforms independently; the fracture height, h_f, is constant; the fluid pressure in the propagation direction is determined by the flow resistance in a narrow rectangular, vertical slit of variable width; the fluid does not act on the entire fracture length; and the cross section in the vertical plane is rectangular (fracture width is constant along its height) (Geertsma, 1969).

1.3.3 Penny-Shape or Radial Model

In the penny-shape or radial model, the fracture is assumed propagating within a given plane and the geometry of the fracture is symmetrical with respect to the point at which the fluid is injected (Fig.1.5). The study of the penny-shaped fracture in a dry rock

mass can be found in e.g., Abé *et al*. (1976). Abé *et al*. (1976) assumed a uniform distribution of fluid pressure and constant fluid injection rate.

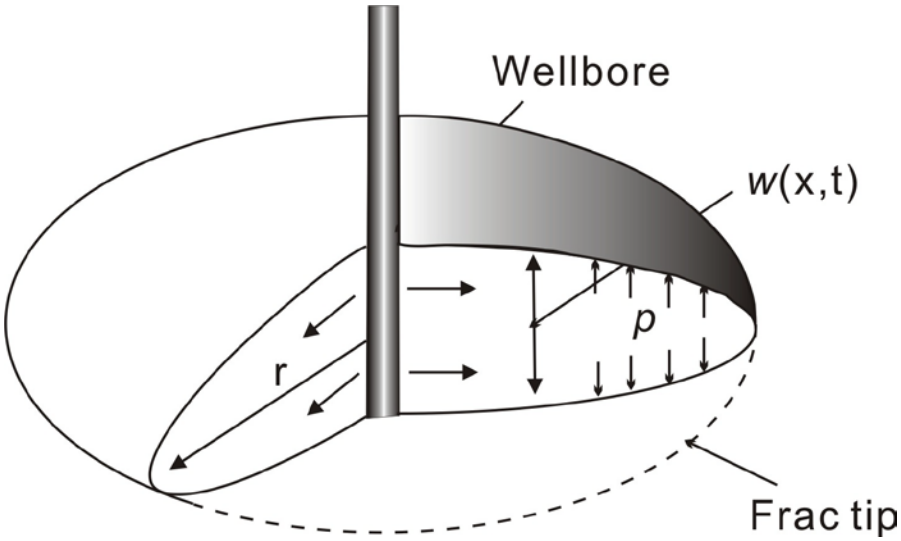

Fig.1.5 Geometry of Penny-Shape or Radial Model

1.3.4 Compare between 2D Models

Table.1.1 Comparison between Traditional 2D Hydraulic Fracture Models

Model	Assumptions	Shape	Bottom Hole Pressure	Application
PKN	Fixed Height Plain Strain	Elliptical Cross Section	Increasing with Time	More Appropriate When Length»Height
KGD	Fixed Height Plain Strain	Rectangle Cross Section	Decreasing with Time	More Appropriate When Length«Height
Radial	Uniform Distribution of Fluid Pressure, Constant Fluid Injection Rate	Circular Cross Section	Decreasing with Time	More Appropriate When It is Radial

The traditional 2D hydraulic fracturing models PKN, KGD, and Radial Model can be compared as shown in Table.1.1. The mechanics of the traditional PKN and KGD models and the analysis on sensitivity of some factors will be shown in the appendix A.

1.4 Poroelasticity

During the propagation of a hydraulic fracture, fluid loss into the permeable formation causes the pore pressure increase in the reservoir, which in turn will cause dilation of the rock around the fracture, and finally, reduce the width of the fracture. Rock deformation also causes pore pressure to increase. The mechanism of poroelasticity will be discussed in detail in Section 2.

The design of Hydraulic fracturing and the stress analysis must take into account the influence of pore pressure increase caused by leak off. In addition, pore pressure changes can cause stresses variations in the rock formation. The first detailed studies of the coupling between the fluid pressure and solid stress fields were described by Biot (1941). In poroelastic theory, the time dependent fluid flow is incorporated by combining the fluid mass conservation with Darcy's law; the basic constitutive equations relate the total stress to both the effective stress given by deformation of the rock matrix and the pore pressure arising from the fluid. Biot’s theory of poroelasticity has been reformulated by a number of investigators (e.g. Geertsma, 1957; Rice and Cleary, 1976). Fig.1.6 shows the mechanics of poroelasticity.

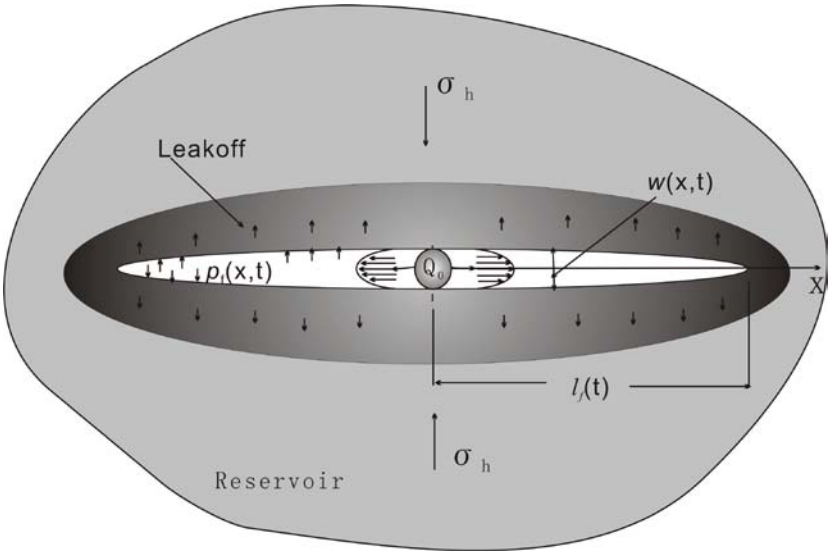

Fig.1.6 Mechanics of Poroelasticity

The coupled poroelastic effects can be summarized as follows (Vandemme et.al, 1989):

(1) A volumetric expansion of the porous rock is induced by an increase of the pore pressure;

(2) Pore pressure is increased from the application of a confining pressure if the fluid is prevented from escaping (undrained condition), an increase of the pore pressure results from the application of a confining pressure.

1.5 Problems Associated with Rock Mechanics

Fracturing by water injection is often used in both tight and permeable reservoirs. In tight reservoirs fractures are usually induced intentionally to increase the injectivity. In a permeable reservoir, fracturing may occur unintentionally if cold water is injected into a relatively hot reservoir. For example, during water-flooding or other secondary or tertiary recovery processes, fluids at temperatures typically cooler (70-80 ^{o}F) than the in-situ

reservoir temperatures (200± ºF) are injected into a well. A region of cooled rock forms around an injection well, and grows as additional fluid is injected. The rock within the cooled region contracts and this leads to a decrease in stress concentration around the injection well until the injection pressure minus the hoop stress exceeds the tensile strength of the rock at a critical point on the well boundary and a fracture begins to propagate to orient itself in the direction of maximum in-situ stress. Although the increase in injectivity is favorable, the fracture may or may not have an adverse effect on the sweep efficiency of the water drive in the case of petroleum, or inefficient heat extraction in geothermal reservoirs, depending on the length, height and orientation of the fracture. These fracture parameters can also be of critical importance for a successful application of a tertiary recovery process, and development of geothermal reservoirs.

Fractures can develop considerable shear stress mechanically and the zone of increased shear stress provides a mechanism for microseisms to accurately reflect the length (and height) of the fracture as many microseisms should be induced in the zone as the fracture propagates (Warpinski *et al.,* 2001). These microseisms could be used to estimate the stimulated reservoir volume and the enhanced permeability.

With the distributions of pore pressure and in situ stresses, and the properties of reservoir rock mass, the failed reservoir volume and the enhanced permeability by the stimulation after water injection could be estimated.

Therefore, to analyze these two estimations, two models are developed in our work—the WFPSD model and the FracJStim model. The WFPSD model, which is modeling the water-flood induced fracturing from a single well in an infinite reservoir, is petroleum applications. The FracJStim model has a more general character and can be

used in the analysis of pore pressure and stress distributions around a hydraulic fracture, and to assess the permeability enhancement around a hydraulic fracture when appropriate.

In petroleum field operations, injection is at a BHP that is high enough to initiate and extend a hydraulic fracture. The injected fluid then leaks off radically through a large fracture face area. Because of the decreasing in horizontal in-situ rock stresses that result from cold fluid injection, hydraulic fracturing pressures can be much lower than would be expected for an ordinary low leak-off hydraulic fracturing treatment. If the injection conditions are such that a hydraulic fracture is created, then the flow system will evolve from an essentially circular geometry in the plan view to one characterized more nearly as elliptical as shown in Fig.1.7.

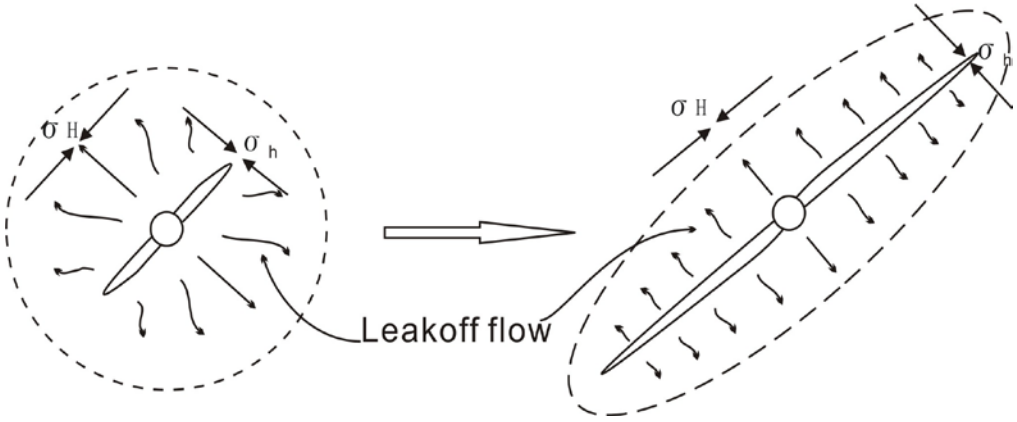

Fig.1.7 Evolution of Flow System

1.6 Literature Review

Geertsma (1966) considered the potential of poroelastic effects for influencing hydraulically-driven fracture propagation. Oil bearing rock is a two-phase system with

the potential for these effects. However, Geertsma concluded that these effects were to be insignificant in practical situations. Cleary (1980) suggested that poroelastic effects can be expressed as “back-stress”. Settari included poroelastic effects through a similar approximation (Settari, 1980).

A poroelastic PKN hydraulic fracture model based on an explicit moving mesh algorithm was set by Detournay (Detournay *et al*. 1990). The poroelastic effects, induced by leak-off of the fracturing fluid, were treated in a manner consistent with the basic assumptions of the PKN model. Their model was formulated in a moving coordinates system and solved using an explicit finite difference technique.

Perkins and Gonzalez (1985) presented a semi-analytical model of a water-flood-induced fracture emanating from a single well in an infinite reservoir. Their model has two important features. First, the leak-off distribution is two-dimensional with the pressure transient moving elliptically outward into the reservoir with respect to the growing fracture. Second, the effect of thermo-elastic changes on reservoir rock stress and therefore on fracture propagation pressure was incorporated. It was shown that cooling of the reservoir rock following injection of cold water may cause fractures to become very long. Koning (1985) presented an analytical model for waterflood-induced fracture growth under the influence of poro- and thermoelastic changes in reservoir stress. In his work, a model is presented in which the leak-off distribution in the reservoir is allowed to range from 1-D perpendicular to 2-D radial with respect to the fracture. A three dimensional calculation of poro-elastic changes in reservoir stress at the fracture face is performed analytically for a quasi steady state pressure profile including elliptical discontinuities in fluid mobility.

In our work, we use the formulation of Koning in the framework of Perking and Gonzales approach to water-flood fracture propagation. The leak-off distribution in the reservoir is allowed to range from 1-D perpendicular to 2D radial with respect to the fracture. Also, an analytical calculation of the poroelastic stress changes at the fracture face is presented. The stress change is induced by a quasi steady-state pressure profile including elliptical discontinuities in fluid mobility. The calculations are performed in two dimensions (plane strain) in elliptical coordinates.

We also include the effect of fracture pressurization in the model using the solution for calculating the stresses distribution around a flat elliptic crack (Jaeger and Cook, 1979). Also, the solution provided by Pollard and Segall (1987) is utilized to improve the expressions for the calculation of the stress changes around an elliptic fracture by including the effect of fracture pressurization.

A lot of work has been done on the joints slip in rock formations.

Jaeger and Cook (1979) gave the Mohr-Coulomb failure criterion for rock joints, and calculated the shear stress and the normal stress on a joint surface using the principal stresses.

Mildren *et al*. (2002) and Nelson *et al*. (2007) introduced the structural permeability diagram technique to estimate the additional treating effective pressure required to reactivate the existing joints in rock formations.

Palmer *et al.* (2007) used a method to estimate the enhanced permeability after stimulation by hydraulic fracture in Barnett Shale. They pointed out that some data show greater gas flow rate is correlated with a larger “failed reservoir volume”, and a higher net fracturing pressure. They instigated the shear slip or failure along planes of weakness

by pore pressure increases during injection of fracturing fluid. By combing the knowledge of in situ stress, and the strength for the planes of weakness, they predicted failed distance from the central fracture plane. By matching the failed reservoir volume with the volume of the microseismic cloud, they estimated the enhanced permeability by stimulation after injection.

1.7 Research Objectives

The objectives of this study are:

1) To study the poroelasic effects on fracture propagation, as well as on the pore pressure and stress distributions around a fracture. To investigate the pore pressure and stresses distributions around a hydraulically induced fracture based on previous works.
2) To study the shear slip or failure along planes of weakness by pore pressure increases during injection of fracturing fluid.
3) To research the stimulated volume (rock failure) and the enhanced permeability by hydraulic fracturing operations.

1.8 Sign Convention

Most published papers concerning poroelasticity consider tensile stress as positive. However, in rock mechanics, compressive stresses are generally considered as positive for the convenience of engineering use. In this thesis, in order to be consistent with the rock mechanics literature, all equations are presented using the compression positive convention. This sign convention is adopted for the remainder of this thesis unless otherwise specified.

2 POROELASTICITY AND THERMOELASTICITY

2.1 Introduction

The effects of poroelasticity and thermoelasticity on fracture propagation, as well as the pore pressure and stress distributions are considered in this study. For geothermal reservoirs, these two factors are both significant, while for gas shale reservoirs, the temperature of formation is not high and the effects of thermoelasticity are insignificant. In this section, the effects of poroelasticity on fracture propagation are studied, and the theory of thermoelasticity is introduced.

The theory of poroelasticity was introduced by Biot in 1941. The theory was subsequently extended by Biot to include dynamics, anisotropy and nonlinear materials. Rice and Cleary (1976) published a much more attractive presentation of theory through the use of material parameters that are readily given a physical interpretation.

The theory of poroelasticity is an extension of the theory of elasticity and as such inherits the same fundamental assumptions. It is assumed in the theory of elasticity that a body is perfectly elastic and its material is homogeneous and continuously distributed over its volume. Timoshenko and Goodier (1951) noted that very few bodies are homogeneous at all scales. However, if the geometry of the structure is large compared to the scale at which inhomogeneities are apparent then the theory can be a reasonable approximation.

For the theory of poroelasticity to be a reasonable approximation, it is necessary for the body to be large relative to a representative element of volume. In addition, it is assumed that the body is composed of a porous, elastic, solid skeleton that is saturated with a fluid. Both the pore fluid and the solid grains that compose the skeleton can be

assumed to have a linear compressibility, or can be assumed to be incompressible. Finally, it is assumed that the fluid flow through the skeleton is governed by Darcy's law, so that the flow rate is directly proportional to the gradient of the pore pressure.

Rice and Cleary (1976) stated that the pore pressure, *p*, can be defined as "the equilibrium pressure that must be exerted on a homogeneous reservoir of pore fluid brought into contact with a material element so as to prevent any exchange of fluid between it and the element". They also propose that the term undrained deformation applies to "stress alterations, $\Delta\sigma_{ij}$, over a time scale that is too short to allow loss or gain of pore fluid in an element by diffusive transport to or from neighboring elements". Conversely, the term drained deformation applies to stress alterations, $\Delta\sigma_{ij}$, over a time scale that is allow diffusive transport of pore fluid between elements to reach a steady state condition.

There are some parameters that arise commonly when dealing with poroelastic materials. In this section they will be defined.

First, the poroelastic constant, α, is independent of the fluid properties and is defined as (Rice and Cleary, 1976):

$$\alpha = \frac{3(\nu_u - \nu)}{B(1-2\nu)(1+\nu_u)} = 1 - \frac{K}{K_s} \quad \text{..... (2.1)}$$

In which B is Skempton pore pressure coefficient, ν_u is undrained Poisson ratio, ν is drained Poisson ratio, K is drained bulk modulus of elasticity, and Ks bulk modulus of solid phase. The range of poroelastic constant is 0 to 1, but most rocks fall in the range of 0.5 to 1 (Rice and Cleary, 1976).

The second parameter is poroelastic stress coefficient, usually expressed with symbol η, and defined as (Detournay and Cheng, 1993):

$$\eta = \alpha \frac{(1-2\nu)}{2(1-\nu)} \quad \text{..... (2.2)}$$

The range of η is 0 to 0.5, and it is independent of the fluid properties.

The theory of thermoelasticity accounts for the effect of changes in temperature on the stresses and displacements in a body (Jaeger, Cook and Zimmerman, 2007). The thermoelasticity theory can be analogous to the theory of poroelasticity, with the temperature playing a role similar to that of the pore pressure.

The coupled theory of thermo-poroelasticity was first developed by Palciauskas and Domenico (1982), and later studied by other researchers (Zhang, 2004). In a fluid-saturated porous rock, thermal loading can significantly alter the surrounding stress field and the pore pressure field. Thermal loading induces volumetric deformation because of thermal expansion/contraction of both the pore fluid and the rock solid. If the rock is heated, expansion of the fluid can lead to a significant increase in pore pressure when the pore space is confined. The tendency is reversed in the case of cooling. Therefore, the time dependent poromechanical processes should be fully coupled to the transient temperature field.

2.2 Poroelastic Effects on Hydraulic Fracture

Geertsma (1966) considered the potential of poroelastic effects for influencing hydraulically-driven fracture propagation. Oil bearing rock is a two-phase system with the potential for these effects. However, Geertsma concluded that these effects were to be insignificant in practical situations. Cleary (1980) suggested that poroelastic effects can be expressed as “back-stress”. Settari (1980) included poroelastic effects through a similar approximation.

A poroelastic PKN hydraulic fracture model based on an explicit moving mesh algorithm was described by Detournay (Detournay *et al*., 1990). The poroelastic effects, induced by leak-off of the fracturing fluid, were treated in a manner consistent with the basic assumptions of the PKN model. Their model was formulated in a moving coordinates system and solved using an explicit finite difference technique.

In our work, we consider the frame work of Detournay (Detournay *et al*., 1990), and a FORTRAN program is set to get the results for the effects from poroelasticity on the fracture propagation. In our program, the input data are listed in Table.2.1.

Table 2.1 Input Parameters for Poroleastic PKN Model (Detournay *et al*., 1990)	
Power law constitutive constant (K):	$5.6*10^{-7}$ MPa•$s^{0.8}$
Power law fluid index (n):	0.8
Injection rate (Q_o):	$4*10^{-3}$ m^3/s
Poisson's ratio (v):	0.2
Shear Modulus (G):	$1*10^4$MPa
Fracture Height (H):	10 m
Leak-off coefficient (C_l):	$6.3*10^{-5}$ $m/s^{1/2}$
Interface pressure (λ_p):	1.7 MPa
Poroelastic coefficient (η):	0.25
Diffusivity coefficient (c):	0.4 m^2/s

2.3 Results of Poroelastic PKN Model

In our work, the numerical method is used to simulate a hydraulic fracturing treatment in a permeable formation using a non-Newtonian fluid. The analysis is carried out by first taking into consideration and then neglecting poroelastic effects. The basic data used are shown in Table 2.1.

To compare with the results of previous work by Detournay *et al*., (1990), the fracture is injected at the constant flow rate Q_0 for 1000s, and then the well is shut in. After the shut in of the well, the fracture pinching is analyzed without fluid flow back. The poroleastic evolution function from our program is shown in Fig.2.1, which has great agreement with the result given by Detournay *et al*., (1990). The fracture length, width and the net fracturing pressure of the fracture are shown in Figs.2.2-2.4.

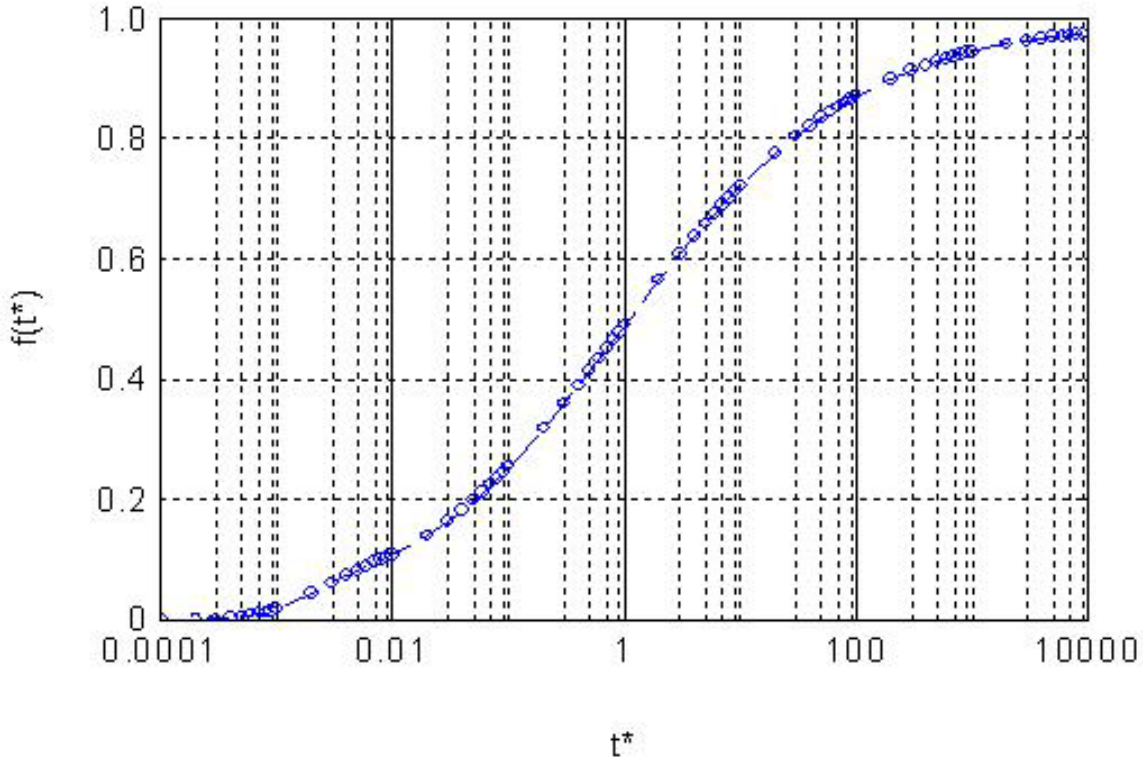

Fig.2.1 Poroelastic Evolution Function

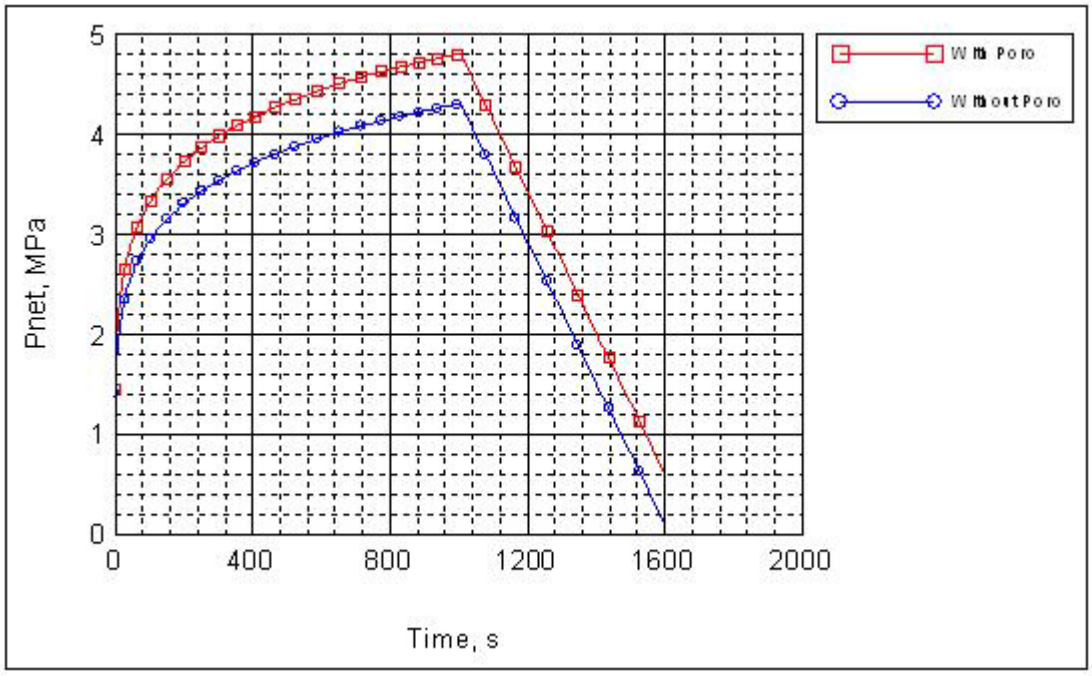

Fig.2.2 Variation of Fracture Pressure with Time

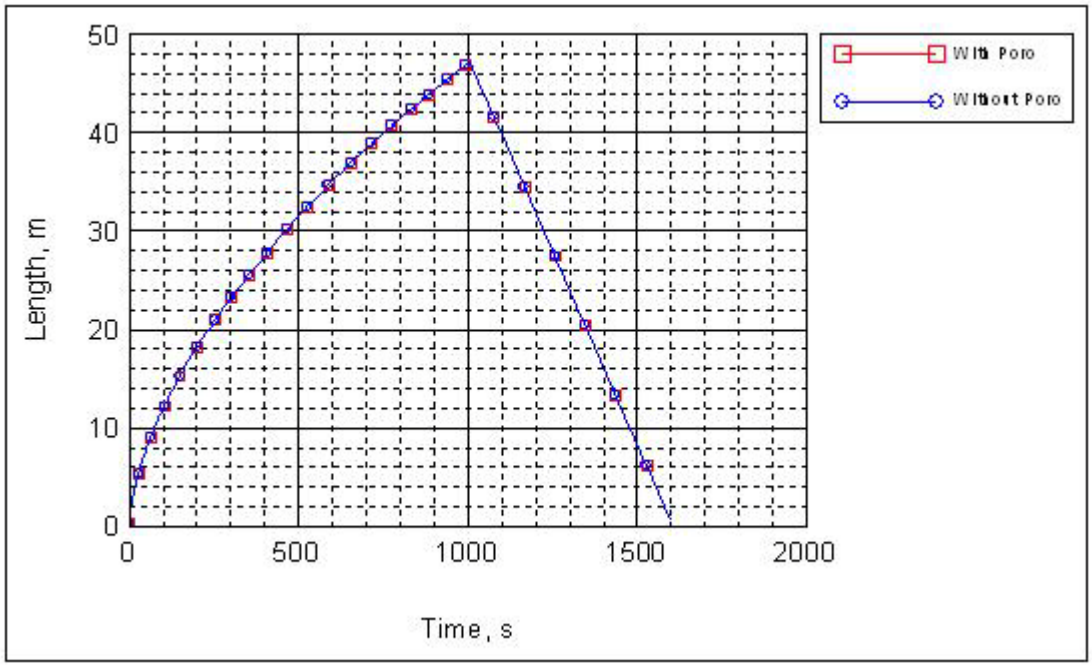

Fig.2.3 Variation of Fracture Length with Time

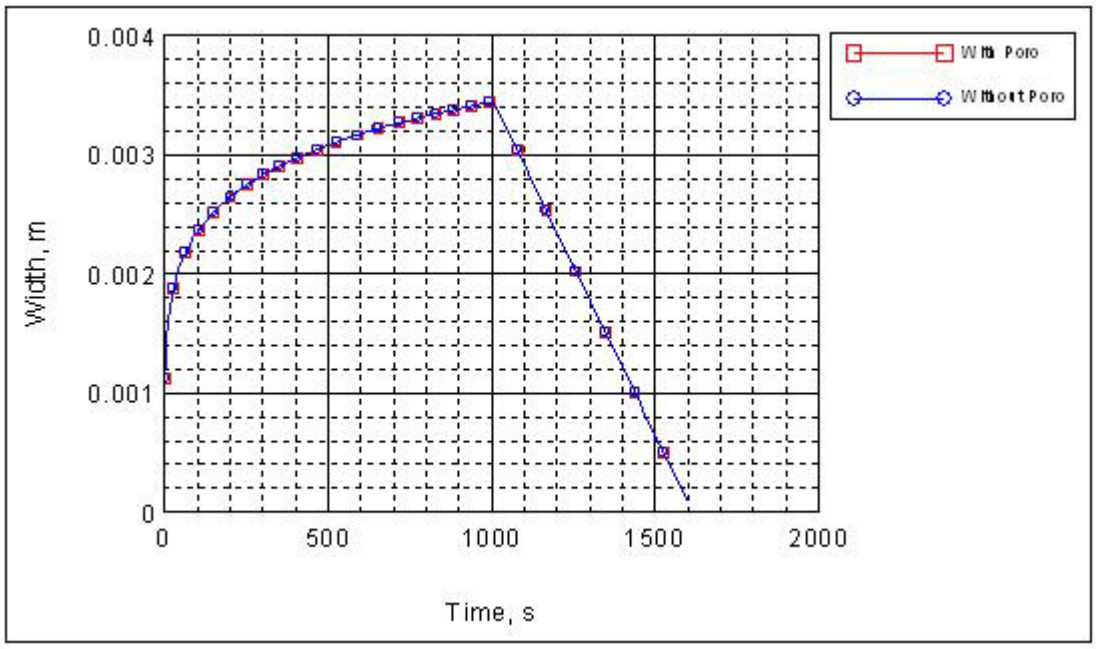

Fig.2.4 Variation of Fracture Maximum Width with Time

From Fig.2.2 to Fig.2.4, the fracture pressure, length, and width are increasing with time until the shut-in time, and then are decreasing. By comparing the variations of fracture length, width, and pressure under the condition of poroelasticity and without poroelasticity, it is easy to get conclusion that the fracture length and width are almost not affected by poroelasticity, and fracture pressure is affected significantly.

To verify the results of this study, the plots are compared with the results from Detournay *et al.* (1990), and the simulation of the net fracturing pressure, the fracture length, and the fracture maximum width are close. The agreements between our work and the results given by Detournay *et al.* (1990) give the validation of our work.

In our study, the sensitivity analyses of parameters are examined. The variations of fracture length, width, and pressure with time under different shear Modulus, power

law constant, diffusivity coefficient are investigated. The detailed analysis can be found in Appendix B.

2.4 Conclusions and Discussions

In this section, the impact of poroelastic effects on hydraulic fractures is reviewed, and a poroelastic PKN model is examined. From the study, the effects of poroelasticity on fracture propagation can be concluded as the following:

- Poroelasticity causes a significant increase in fracturing pressure
- The fracture length and width are unaffected;

From this study, it suggests that poroelastic effects can cause a significant increase of the fracturing pressure, but have little influence on the geometry of the fracture. This is direct consequence of assuming a constant leak-off coefficient. As suggested by Detournay et.al (1990), for pressure dependent leak-off, the prediction of both the geometry and the pressure will be different. Since the pressure response is under strong influence of poroelasticity, ignoring poroelastic effects can lead to an erroneous interpretation of the parameters such as minimum in situ stress, leak-off coefficient, when determining of the state of the formation during an actual treatment.

3 PORE PRESSURE DISTRIBUTION AROUND HYDRAULIC FRACTURE

Pore pressure refers to the pressure in pores of a reservoir, usually the hydrostatic pressure. During the water injection and hydraulic fracturing operations, the water leaking off to the formation around fracture may increase the pore pressure in the reservoir near fracture surface. The pore pressure variations will affect the stresses distributions around the fracture and the affect the failure of rock mass in the reservoir. Therefore, researches on the pore pressure distributions around a hydraulic fracture are of interest.

If fluids at temperatures typically cooler than the in-situ reservoir temperatures are injected into a well, a region of cooled rock forms around an injection well, and grows as additional fluid is injected. The rock within the cooled region contracts and this leads to a decrease in stress concentration around the injection well until the injection pressure minus the hoop stress exceeds the tensile strength of the rock at a critical point on the well boundary and a fracture begins to propagate and will orient itself in the direction of maximum in-situ stress. As discussed in previous sections and shown in Fig.1.6, the flow evolves into elliptical shape during the fracture propagates.

In our study, two models were developed. As introduced in previous sections, the model WFPSD is a model of a water-flood induced fracture from a single well in an infinite reservoir (Perkins and Gonzalez, 1985; Koning, 1985). The model is used to calculate the length of a water flood fracture and the extent of the cooled and flooded zones. The model allows the leak-off distribution in the formation to be two-dimensional with the pressure transient moving elliptically outward into the reservoir with respect to the growing fracture. The thermoelastic stresses are calculated by considering a cooled

region of fixed thickness and of elliptical cross section (details in next section). The methodology of Perkins and Gonzalez (1985) is used for calculating the fracture lengths, bottomhole pressures (BHP's), and elliptical shapes of the flood front as the injection process proceeds. However, in contrast to Perkins and Gonzalez (1985) and Koning (1985) who gave only the calculation of poroelastic changes in reservoir stress at the fracture face for a quasi steady-state pressure profile, our model allows the calculation of the pore pressure and in situ stress changes at any point around the fracture caused by thermoelasticity, poroelasticity, and fracture compression. The FracJStim model calculates the stress and pore pressure distribution around a fracture of a given length under the action of applied internal pressure and in situ stresses as well as their variation due to cooling and pore pressure changes. It also calculates the failure potential around the fracture to determine the zone of tensile and shear failure.

In petroleum field operations, injection often continues at a BHP that is high enough to initiate and extend hydraulic fractures. The injected fluid leaks off radically through the large fracture face area. Because of the decreasing in horizontal in-situ rock stresses that result from cold fluid injection, hydraulic fracturing pressures can be lower than would be expected for an ordinary low leak-off hydraulic fracturing treatment.

Perkins and Gonzalez (1985) presented a semi-analytical model of a water-flood-induced fracture emanating from a single well in an infinite reservoir. Their model has two important features. First, the leak-off distribution is two-dimensional with the pressure transient moving elliptically outward into the reservoir with respect to the growing fracture. Second, the effect of thermo-elastic changes on reservoir rock stress and therefore on fracture propagation pressure was incorporated. It was shown that

cooling of the reservoir rock following injection of cold water may cause fractures to become very long compared to the fractures without cooling.

Koning (1985) presented an analytical model for waterflood-induced fracture growth under the influence of poro- and thermoelastic changes in reservoir stress. He assumed the fracture geometry from the traditional PKN fracture propagation model. By considering the pore pressure and temperature effects on the stresses changes around a hydraulic fracturing and on fracture propagation, an analytical model was also given for the 3-D poroelastic and thermoelastic stress change at the fracture surface.

In our work, we use the formulation of Koning in the framework of Perking and Gonzales approach to water-flood fracture propagation. The leak-off distribution in the reservoir is allowed to range from 1-D perpendicular to 2D radial with respect to the fracture. The pore pressure distributions during fracturing are calculated by using their framework.

For the pore pressure distributions after hydraulic fracturing, the simplified calculation is used from the Koning's work.

3.1 Pore Pressure Geometry around a Fracture

From Muskat (1937), if water is injected into a line crack (representing a two-wing, vertical hydraulic fracture), the flood front will progress outward, and its outer boundary at any time can be described approximately as an ellipse that is confocal with the line crack. Muskat (1937) deduced this by considering the flow from a finite line source into an infinite reservoir, and using the theory of conjugate functions.

As Muskat (1937) studied in his work, the physical significance of the theory of conjugate functions consists essentially in the observation that both the real and

imaginary parts of any analytic function of the complex variable $z=x+iy$, with the physical application considering the flow from a finite line source into an infinite reservoir, defined as:

$$f(z) = p + i\psi = \cosh^{-1}\frac{(x+iy)}{c} \quad \text{..... (3.1)}$$

where c is a constant and p is the fluid pressure. Separating real and imaginary parts, it is readily seen that:

$$\begin{aligned} x &= c\cosh(p)\cos(\psi) \\ y &= c\sinh(p)\sin(\psi) \end{aligned} \quad \text{..... (3.2)}$$

So that:

$$\begin{aligned} &\frac{x^2}{c^2\cosh^2(p)} + \frac{y^2}{c^2\sinh^2(p)} = 1 \\ &\frac{x^2}{c^2\cos^2(\psi)} - \frac{y^2}{c^2\sin^2(\psi)} = 1 \end{aligned} \quad \text{..... (3.3)}$$

The above equation (3.3) shows that the equipressure curves p=constant are the confocal ellipses with foci at $x = \pm c$.

3.2 Pore Pressure Distributions

From section 3.1, the pore pressure distribution geometry around a fracture could be described approximately as an ellipse. As suggested by Perkins and Gonzalez (1985), if the injected fluid is at a temperature different from the formation temperature, a region of changed rock temperature with fairly sharply defined boundaries will progress outward from the injection well but lag behind the flood front. The outer boundary of the region of changed temperature also will be elliptical in its plan view and confocal with the line crack (see Fig. 3.1).

With continued injection and fracture propagation, the pore pressure around the fracture will change due to the effect of thermo-poroelasticity. Pore pressure within the region of altered temperature (Cooled zone in Fig.3.1) will be changed by the contraction of the formation rock and the expansion of surrounding rock. Pore pressure within the waterflood region (Flooded zone in Fig.3.1) will be changed by the expansion or the formation rock. In the three different regions, the pore pressure changes are calculated separately. And the total pore pressure at any point around the fracture should be the reservoir pressure plus the sum of all pore pressures induced.

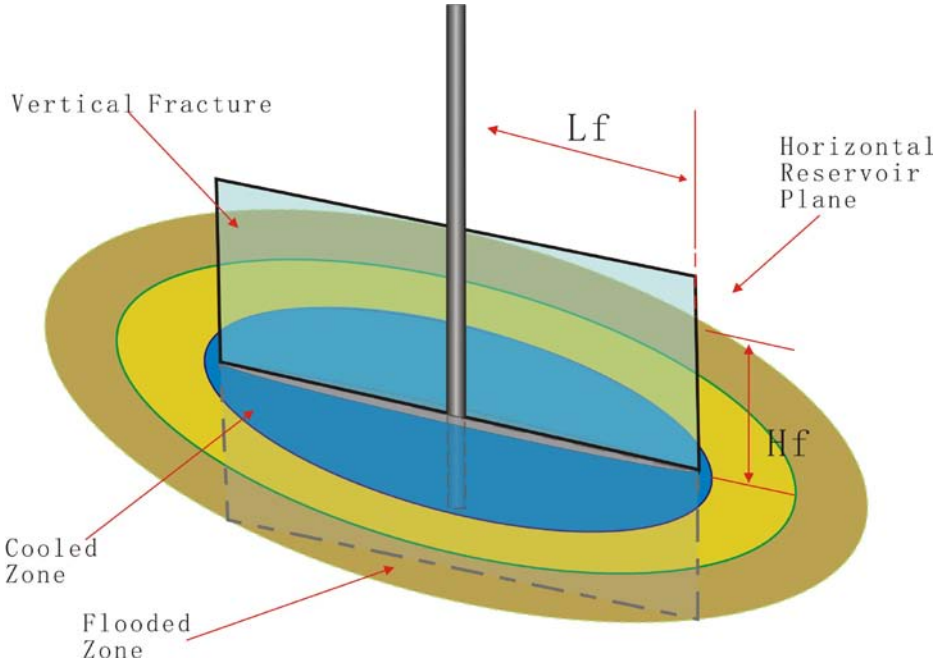

Fig.3.1 Plan View of Two-winged Hydraulic Fracture.

Therefore, let's consider any a point (x, y) around the fracture, we set in elliptical coordinates:

$$x=L_f \cosh\xi \cos\eta \quad \text{..... (3.4)}$$

$$y=L_f \sinh\xi \sin\eta \quad \text{..... (3.5)}$$

The pore pressure at any point around the fracture is changing with time and can be given by (Koning, 1985):

$$P(\xi,\eta,t)=P_i+\Delta p(\xi) \quad \text{..... (3.6)}$$

In which:

$$\Delta p_1(\xi)=\frac{q}{2\pi kh\lambda_1}\ln\left(\frac{3.0\sqrt{\kappa t}}{L\cosh\xi+L\sinh\xi}\right);\ \xi_1\le\xi<\xi_2 \quad \text{..... (3.7)}$$

$$\Delta p_2(\xi)=\frac{q}{2\pi kh\lambda_2}\ln\left(\frac{a_1+b_1}{L\cosh\xi+L\sinh\xi}\right)+\Delta P_1;\ \xi_0\le\xi<\xi_1 \quad \text{..... (3.8)}$$

$$\Delta p_3(\xi)=\frac{q}{2\pi kh\lambda_3}\ln\left(\frac{a_0+b_0}{L\cosh\xi+L\sinh\xi}\right)+\Delta P_1+\Delta P_2;\ 0\le\xi<\xi_0 \quad \text{..... (3.9)}$$

In which,

$$\begin{aligned}\lambda_1 &= kk_{rw}/\mu_o\\ \lambda_2 &= kk_{rw}/\mu_{hot}\\ \lambda_3 &= kk_{rw}/\mu_{cold}\end{aligned} \quad \text{..... (3.10)}$$

$$\kappa=\frac{k}{\phi\mu_o c_f} \quad \text{..... (3.11)}$$

where c_f is the formation compressibility.

And

$$\Delta P_1=i_w\mu_o\ln\left(\frac{3\sqrt{\kappa t}}{a_1+b_1}\right)/(2\pi kk_{rw}h) \quad \text{..... (3.12)}$$

$$\Delta P_2=i_w\mu_w^{\ hot}\ln\left(\frac{a_1+b_1}{a_0+b_0}\right)/(2\pi kk_{rw}h) \quad \text{..... (3.13)}$$

These equations are the elliptical pressure distributions in different zones surrounding the fracture. In fact, it is better to calculate the pore pressure distribution at a

certain time *t*, so that we can see the difference of pore pressure in position. Therefore, at every certain time t, we can get the distribution for the pore pressure around the fracture. This will be shown in a case study (Fig. 3.2).

Considering the condition of pore pressure distribution after hydraulic fracturing, Warpinski and Teufel (1987) gave the pressure transient profile. The pressure in an infinite joint is approximately given by:

$$p(y,t) = p_f - (p_f - p_r)(y / y_f) \quad \text{..... (3.14)}$$

where p_f is the average pressure in hydraulic fracture over the entire treatment time and p_r is the original reservoir pore pressure.

And y_f is the location of the fluid front which could be approximated given as (Modified from Koning, 1985):

$$y_f = 1.5\sqrt{\frac{kt}{\phi\mu c_t}} \quad \text{..... (3.15)}$$

3.3 Case Study

We used the parameters from Perkins and Gonzales (see Table3.1) to calculate the pore pressure distributions around a hydraulic fracture.

Fig.3.2 shows the pore pressure distributions around a fracture during the fracture propagation. And from the Fig. 3.2 (scale exaggerated in radial direction), it is easy to see that the pore pressure distribution was about to be co-focal ellipses around the fracture, and the pore pressure reaches its highest value at the fracture surface and decays to the reservoir pore pressure in the far field (Fig. 3.2).

Table 3.1 Input Parameters for Simulations (Perkin and Gonzalez, 1985)	
Injection condition	
Depth to the center of the formation (D):	1524m
Reservoir Thickness (h):	30.5m
Water injection rate (I_w):	477m^3/d
Time (t):	5year
Initial Reservoir temperature (T_R):	65.6°C
Bottomhole temp. of the injection water (T_w):	21.1°C
Undisturbed reservoir fluid pressure (P_R):	13.78MPa
Reservoir Rock Properties	
Compressibility of mineral grains (c_{qr}):	2.20E-05 $(MPa)^{-1}$
Compressibility of fracture (c_f):	4.080E-04$(MPa)^{-1}$
Young's modulus (E):	13.8E+03MPa
Relative perm. to water at residual oil saturation (k_{rw}) :	0.29
Residual oil saturation (S_{or}):	0.25
Initial water saturation (S_{wi}):	0.20
Rock surface energy (U):	5.0E-02 kJ/m^2
Linear coefficient of thermal expansion (β):	5.60E-06mm/ (mm*K)
Poisson's ratio (v):	0.15
Density * Specific heat of mineral grains (ρ_{qr}*C_{qr}):	2347kJ/ (m^3*K)
Minimum in-situ, total horizontal earth stress ($(\sigma_h)_{min}$):	24.1MPa
Porosity (Φ):	0.25
$(\sigma_H)_{max}$ /$(\sigma_h)_{min}$:	1.35
Reservoir permeability (k):	4.935E-14m^2
Reservoir Fluid Properties	
Compressibility of oil (c_o):	1.5E-03 $(MPa)^{-1}$
Compressibility of water (c_w):	5.20E-04 $(MPa)^{-1}$
Specific heat of oil (C_o):	2.1kJ/(kg*K)
Specific heat of water (C_w):	4.2kJ/(kg*K)
Viscosity of oil at 65.6 °C (μ_o):	1.47E-09 MPa*s
Viscos ity of water at 65.6 °C (μ_w):	4.30E-10 MPa*s
Viscosity of water at 21.1°C (μ_w):	9.95E-10 MPa*s
Density of oil (ρ_o):	881kg/m^3
Density of water (ρ_w):	1000kg/m^3

Fig.3.2 shows the contours of pore pressure around the fracture at injection time t=100 days. At this time, the program based on Perkins and Gonzales shows the half-fracture length, and by the method in this program, a contour plot of pore pressure is shown in Fig.3.2 for t=100 days. The pattern of pore pressure distribution is elliptical as one would expect. Note that half-fracture length is about 137 feet (41 m) at t=100 days.

The extent of the various invaded zones are also calculated, and the results show the a_0=148 ft; b_0=57 ft for the cool region, a_1=222 ft and b_1=175 ft and for the water flooded region (Fig.3.3).

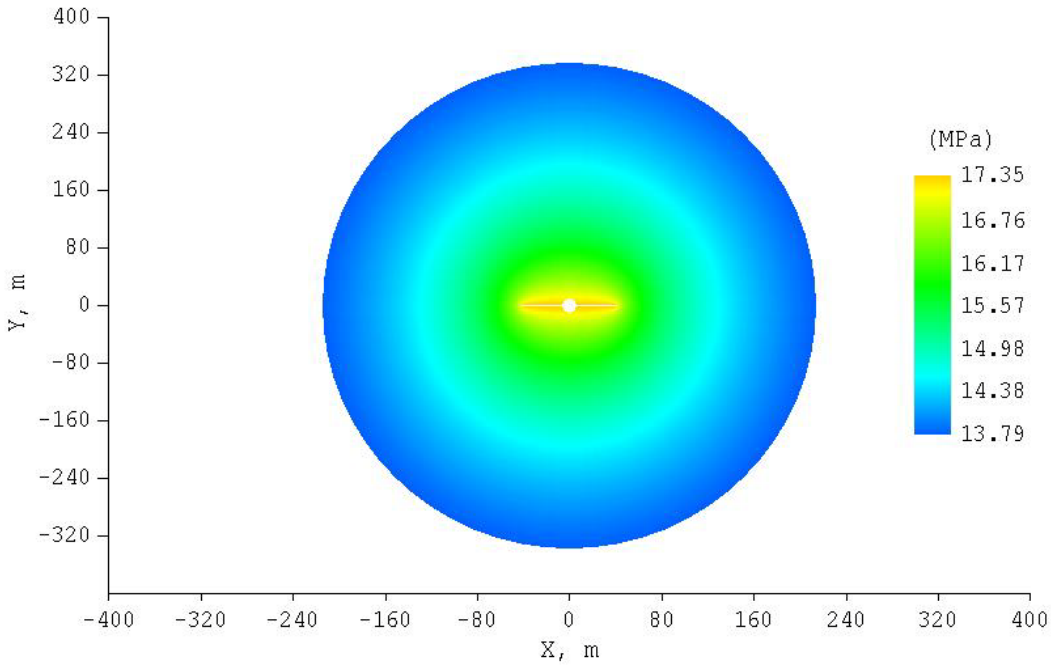

Fig.3.2 Pore Pressure Distribution around the Fracture (t=100 days)

Fig.3.3 shows the fracture length and the major and minor axis of cooled and flooded zone as a function of time. The major axis of cooled region is almost the same as fracture length with time.

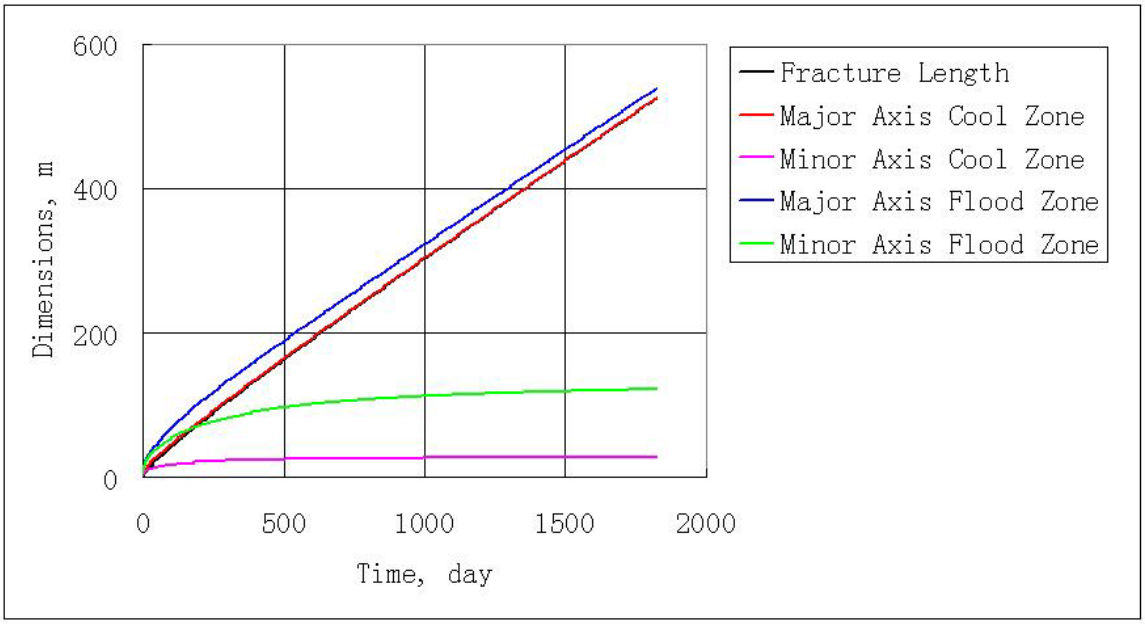

Fig. 3.3 Fracture Length and Major and Minor Axis of Cooled and Flooded Zones as a Function of Time

Another case is given in this study for the pore pressure distributions after hydraulic fracturing. Table 3.2 is for the Barnett Shale, assuming the fracturing net pressure in is 900 psi; the distribution of pore pressure around the hydraulic fracture is plotted in Fig.3.4.

From the Fig.3.4, we can see that the pore pressure distribution is elliptically decreasing from bottom-hole pressure at the fracture surface to the original reservoir pore pressure at far field.

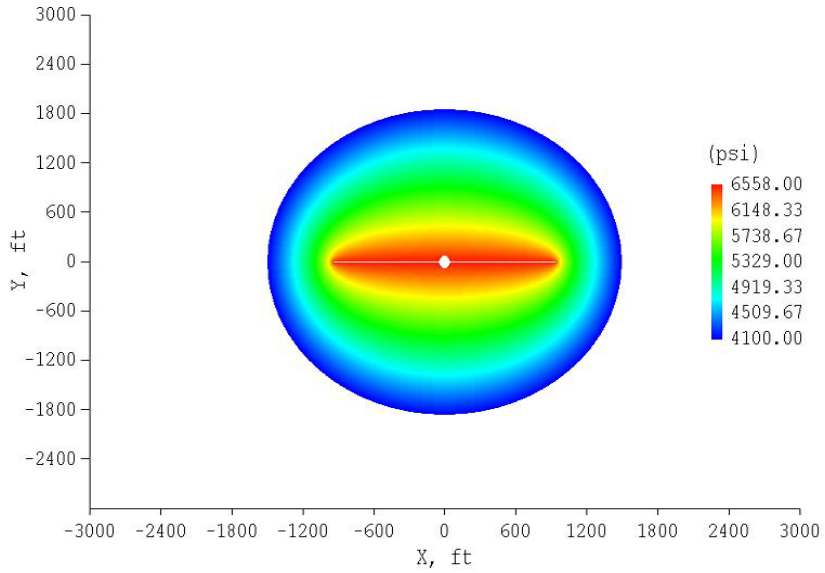

Fig.3.4 Pore Pressure Distribution around Fracture in Barnett Shale (t= 9 hours)

Table 3.2 Input Parameters for Barnett Shale (Palmer *et al.*, 2007)	
In situ Stresses	
Depth (D):	8200 ft
Min in situ stress (S_h):	5658 psi (= 0.69 psi/ft)
Max in situ stress (S_H):	6286 psi (Sh/SH = 0.9)
Overburden (S_v):	8200 psi (= 1 psi/ft)
Reservoir pressure (P_o):	4100 psi (= 0.50 psi/ft)
Barnett Shale properties	
Friction angle (Φ):	31 deg
Cohesion (c):	100 psi
Modulus (E):	3.00E6 psi
Poisson's ratio	0.25
Fracture Porosity (φ =	Ko = 0.03 mD; φo = 0.1%
Bulk compressibility (c_t):	3.69E-06 (1/psi)
Water viscosity at res. temp.	0.3 cp
Injection permeability (K):	Determined by matching the FRV trendlines
Fracture Treatment Parameters	
Frac half height (H_f):	200 ft
Frac half length (X_f):	1000 ft
Pumping time (T):	9 hours
Fracturing pressure (P_f):	100-900 Psi
Fracturing rate (Q_0):	70 bpm
Fracture fluid volume (V):	800,000-1,000,000 gal

3.4 Conclusions

In this section, we have discussed the pore pressure distributions around a fracture during the fracture propagation (fracture keeps growing). We also discussed the pore pressure distributions around a hydraulic fracture after stimulation of water injection (fracture stabilizes).

The WFPSD model for calculating the length of a water-flood induced fracture from a single well in an infinite reservoir is developed. Similarly to Perkins and Gonzalez (1985) and Koning (1985) the model allows the leak-off distribution in the formation to be two-dimensional with the pressure transient moving elliptically outward into the reservoir with respect to the growing fracture. The model calculates the length of a water flood fracture and the extent of the cooled and flooded zones. The methodology of Perkins and Gonzalez (1985) and Koning (1985) is used to calculate the fracture length, bottom-hole pressures (BHP's), and extent of the flood front as the injection process proceeds. The pore pressure at any point around the fracture is calculated in this model.

The pore pressure distributions around a hydraulic fracture after stimulation by water injection are also estimated and we will use this pore pressure distribution in the later sections to determine the sliding of joints in the reservoir.

Furthermore, the pore pressure variations due to the existence of hydraulic fracture will affect the in situ stresses around the fracture. This will be discussed in detail in next section.

4 STRESSES DISTRIBUTIONS AROUND HYDRAULIC FRACTURE

In previous section, the pore pressure distributions around a hydraulic fracture are discussed. In this section, the stresses distributions around a hydraulic fracture will be examined at any point near the fracture surface.

Fracturing of water injection wells can occur either in tight or in permeable reservoirs. In tight reservoirs fractures are usually induced intentionally to increase the injectivity. In permeable reservoirs, fracturing may occur unintentionally if cold water is injected into a relatively hot reservoir. During water-flooding or other secondary or tertiary recovery processes, fluids at temperatures cooler than the in-situ reservoir temperatures are injected into a well. A region of cooled rock forms around an injection well, and grows as additional fluid is injected. The rock within the cooled region contracts and this leads to a decrease in stress concentration around the injection well until the injection pressure minus the hoop stress exceeds the tensile strength of the rock at a critical point on the well boundary and a fracture begins to propagate to orient itself in the direction of maximum in-situ stress. Although the increase in injectivity is favorable, the fracture may have an adverse effect on the sweep efficiency of the water drive in the case of waterflooding.

In our study, we developed WFPSD model and FracJStim model separately to calculate the distributions of stresses around a propagation hydraulic fracture and a stabilized fracture.

Perkins and Gonzalez (1985) presented a semi-analytical model of a water-flood-induced fracture emanating from a single well in an infinite reservoir. Their model has two important features. First, the leak-off distribution is two-dimensional with the

pressure transient moving elliptically outward into the reservoir with respect to the growing fracture. Second, the effect of thermo-elastic changes on reservoir rock stress and therefore on fracture propagation pressure was incorporated. It was shown that cooling of the reservoir rock following injection of cold water may cause fractures to become very long.

Koning (1985) presented an analytical model for waterflood-induced fracture growth under the influence of poro- and thermoelastic changes in reservoir stress. He assumed the fracture geometry from the traditional PKN fracture propagation model. By considering the pore pressure and temperature effects on the stresses changes around a hydraulic fracturing and on fracture propagation, an analytical model was also given for the 3-D poroelastic and thermoelastic stress change at the fracture surface.

In our model, we use the formulation of Koning in the framework of Perking and Gonzales approach to water-flood fracture propagation. The leak-off distribution in the reservoir is allowed to range from 1-D perpendicular to 2D radial with respect to the fracture. Also, an analytical calculation of the poroelastic stress changes at the fracture face is presented. The stress change is induced by a quasi steady-state pressure profile including elliptical discontinuities in fluid mobility. The calculations are performed in two dimensions (plane strain) in elliptical coordinates.

4.1 Expressions for Stresses

The stresses at any point around the fracture are mainly affected by the following factors: pore pressure change, temperature change, and the presence of the fracture. The latter was considered neither by Perkins and Gonzales nor by Koning. The stresses at any point (x, y) surrounding the fracture are given by:

$$\sigma_x = \sigma_H + \Delta\sigma_{Px} + \Delta\sigma_{Tx} + \Delta\sigma_{Fx} \quad \text{..... (4.1)}$$

$$\sigma_y = \sigma_h + \Delta\sigma_{Py} + \Delta\sigma_{Ty} + \Delta\sigma_{Fy} \quad \text{..... (4.2)}$$

$$\sigma_{xy} = \Delta\sigma_{Pxy} + \Delta\sigma_{Txy} + \Delta\sigma_{Fxy} \quad \text{..... (4.3)}$$

where:

σ_H is the in-situ maximum horizontal stress;

σ_h is the minimum in-situ horizontal stress;

$\Delta\sigma_P$ is the change of stress due to pore pressure change;

$\Delta\sigma_T$, the change of stress due to temperature change;

$\Delta\sigma_F$ is the change of stress due to the presence of the fracture

(Index: *H*: maximum horizontal; *h*: minimum horizontal; *p*: due to pore pressure; *F*: due to fracture).

For the convenience of analysis and programming, the stresses around a hydraulically induced fracture are expressed in the elliptical coordinates system as shown in Fig. 4.1. Elliptic coordinates are a two dimensional orthogonal coordinate system in which the coordinate lines are confocal ellipses and hyperbolae. The tow foci are generally taken to be fixed at $-L_f$ and L_f (fracture half length) respectively on x-axis of the Cartesian coordinate system.

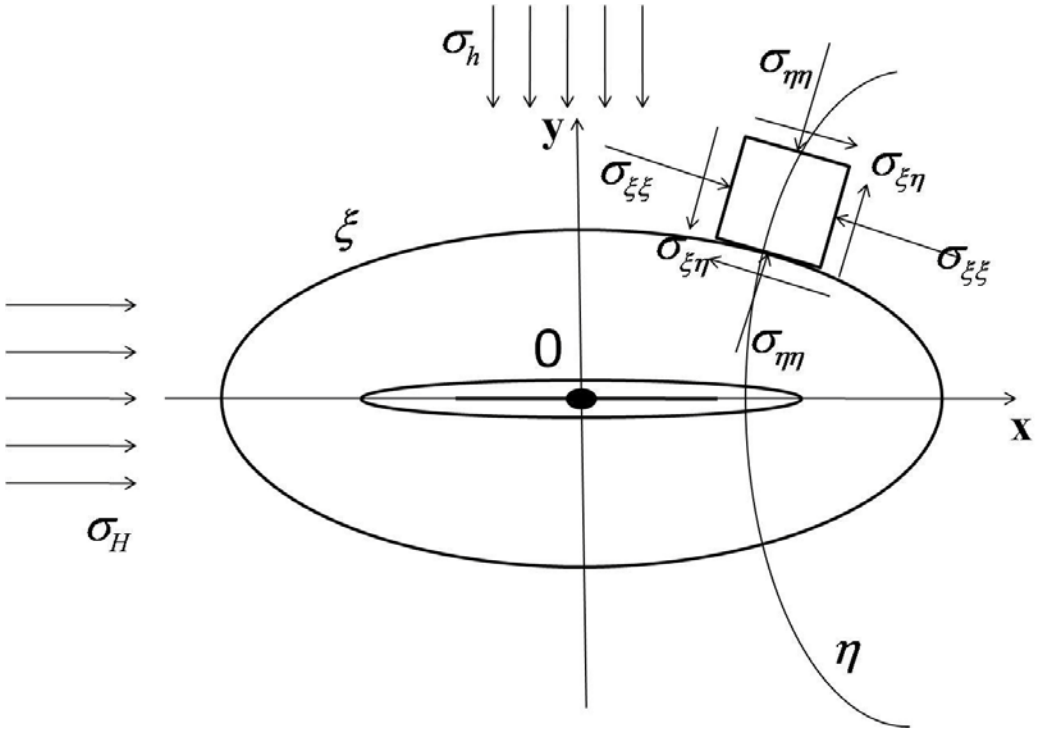

Fig.4.1 Stresses in Elliptical Coordinates System

In the following analysis for the induced stresses from pore pressure, temperature variations and fracture compression are cited from relative references and all expressions are converted into the same Cartesian coordinate system for the convenience of calculations and programming.

4.2 Poroelastic Stresses

The stresses induced by the pore pressure variation around a hydraulic fracture were given by Koning (1985). And the analytical fracture propagation model was constructed by him with the following assumptions.

1) A vertical fracture confined to the pay zone with fixed height and the geometry of PKN model extends laterally from a single well to an infinite reservoir.
2) The fracture has an infinite conductivity and the fluid pressure along the fracture length keeps constant.
3) The total leak-off rate equals to the constant injection rate.
4) The fracture propagates slow enough that the pressure distribution around the fracture behaves as quasi steady state. And the transient pressure distribution far away from the fracture moves radially outwards into the reservoir.
5) The fluid flow system can be separated into different elliptic zones as shown in Fig.3.1.

With the assumptions the stresses at any point (ξ, η) in the pressure affected region $0 \le \xi \le \xi_2$ surrounding the fracture is solving the poroelastic stress-strain relations and are given by (Koning, 1985):

$$\frac{(1-\nu)}{EJ}\Delta\sigma_{\xi p}^{(m)} = \frac{1}{g^2}\Phi_{\xi\xi}^{(m)} - \frac{L_f^2}{2}\frac{\sinh 2\xi}{g^4}\Phi_{\xi}^{(m)} + \frac{L_f^2}{2}\frac{\sin 2\eta}{g^4}\Phi_{\eta}^{(m)} + \Delta p^{(m)}(\xi) \text{.....} \quad (4.4)$$

$$\frac{(1-\nu)}{EJ}\Delta\sigma_{\eta p}^{(m)} = \frac{1}{g^2}\Phi_{\eta\eta}^{(m)} + \frac{L_f^2}{2}\frac{\sinh 2\xi}{g^4}\Phi_{\xi}^{(m)} - \frac{L_f^2}{2}\frac{\sin 2\eta}{g^4}\Phi_{\eta}^{(m)} + \Delta p^{(m)}(\xi) \text{ .....} \quad (4.5)$$

$$\frac{(1-\nu)}{EJ}\Delta\sigma_{\xi\eta p}^{(m)} = \frac{1}{g^2}\Phi_{\xi\eta}^{(m)} - \frac{L_f^2}{2}\frac{\sin 2\eta}{g^4}\Phi_{\xi}^{(m)} - \frac{L_f^2}{2}\frac{\sinh 2\xi}{g^4}\Phi_{\eta}^{(m)} \text{ .....} \quad (4.6)$$

The linear coefficient of pore pressure expansion J is used as:

$$J = \frac{(1-2\nu)}{E} - \frac{c_{gr}}{3} \text{ .....} \quad (4.7)$$

And where the superscript (m) is associated with the subregions:

$$\begin{aligned} m &= 1;\ \xi_1 \le \xi < \xi_2 \\ &= 2;\ \xi_0 \le \xi < \xi_1 \\ &= 3;\ 0 \le \xi < \xi_0 \end{aligned} \quad \text{..... (4.8)}$$

and:

$$\Phi_{\xi\xi}^{(m)} = -\frac{L_f^2}{2}\Delta p(\xi)\cosh 2\xi + \cos 2\eta(4A_1^{(m)}e^{-2\xi} + 4A_2^{(m)}\cosh 2\xi) \text{ ..... (4.9)}$$

$$\Phi_{\eta\eta}^{(m)} = \cos 2\eta[\frac{L_f^2}{2}\Delta p(\xi) - 4A_1^{(m)}e^{-2\xi} - 4A_2^{(m)}\cosh 2\xi] \text{ ..... (4.10)}$$

$$\Phi_{\xi\eta}^{(m)} = \sin 2\eta[\frac{L_f^2}{4}\frac{\partial[\Delta p(\xi)]}{\partial\xi} + 4A_1^{(m)}e^{-2\xi} - 4A_2^{(m)}\sinh 2\xi] \text{.....(4.11)}$$

$$\Phi_{\eta}^{(m)} = \sin 2\eta[\frac{L_f^2}{4}\Delta p(\xi) - 2A_1^{(m)}e^{-2\xi} - 2A_2^{(m)}\cosh 2\xi] \text{.....(4.12)}$$

$$\begin{aligned} \Phi_{\xi}^{(m)} = &-\frac{L_f^2}{2}\int_0^{\xi}[\Delta p(\xi)\cosh 2\xi]d\xi + \cos 2\eta[-\frac{L_f^2}{8}\frac{\partial[\Delta p(\xi)]}{\partial\xi} \\ &- 2A_1^{(m)}e^{-2\xi} + 2A_2^{(m)}\sinh 2\xi] \end{aligned} \text{.....(4.13)}$$

in which:

$$\begin{aligned} &\int_0^{\xi}[\Delta p(\xi)\cosh 2\xi]d\xi = \frac{1}{2}\Delta p(\xi)\sinh 2\xi - \frac{1}{4}\frac{\partial[\Delta p(\xi)]}{\partial\xi}[\cosh 2\xi - 1] \\ &\frac{\partial[\Delta p(\xi)]}{\partial\xi} = -\frac{i_w}{2\pi h\lambda_m} \end{aligned} \text{.....(4.14)}$$

The pore pressure variations are given:

$$\begin{aligned} \Delta p(\xi) &= \Delta p^{(1)}(\xi);\ \xi_1 \le \xi < \xi_2 \\ &= \Delta p^{(2)}(\xi);\ \xi_0 \le \xi < \xi_1 \\ &= \Delta p^{(3)}(\xi);\ 0 \le \xi < \xi_0 \\ &= 0;\ \xi \ge \xi_2 \end{aligned} \text{.....(4.15)}$$

and:

$$A_1^{(3)} = \frac{i_w L_f^2}{32\pi h}[\frac{1}{\lambda_3}] \text{.....(4.16)}$$

$$A_1^{(2)} = A_1^{(3)} + \frac{i_w L_f^2}{32\pi h}[\frac{1}{\lambda_2} - \frac{1}{\lambda_3}]\cos h2\xi_0 \quad \text{.....(4.17)}$$

$$A_1^{(1)} = A_1^{(2)} + \frac{i_w L_f^2}{32\pi h}[\frac{1}{\lambda_1} - \frac{1}{\lambda_2}]\cos h2\xi_1 \text{.....(4.18)}$$

$$A_2^{(1)} = -\frac{i_w L_f^2}{32\pi h}[\frac{1}{\lambda_1}]e^{-2\xi_2} \text{.....(4.19)}$$

$$A_2^{(2)} = A_2^{(1)} + \frac{i_w L_f^2}{32\pi h}[\frac{1}{\lambda_1} - \frac{1}{\lambda_2}]e^{-2\xi_1} \text{.....(4.20)}$$

$$A_2^{(3)} = A_2^{(2)} + \frac{i_w L_f^2}{32\pi h}[\frac{1}{\lambda_2} - \frac{1}{\lambda_3}]e^{-2\xi_0} \text{.....(4.21)}$$

While in the pressure unaffected region $\xi \geq \xi_2$, the stress changes:

$$\frac{(1-\nu)}{EJ}\Delta\sigma_{\xi p}^{(0)} = \frac{1}{g^2}\Phi_{\xi\xi}^{(0)} - \frac{L_f^2}{2}\frac{\sinh 2\xi}{g^4}\Phi_{\xi}^{(0)} + \frac{L_f^2}{2}\frac{\sin 2\eta}{g^4}\Phi_{\eta}^{(0)} \text{.....(4.22)}$$

$$\frac{(1-\nu)}{EJ}\Delta\sigma_{\eta p}^{(0)} = \frac{1}{g^2}\Phi_{\eta\eta}^{(0)} + \frac{L_f^2}{2}\frac{\sinh 2\xi}{g^4}\Phi_{\xi}^{(0)} + \frac{L_f^2}{2}\frac{\sin 2\eta}{g^4}\Phi_{\eta}^{(0)} \text{.....(4.23)}$$

$$\frac{(1-\nu)}{EJ}\Delta\sigma_{\xi\eta p}^{(0)} = \frac{1}{g^2}\Phi_{\xi\eta}^{(0)} - \frac{L_f^2}{2}\frac{\sin 2\eta}{g^4}\Phi_{\xi}^{(0)} - \frac{L_f^2}{2}\frac{\sinh 2\xi}{g^4}\Phi_{\eta}^{(0)} \text{.....(4.24)}$$

where the superscript (0) stands for the region with zero pressure change.

And the constants are:

$$\Phi_{\xi\xi}^{(0)} = 4A_3^{(0)}e^{-2\xi}\cos 2\eta; \qquad \Phi_{\eta\eta}^{(0)} = -4A_3^{(0)}e^{-2\xi}\cos 2\eta \text{.....(4.25)}$$

$$\Phi_{\xi\eta}^{(0)} = 4A_3^{(0)}e^{-2\xi}\sin 2\eta; \qquad \Phi_{\eta}^{(0)} = -2A_3^{(0)}e^{-2\xi}\sin 2\eta \text{..... (4.26)}$$

$$\Phi_{\xi}^{(0)} = -2A_3^{(0)}e^{-2\xi}\cos 2\eta + A_4^{(0)}; \quad A_3^{(0)} = A_1^{(1)} - \frac{i_w L_f^2}{32\pi h\lambda_1}\cosh 2\xi_2 \text{ ... (4.27)}$$

$$A_4^{(0)} = -\frac{L_f^2}{2}\int_0^{\xi_2}[\Delta p(\xi)\cosh 2\xi]d\xi \text{..... (4.28)}$$

The listed equations above are in elliptical coordinates system, and Koning (1985) gave transformation of the pore pressure induced stresses from elliptic coordinate system into the *x*-*y* coordinates system by the following equations (Koning, 1985).

$$\begin{aligned}\Delta\sigma_{px} &= \Delta\sigma_{\xi p} g^2 \\ \Delta\sigma_{py} &= \Delta\sigma_{\eta p} g^2 \\ \Delta\sigma_{pxy} &= \Delta\sigma_{\xi\eta p} g^2\end{aligned} \quad \text{..... (4.29)}$$

In which the metric tensor g is given:

$$g = \sqrt{\frac{L_f^2}{2}(\cosh 2\xi - \cos 2\eta)} \quad \text{..... (4.30)}$$

In our work, we deduced the stresses transformation between these two coordinate systems and the detailed deducing process can be found in Appendix C.

$$\begin{aligned}\sigma_{yy} &= \sigma_{\eta\eta}\cos 2\theta + \sigma_{\xi\eta}\sin 2\theta + (\sigma_{\xi\xi} + \sigma_{\eta\eta})\sin^2\theta \\ &= \sigma_{\eta\eta} + \sigma_{\xi\eta}\sin 2\theta + (\sigma_{\xi\xi} - \sigma_{\eta\eta})\sin^2\theta\end{aligned} \quad \text{..... (C.17)}$$

$$\sigma_{xx} = \sigma_{\xi\xi} - \sigma_{\xi\eta}\sin 2\theta - (\sigma_{\xi\xi} - \sigma_{\eta\eta})\sin^2\theta \quad \text{..... (C.18)}$$

$$\sigma_{xy} = (\sigma_{\xi\eta} - \frac{1}{2}(\sigma_{yy} - \sigma_{xx})\sin 2\theta)/\cos 2\theta \quad \text{..... (C.19)}$$

In which θ is given by:

$$\tan\theta = \frac{y}{x} = \frac{c\sinh\xi\sin\eta}{c\cosh\xi\cos\eta} \quad \text{..... (C.8)}$$

4.3 Thermoelastic Stresses

In this study, we considered the induced stresses by the variation of temperatures around the fracture. The studies of thermoelastic stresses are most investigated in the field of geothermal production (Ghassemi *et al*., 2005, 2006, and 2007). However, in

petroleum field, especially in gas shale reservoirs, due to the temperature difference between injection fluids and reservoir fluids is small, the thermoelastic effects on stress changes is less important than poroelastic stresses. Therefore, here it is assumed that the temperature distribution around the fracture is uniform and elliptically distributed. Therefore, not like the complexity of poroelastic stress changes surrounding the fracture, the thermoelastic stress changes are simpler because the temperature distribution surrounding the fracture is simply assumed to be elliptical and is only affected in the cool region as we can see from Fig.4.2 (outside the cool region are all reservoir temperature, uniform temperature distribution).

For a zone of uniform temperature change around the fracture, and assuming plane strain, the interior thermo-elastic stresses perpendicular and parallel to the major axes of the ellipse are given by the following equations (Perkinz and Gonzales, 1985).

$$\frac{(1-\nu)\Delta\sigma_{1T}}{E\beta\Delta T} = \frac{(b_0/a_0)}{1+(b_0/a_0)} + \left[\frac{1}{1+(b_0/a_0)}\right] \left(1/\left\{1+\frac{1}{2}\left[1.45\left(\frac{h}{2b_0}\right)^{0.9}+0.35\left(\frac{h}{2b_0}\right)^{2}\right]\left[1+\left(\frac{b_0}{a_0}\right)^{0.774}\right]\right\}\right) \quad \text{..... (4.31)}$$

$$\frac{(1-\nu)\Delta\sigma_{2T}}{E\beta\Delta T} = \frac{1}{1+(b_0/a_0)} + \left[\frac{(b_0/a_0)}{1+(b_0/a_0)}\right] \left(1/\left\{1+\left[1.45\left(\frac{h}{2b_0}\right)^{0.9}+0.35\left(\frac{h}{2b_0}\right)^{2}\right]\left[1+\left(1-\frac{b_0}{a_0}\right)^{1.36}\right]\right\}\right) \quad \text{..... (4.32)}$$

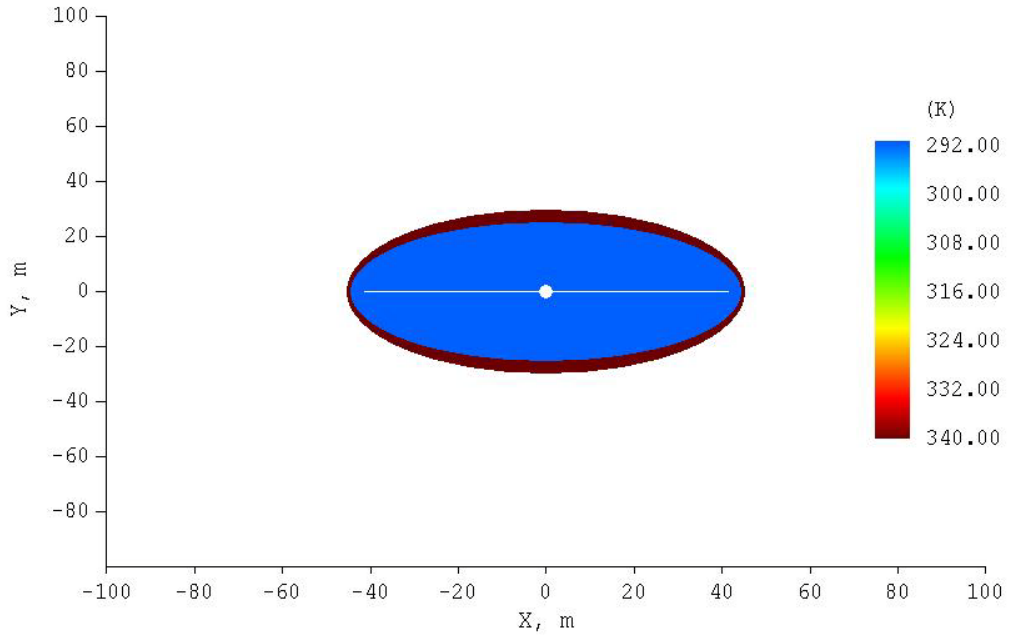

Fig.4.2 Temperature Distribution Surrounded the Fracture

Equations 4.31 and 4.32 are expressions for thermoelastic stress changes at any a point (*x*, *y*) in the cool region and can be used in equations for calculations of changed in situ stresses (see Equations 4.1-4.3). In this study, we have the expressions $\Delta\sigma_{1T} = \Delta\sigma_{Ty}$ and $\Delta\sigma_{2T} = \Delta\sigma_{Tx}$. Theses equations are expressed in X-Y coordinates, and don't need to be converted into elliptic coordinates.

4.4 Induced Stresses by Fracture Compression

In our work, the induced stresses by fracture compression are considered. On many fracture treatments, a "stress shadow" effect is clearly seen in the mapping results (Fisher *et al*., 2004). The compressive stress normal to the fracture faces is increased

above the initial in situ stress by an amount equal to the net fracturing pressure when a hydraulic fracture is opened. The induced stress perturbation is of maximum right at the fracture face and decreases out into the reservoir. This induced stress has big effect on the in situ stresses near around the fracture and so it is considered in our model.

Jaeger and Cook (1979) gave the expressions for induced stresses by fracture compression in elliptical coordinates system. They considered in situ stresses at infinity for an elliptic crack. A more direct and general solution has been reported by Pollard and Segall (1987). The expressions and results between their works are given and analyzed in our study (see Appendix C). While in this section, the analysis and equations from Pollard and Segall are given.

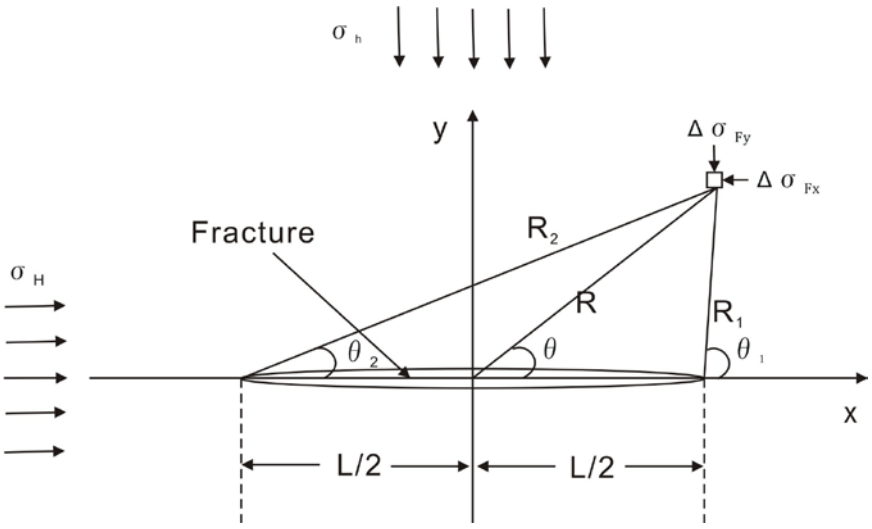

Fig.4.3 Stresses Variations due to Fracture Compression

As shown in Fig.3.6, the induced stresses by fracture compression around the fracture are analyzed. The hydraulic fracture is assumed as a 2-D crack with internal

pressure (here is the normal stress on the crack internal surface) original in situ stresses. The expressions from Pollard and Segall (1987) are given in the following.

$$\Delta\sigma_{Fx} = \Delta\sigma_I[Rr^{-1} * \cos(\theta - \Theta) - 1 - (L/2)^2 Rr^{-3} \sin\theta \sin 3\Theta] + \Delta\sigma_{II}[2Rr^{-1} * \sin(\theta - \Theta) - (L/2)^2 Rr^{-3} \sin\theta \cos 3\Theta] \quad \text{..... (4.33)}$$

$$\Delta\sigma_{Fy} = \Delta\sigma_I[Rr^{-1} * \cos(\theta - \Theta) - 1 + (L/2)^2 Rr^{-3} \sin\theta \sin 3\Theta] + \Delta\sigma_{II}[(L/2)^2 Rr^{-3} \sin\theta \cos 3\Theta] \quad \text{..... (4.34)}$$

$$\Delta\sigma_{Fxy} = \Delta\sigma_{II}[Rr^{-1} * \cos(\theta - \Theta) - 1 - (L/2)^2 Rr^{-3} \sin\theta \sin 3\Theta] + \Delta\sigma_I[(L/2)^2 Rr^{-3} \sin\theta \cos 3\Theta] \quad \text{..... (4.35)}$$

in which:

$$\Delta\sigma_I = \sigma_{11} - \sigma_{11}^{\,c}$$
$$\Delta\sigma_{II} = \sigma_{12} - \sigma_{12}^{\,c} \quad \text{..... (4.36)}$$

and $\sigma_{11}^{\,c}$ refers to the normal stress on the crack internal surface, and $\sigma_{12}^{\,c}$ refers to the shear stress on the crack internal. σ_{11} is the remote stress normal to the crack, σ_{22} is the remote parallel stress, and σ_{12} is the remote shear stress. L is the fracture length, and the geometric relations are given by the following equations: (as shown in the above figure Fig.4.3)

$$R = \sqrt{x^2 + y^2}\,, \theta = \tan^{-1}(y/x) \quad \text{..... (4.37)}$$

$$R_1 = \sqrt{y^2 + (\frac{L}{2} - x)^2}\,,\ \theta_1 = \tan^{-1}[y/(x - L/2)] \quad \text{..... (4.38)}$$

$$R_2 = \sqrt{y^2 + (x + L/2)^2}\,,\ \theta_2 = \tan^{-1}[y/(x + L/2)] \quad \text{..... (4.39)}$$

$$r = (R_1 R_2)^{1/2} \text{ and } \Theta = (\theta_1 + \theta_2)/2 \quad \text{..... (4.40)}$$

Negative values of θ, θ_1, and θ_2 should be replaced by $\pi+\theta$, $\pi+\theta_1$, and $\pi+\theta_2$ respectively, because these angles are in (0, π).

Table 4.1 Input Parameters for Simulations (Case from Perkin and Gonzalez, 1985)	
Injection condition	
Depth to the center of the formation (D):	1524m
Reservoir Thickness (h):	30.5m
Water injection rate (I_w):	477m^3/d
Time (t):	5year
Initial Reservoir temperature (T_R):	65.6°C
Bottomhole temp. of the injection water (T_w):	21.1°C
Undisturbed reservoir fluid pressure (P_R):	13.78MPa
Reservoir Rock Properties	
Compressibility of mineral grains (c_{qr}):	2.20E-05 $(MPa)^{-1}$
Compressibility of fracture (c_f):	4.080E-04$(MPa)^{-1}$
Young's modulus (E):	13.8E+03MPa
Relative perm. to water at residual oil saturation (k_{rw}) :	0.29
Residual oil saturation (S_{or}):	0.25
Initial water saturation (S_{wi}):	0.20
Rock surface energy (U):	5.0E-02 kJ/m^2
Linear coefficient of thermal expansion (β):	5.60E-06mm/ (mm*K)
Poisson's ratio (v):	0.15
Density * Specific heat of mineral grains (ρ_{qr}*C_{qr}):	2347kJ/ (m^3*K)
Minimum in-situ, total horizontal earth stress ($(\sigma_h)_{min}$):	24.1MPa
Porosity (Φ):	0.25
$(\sigma_H)_{max}$ /$(\sigma_h)_{min}$:	1.35
Reservoir permeability (k):	4.935E-14m^2
Reservoir Fluid Properties	
Compressibility of oil (c_o):	1.5E-03 $(MPa)^{-1}$
Compressibility of water (c_w):	5.20E-04 $(MPa)^{-1}$
Specific heat of oil (C_o):	2.1kJ/(kg*K)
Specific heat of water (C_w):	4.2kJ/(kg*K)
Viscosity of oil at 65.6 °C (μ_o):	1.47E-09 MPa*s
Viscos ity of water at 65.6 °C (μ_w):	4.30E-10 MPa*s
Viscosity of water at 21.1°C (μ_w):	9.95E-10 MPa*s
Density of oil (ρ_o):	881kg/m^3
Density of water (ρ_w):	1000kg/m^3

4.5 Case Study

In previous sections, the stresses around a hydraulic fracture are analyzed. The same case is used in this study as an example of the distribution of the stresses after 100 days of injection.

The poro-induced stresses distribution, thermo-induced stresses distribution and induced stresses by fracture compression separately are calculated and plotted separately. The parameters used for simulation in this case study are shown in Table.4.1.

The induced stresses by poroelasticity, thermoelasticity, and fracture compression are considered. The equations for calculating the stress distributions around the crack in Cartesian coordinates system are given by:

$$\sigma_x = \sigma_H + \Delta\sigma_{Px} + \Delta\sigma_{Tx} + \Delta\sigma_{Fx} \quad \text{..... (3.14)}$$

$$\sigma_y = \sigma_h + \Delta\sigma_{Py} + \Delta\sigma_{Ty} + \Delta\sigma_{Fy} \quad \text{..... (3.15)}$$

$$\sigma_{xy} = \Delta\sigma_{Pxy} + \Delta\sigma_{Txy} + \Delta\sigma_{Fxy} \quad \text{..... (3.16)}$$

With the current in situ stresses, the total principal stresses around the crack by stresses transformation are given:

$$\sigma_1 = \frac{1}{2}(\sigma_x + \sigma_y) + [\frac{1}{4}(\sigma_x - \sigma_y)^2 + {\sigma_{xy}}^2]^{1/2} \quad \text{..... (4.41)}$$

$$\sigma_2 = \frac{1}{2}(\sigma_x + \sigma_y) - [\frac{1}{4}(\sigma_x - \sigma_y)^2 + {\sigma_{xy}}^2]^{1/2} \quad \text{..... (4.42)}$$

And the maximum shear stresses distribution around a fracture can be given by:

$$\tau = \frac{1}{2}(\sigma_1 - \sigma_2) \quad \text{..... (4.43)}$$

Mean normal stress is given:

$$\sigma = \frac{1}{2}(\sigma_1 + \sigma_2) \quad \text{..... (4.44)}$$

where σ_H is the in-situ maximum horizontal stress, σ_h is the minimum in-situ horizontal stress; $\Delta\sigma_P$ is the change of stress due to pore pressure change; $\Delta\sigma_T$, the change of stress due to temperature change; and $\Delta\sigma_F$ is the change of stress due to the presence of the fracture (index: *H*: maximum horizontal; *h*: minimum horizontal; *p*: due to pore pressure; *F*: due to fracture). The interior thermo-elastic stresses perpendicular and parallel to the major axes of the ellipse are given by Perkinz and Gonzales (1985.). However, the induced poroelastic stresses are obtained as part of the current study.

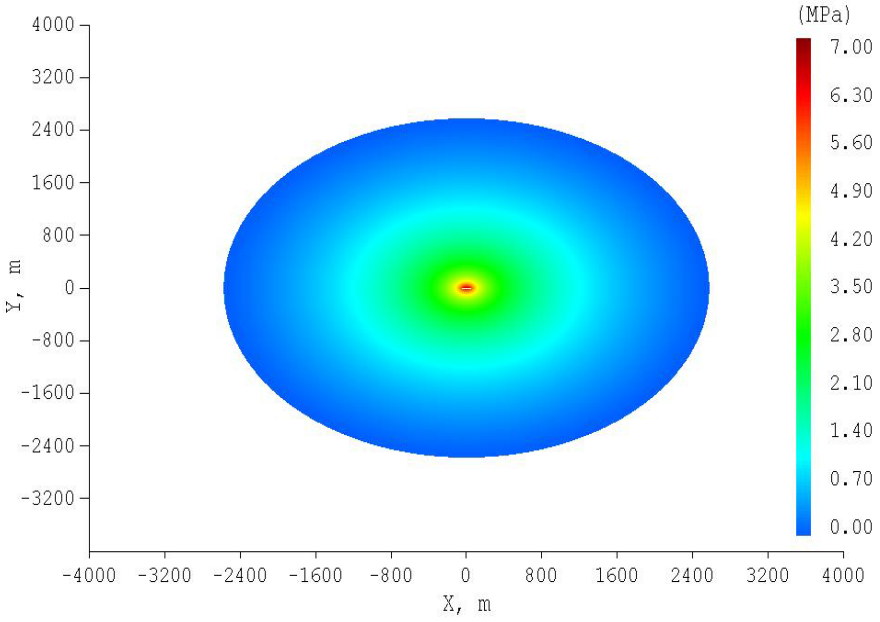

Fig.4.4 Poro-Induced Stresses Distribution X Axis Direction (t=100 days)

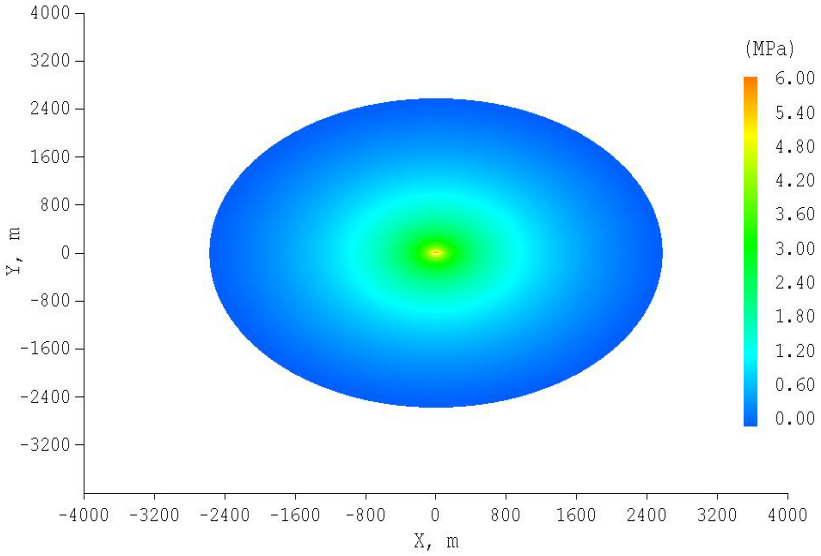

Fig.4.5 Poro-Induced Stresses Distribution Y Axis Direction (t=100 days)

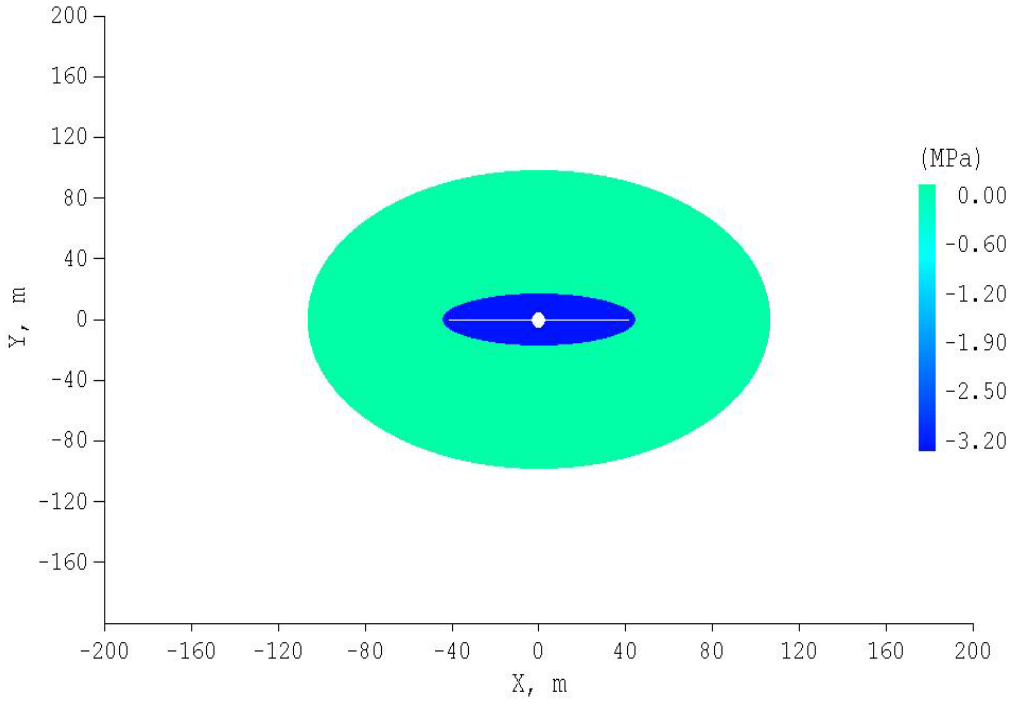

Fig.4.6 Thermo-Induced Stresses Distribution X Axis Direction (t=100 days)

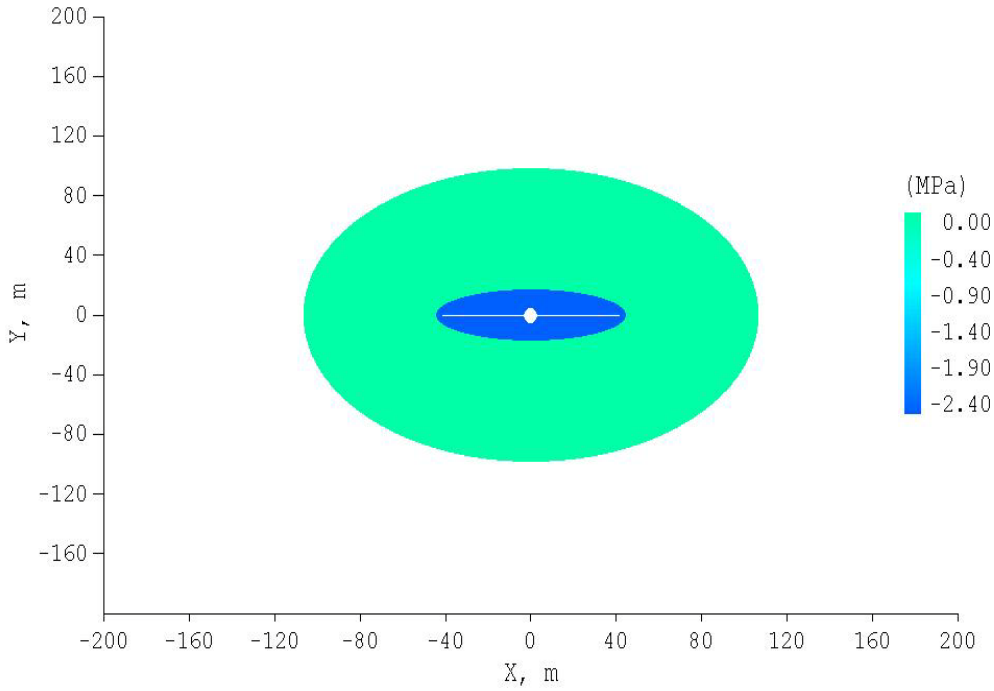

Fig.4.7 Thermo-Induced Stress Distribution Y Axis Direction (t=100 days)

Fig.4.4 and Fig.4.5 are the distributions of pore pressure induced stresses. From the plots, the poroelastic stress reaches its biggest value around the fracture surface, and decays to zero in the far field.

The thermo-induced stresses distributions are calculated by the method from P&G. From Fig.4.6 and 4.7, the contours of thermelastic stresses are plotted. It is easy to see that the thermo-induced stresses are negative near around the fracture, and are zero out of the cooled region. This is because of the assumption that the temperature is uniform in the cooled region as shown in Fig.4.2. The shapes of the distributions of thermo-induced stresses are also elliptical.

According to the equations given by Pollard and Segall (1987), the induced stresses by fracture compression are calculated and plotted for this case.

Fig.4.8, Fig.4.9 and Fig.4.10 are distributions of induced stresses by fracture compression. From these figures, the induced stresses by fracture compression on *x* and *y* axis have compressive values near fracture surface and negative values near the tips.

In Appendix C, the calculations and programming for fracture compression induced stresses around a crack are described in detail.

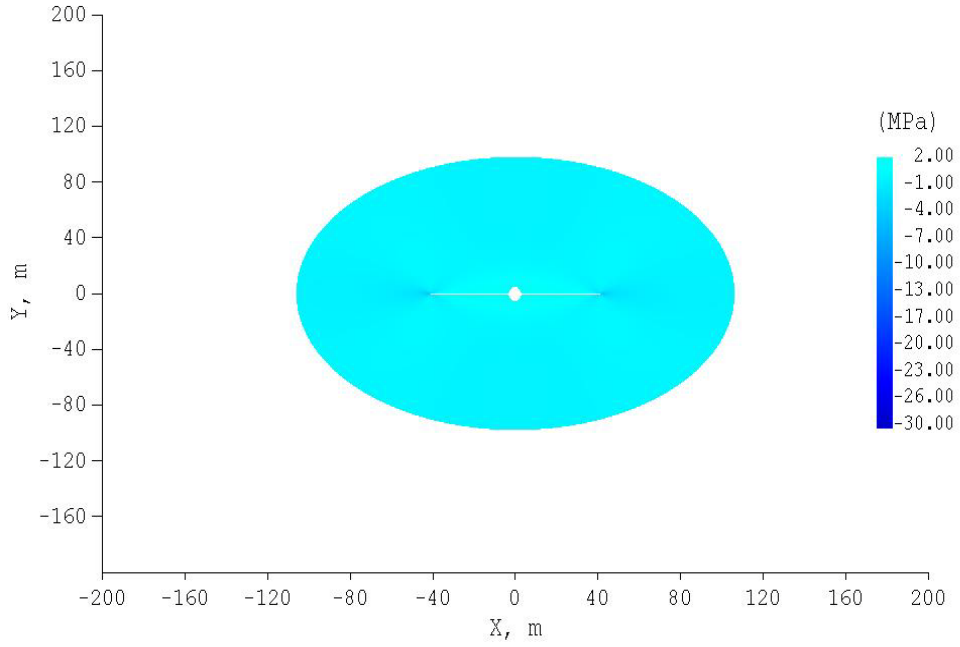

Fig.4.8 Induced Stresses Distribution by Fracture Compression in X Direction (t=100 days)

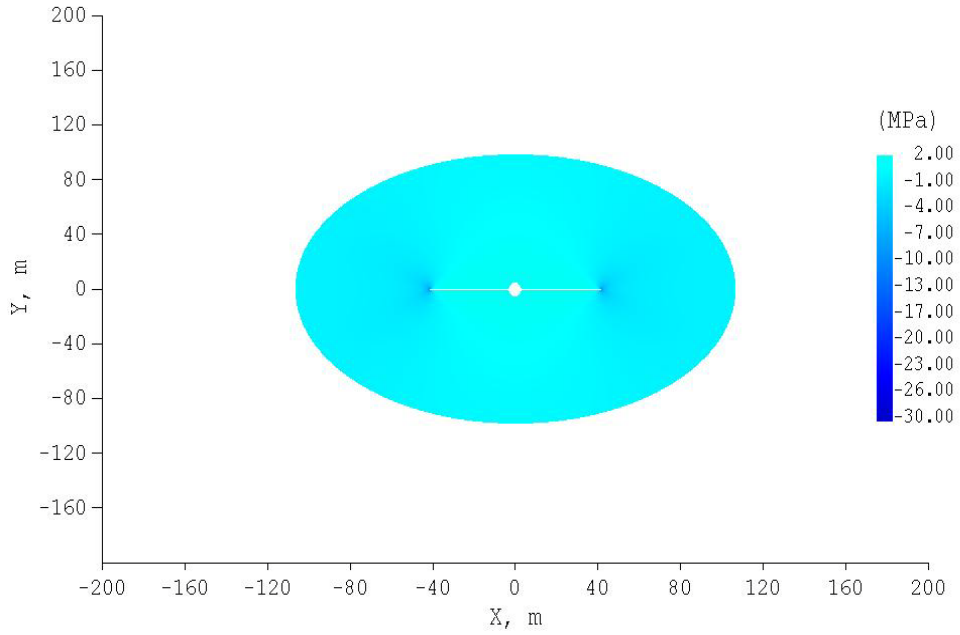

Fig.4.9 Induced Stresses Distribution by Fracture Compression in Y Direction (t=100 days)

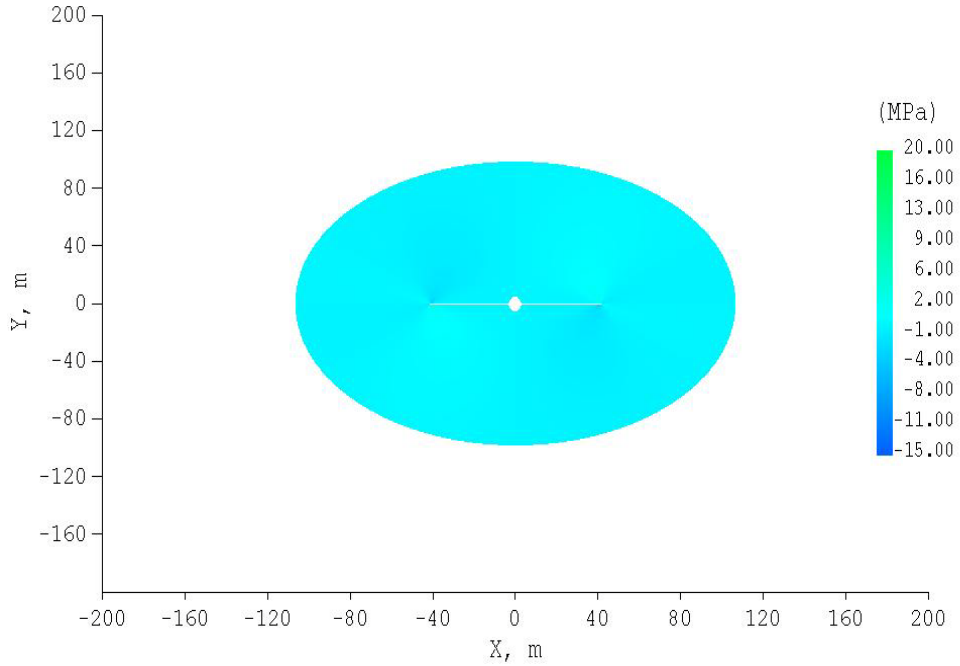

Fig.4.10 Induced Shear Stresses Distribution by Fracture Compression (t=100 days)

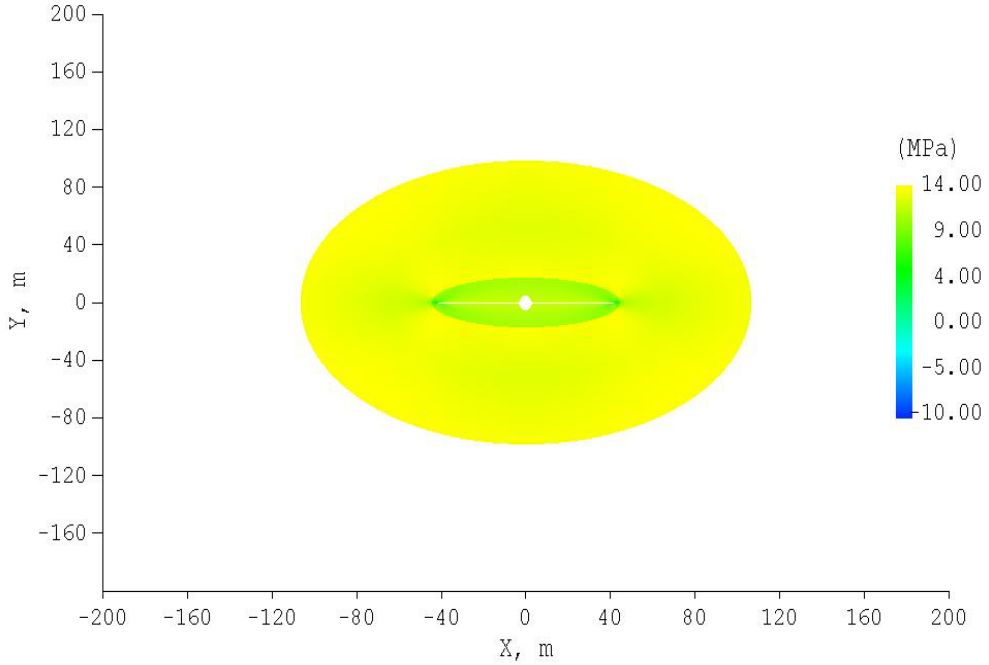

Fig.4.11 Effective Stresses Distribution around the Fracture (σ'_x) (t=100 days)

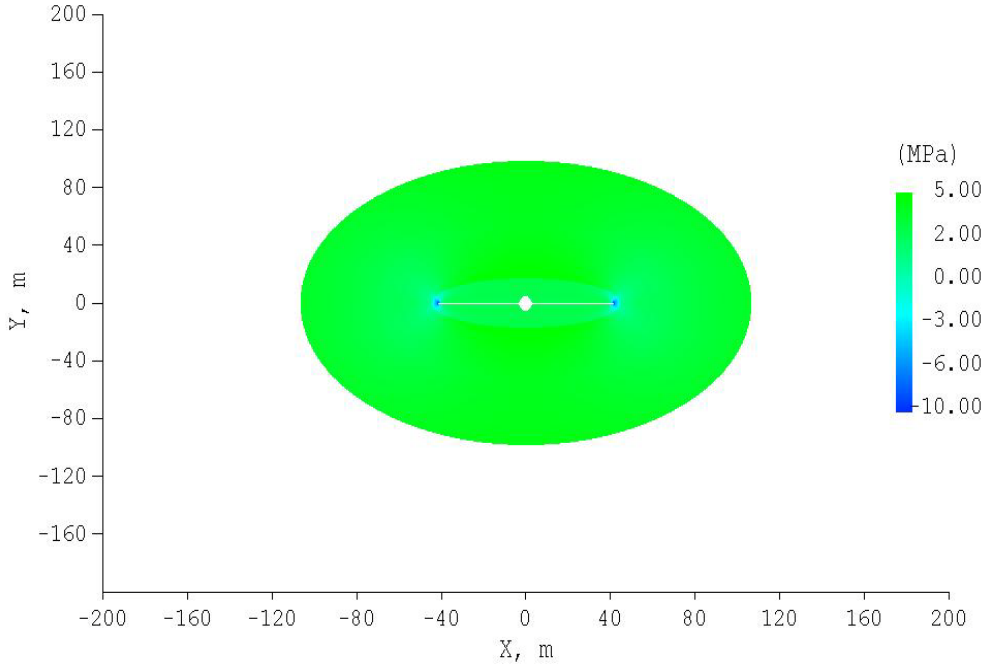

Fig.4.12 Effective Stresses Distribution around the Fracture (σ'_y) (t=100 days)

Then, according to equations 4.1-4.3, the effective stresses in *X* and *Y* directions are calculated and plotted in Fig.4.11 and 4.12.

As shown in Fig.4.11 and Fig.4.12, the distributions of effective stresses around near the fracture in *X* and *Y* directions have smaller values near the fracture tips.

4.6 Conclusions

In our study, we have developed a model (WFPSD model) for calculating the length of a water-flood induced fracture from a single well in an infinite reservoir. Similarly to Perkins and Gonzalez (1985) and Koning (1985) the model allows the leak-off distribution in the formation to be two-dimensional with the pressure transient moving elliptically outward into the reservoir with respect to the growing fracture. The model calculates the length of a water flood fracture and the extent of the cooled and flooded zones. The thermoelastic stresses are calculated by considering a cooled region of fixed thickness and of elliptical cross section. The methodology of Perkins and Gonzalez (1985) and Koning (1985) is used to calculate the fracture length, bottom-hole pressures (BHP's), and extent of the flood front as the injection process proceeds. Different from previous work, in our WFPSD model, we also calculate the pore pressure distribution around the fracture at any specific time. In addition, our model can calculate the stresses variations at any point around the fracture caused by thermoelasticity, poroelasticity, and fracture compression. The plots of stresses distributions at any specific time can be given by our model. This model is useful for investigating the response of the rock mass to stress variations resulting from pore pressure and temperature changes.

5 FAILURE POTENTIALS OF JOINTS AROUND HYDRAULIC FRACTURE

In previous sections, we have investigated the distributions of pore pressure and stresses around a hydraulically induced fracture. In the following study, shear slip or failure along planes of weakness caused by pore pressure increases during injection of fluid is investigated. Knowledge of in situ stress, and strength for the planes of weakness, is needed to predict potential failure area around the hydraulic fracture.

In this section, the pore pressure distribution after hydraulic fracturing is predicted, and the failure of joints in the reservoir formation around a hydraulic fracture is studied by constructing the Structural Permeability Diagram, by finding the critical pore pressure, and by plotting the failure potential area around hydraulic fracture.

The structural permeability diagram is a technique that can be used to show the additional pore pressure ΔP required to reactivate fabrics of different orientations (Mildren *et al*. 2002; Nelson *et al*. 2007). With the structural permeability diagram, the required minimum additional pore pressure is easy to find.

If the problem is simplified for certain sets of joints, the additional pore pressure could be found with simple calculations. And for the formation with a certain set of joints around a hydraulic fracture, the poroelastic changes of the in situ stresses are calculated, as well as the induced stresses changes by fracture compression. the failure potential area for the existing set of joints could be plotted near the fracture surface.

The failure of rock mass around the fracture is also studied to roughly predict the failure distance from the central fracture surface. It may have significant impact on permeability around a hydraulic fracture, and therefore on production. This in conjunction with the microseismic cloud is used to estimate the stimulated volume and

the resulting rock mass permeability (Palmer *et al.*, 2005; Palmer *et al.*, 2007). The injected permeability is greater than the virgin permeability, and this is interpreted as enhanced permeability due to shear or tensile failure away from the central fracture plane. In our model, the initial permeability and the fracturing geometry are given to simulate the in situ stresses variations and predict the failure zone.

5.1 Structural Permeability Diagram

Knowing the pore pressure distributions, it can be applied to determine if the joints in the reservoir around the fracture fail or not. And a structural permeability diagram can be used to show the ΔP required to reactivate fabrics of different orientations (Mildren *et al*., 2002; Nelson *et al*., 2007).

The structure permeability diagram is set up based on the dip angle δ and the angle from north to the dip direction of the joints φ (clockwise positive). Here, the dip angle refers to the angle between the joint plane and the horizontal plane; and the dip direction is really vertical to the strike of the joint.

To get the structural permeability diagram, the direction cosines of the principal stresses should be found first using the known dip angle and dip direction angle.

From Goodman (1989), the expressions for finding the direction cosines with dip angle and δ and the dip direction angle φ:

$$\begin{aligned} d_H &= \cos(90-\delta)\times\cos(90-\varphi) \\ d_h &= \cos(90-\delta)\times\sin(90-\varphi) \\ d_v &= \sin(90-\delta) \end{aligned} \quad \text{..... (5.1)}$$

in which, d_H, d_h, and d_v are direction cosines for the normal to a given weakness plane with respect to the direction of the three stresses σ_H, σ_h and σ_v. The three principal

stresses and the direction cosines of the normal to the weakness plane with respect to the principal stresses could then be decided by comparing the relative value between σ_H, σ_h and σ_v.

The equations for calculation of normal and shear stresses on a plane were given by Jaeger and Cook (1979) as the following:

$$\sigma_n = l^2\sigma_1 + m^2\sigma_2 + n^2\sigma_3$$
$$\tau = \sqrt{l^2m^2(\sigma_1-\sigma_2)^2 + n^2m^2(\sigma_3-\sigma_2)^2 + l^2n^2(\sigma_3-\sigma_1)^2} \quad \text{..... (5.2)}$$

in which, *l*, *m*, and *n* are direction cosines for a given plane to the direction of the three principal stresses.

Then, to investigate failure potentials of jointed rocks around a hydraulic fracture, the Mohr-Coulomb failure criterion is used:

$$|\tau| = c + \sigma_n' \tan\phi' \quad \text{..... (5.3)}$$

where τ is the shear stress on the joint plane, c (in some references given by τ_s) is the shear strength or cohesive strength or cohesion of that joint, σ_n' is the effective normal stress on the joint and ϕ' is the joint friction angle, and sometimes $\tan\phi'$ can be replaced by μ, the coefficient of friction.

We set up our own program in the FracJStim model for plotting the structural permeability diagram. In this section, we will compare some of our results with previous works, and apply the structural permeability diagram to some gas shale reservoirs.

To verify the calculations, the model is first applied to the special case given by Nelson *et al.* (2007) for the Cooper Basin stimulation experiment (Table.5.1). Fig.5.1 shows the structural permeability diagram for Cooper Basin from the work of Nelson *et al.* (2007). Fig.5.2 shows the structural permeability diagram for Cooper Basin from our

program. Fig.5.1 and Fig.5.2 have good agreement except a 0.2 psi/ft difference on the maximum effective treating pressure between them. This difference may be caused by different calculation process or adjustments in the software used by Nelson *et al.* (2007).

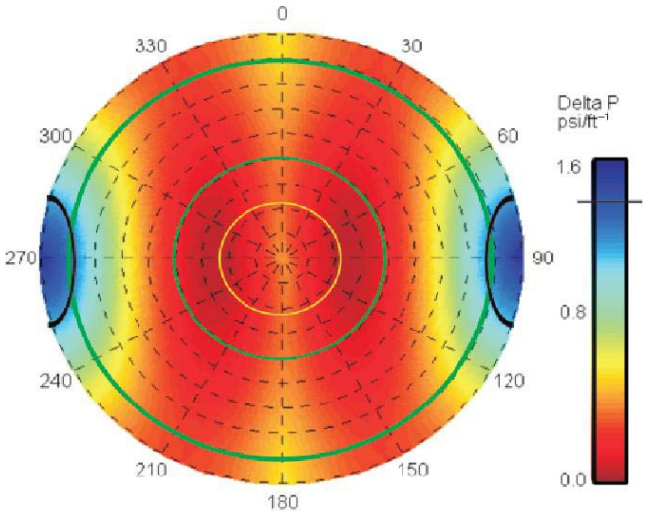

Fig.5.1 Structural Permeability Diagram for Cooper Basin (Nelson *et al.*, 2007)

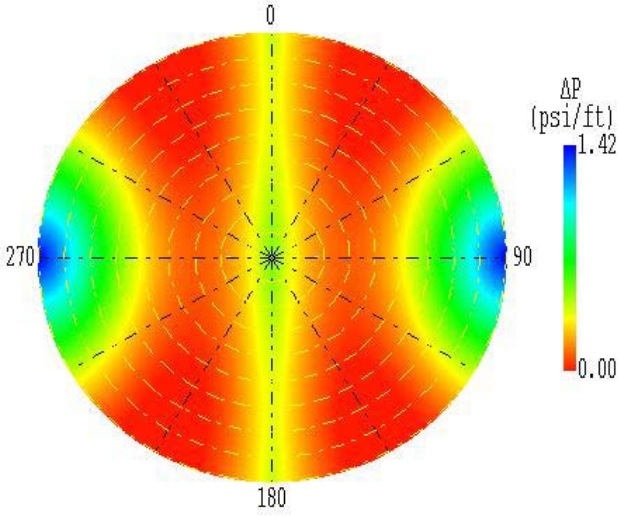

Fig.5.2 Structural Permeability Diagram for Cooper Basin (Our Program)

Table 5.1 Parameters used for Cooper Basin (Nelson *et al*., 2007)		
$\sigma_{H\max}$ (psi/ft)	1.85	E-W direction
$\sigma_{H\min}$ (psi/ft)	0.84	N-S direction
σ_V (psi/ft)	0.95	Vertical
P_p (psi/ft)	0.433	
μ	0.6	Tensile negligible
H (ft)	9800	

To further verify the results, we simulated the data of Otway Basin given by Mildren *et al*., 2005 (Table 5.2). The structural permeability maps are shown in Fig.5.3 and Fig.5.4. Minor difference can be attributed to uncertainty in the input data used. Fig.5.3 and Fig.5.4 show perfect agreement in plot shapes and values.

Table 5.2 Otway Basin Data from Mildren *et al*. (2005)		
$\sigma_{H\max}$ (MPa/km)	37.1	156 ^{o} N
$\sigma_{H\min}$ (MPa/km)	16.1	Normal to $\sigma_{H\max}$
σ_V (MPa/km)	22.4	Vertical
P_p (MPa/km)	9.8	
μ	0.8	Tensile negligible
H (km)	2.845	

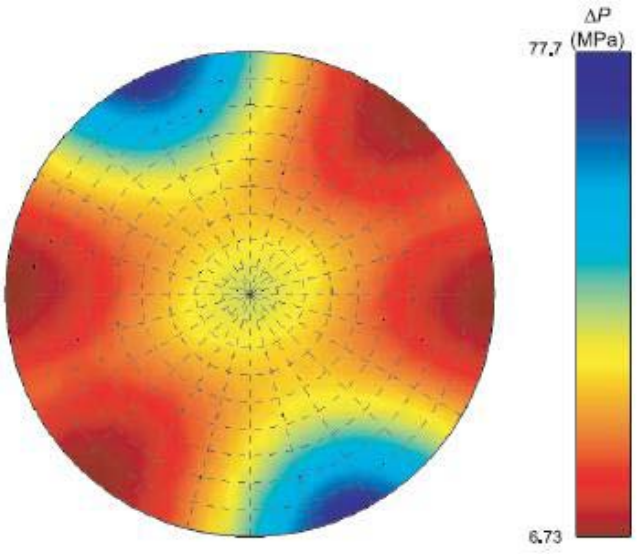

Fig.5.3 Structural Permeability Diagram for Otway Basin (Mildren *et al*., 2005)

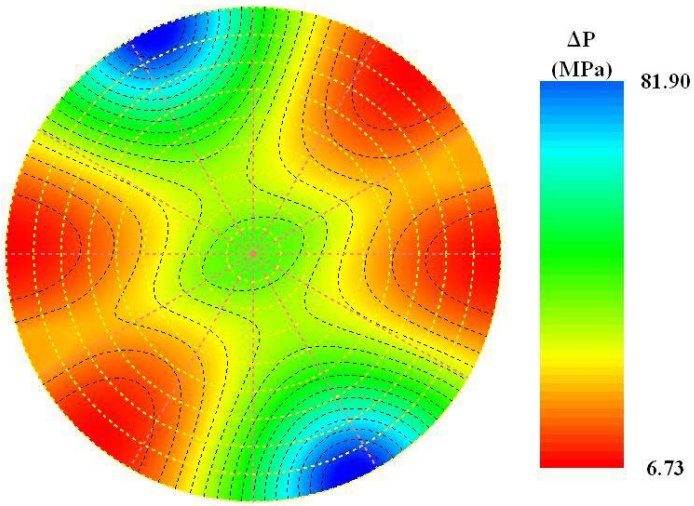

Fig.5.4 Structural Permeability Diagram for Otway Basin (Our Program)

In the following, the application of structural permeability diagram on New Albany Shale and Barnett Shale are given.

According to the data from J Ray Clark well in Christian County, KY, we assume that the principal stresses are σ_1 =2500 psi (vertical), σ_2 =2200 psi (East horizontal), σ_3 =2000 psi, and pore pressure P_p=1800 psi with μ =0.6, and cohesion zero. As shown in Fig.5.5, the maximum required effective treating pressures are located in areas with low dip angles, and the minimum required effective treating pressures are located in the areas with dip angles around 50º-70º and dip directions between -30º N and 30º N, 150º N and 210º N.

Fig.5.6 and Fig.5.7 show the sensitivity analysis of the results to the friction coefficient of joints. It can be seen that with the increase of friction coefficient, the failure of certain joints require larger effective treating pressures. This underscores the necessity of rock data for accurate prediction of stimulation requirements and outcomes.

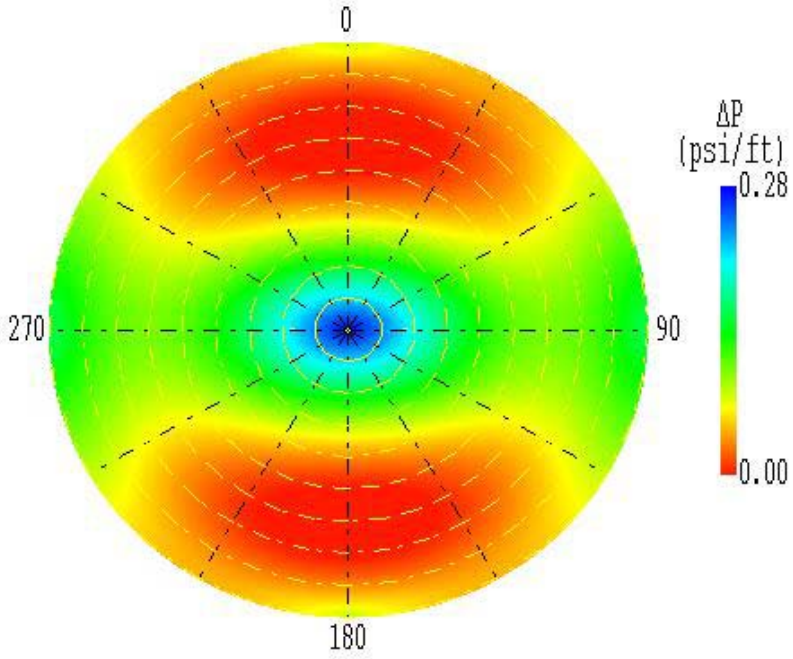

Fig.5.5 Structural Permeability Diagram for New Albany Shale (μ =0.6)

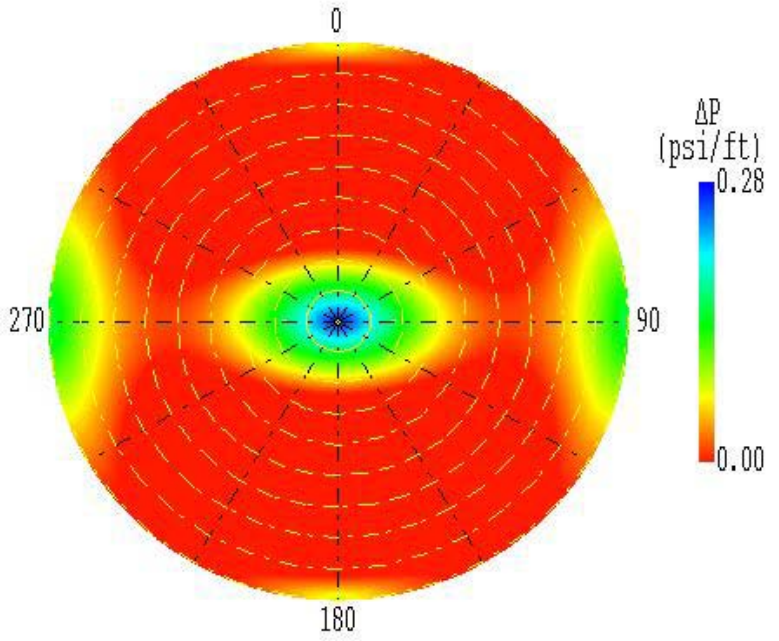

Fig.5.6 Structural Permeability Diagram for New Albany Shale (μ =0.3)

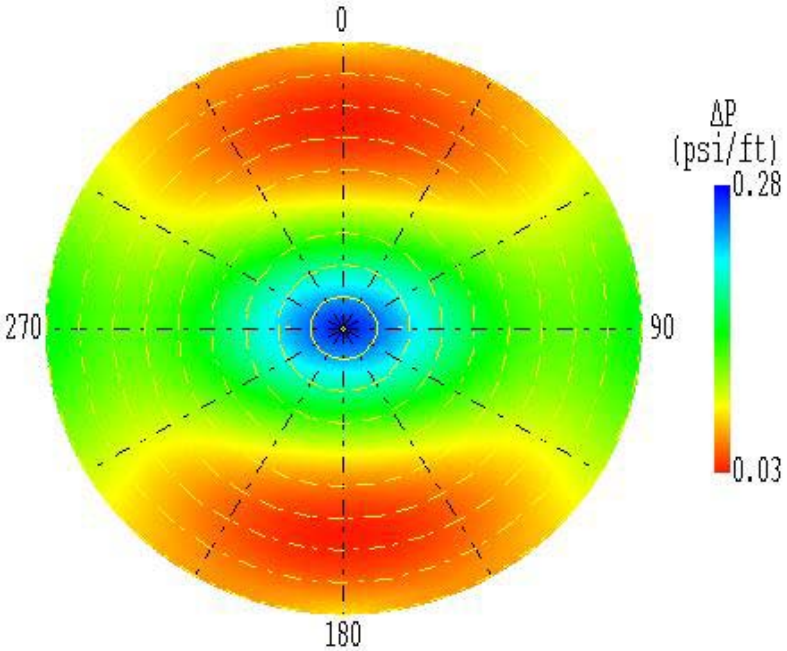

Fig.5.7 Structural Permeability Diagram for New Albany Shale (μ =0.9)

The required effective treating pressure to reactivate fabrics of different orientations of joints in the reservoir of Barnett Shale is shown in Fig.5.8 (Parameters are from Table 3.2).

In Fig.5.8, if we assume there are enough joints in the formation around the hydraulic fracture, the required effective treating pore pressure to stimulate the joints shouldn't be less than 0.06 psi/ft.

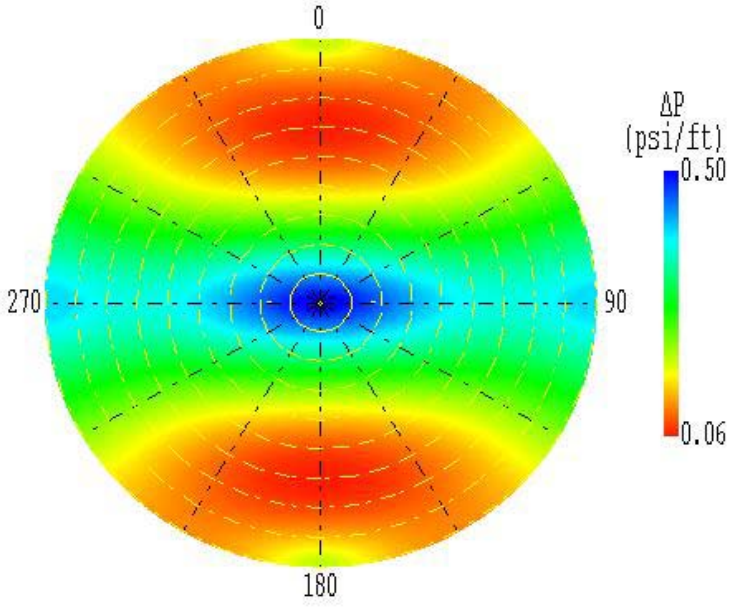

Fig.5.8 Structural Permeability Diagram Showing the Orientations of Rock Joints That May be Reactivated during Fracture Stimulation Treatments at Treating Pressures in Barnett Shale

5.2 Failure Potentials

From previous section, the structural permeability diagram shows the stimulation of joint planes by pore pressure increase without considering the pore pressure effects on the variations of in situ stresses. In fact, the stresses around a hydraulic fracture have

been changing with fracture propagation and pore pressure variation. Therefore, in the following the failure potential of joints will be discussed with considering the stresses variations.

The stresses at any point around the fracture are mainly affected by the following factors: pore pressure change, temperature change, and the presence of the fracture. The fracture compression induced stress was considered neither by Perkins and Gonzales nor by Koning. In this study, as shown in section 4, we consider 2 dimensional stresses distributions around the fracture by combing the effects from pore pressure, temperature, and fracture compression.

In order to investigate the condition for sliding across joint planes, the effective principal stresses are used by considering the effects of pore pressure. The 3D stresses distributions can also be estimated by considering the induced stress in the vertical direction, which can be the further work in the future.

In jointed rocks, the failure potentials should be analyzed by considering the joints' strike, dip and dip direction. Different joints can be theoretically expected for different slip regimes. In a normal faulting regime, joints strike in the direction of S_H with dips in the direction of S_h. For the strike-slip faulting regime the fractures will propagate in the vertical direction and strikes will generally bisect the S_H and S_h direction (Nygren and Ghassemi, 2005).

In this study, the joints are assumed to be vertical dips and the strikes of joints are assumed to have an angle β with the minimum principal stress, so that we can use the two dimensional stress distributions to estimate the failure potentials of joints.

Before determining the slip of joints, a failure criterion should be employed. There are many failure criteria for the sliding of jointed rock masses. In our study, to investigate failure potentials of jointed rocks around a hydraulic fracture, the Mohr-Coulomb failure criterion is used as shown in Eqn.5.3.

If the joint orientation β is given by the angle between the joints' orientation and the minimum principal stress as shown in Fig.5.9, by assuming this angle the slip can be determined. The normal stress and shear stress on the joints can be expressed in terms of principal stresses (assume effective) using the following transformation equations (Jaeger and Cook, 1979):

$$\sigma_n' = \frac{\sigma_1 + \sigma_3}{2} + \frac{\sigma_1 - \sigma_3}{2}\cos 2\beta \quad \text{..... (5.4)}$$

$$|\tau| = \frac{\sigma_1 - \sigma_3}{2}\sin 2\beta \quad \text{..... (5.5)}$$

Then, the failure criterion for the planes of weakness or joints Eqn.5.3 can be expressed in terms of principal stresses by applying the stress transformation equations in Eqn.5.4 and 5.5. This yield:

$$\sigma_1 - \sigma_3 = \frac{2(\tau_s + \sigma_3 \tan\varphi')}{(1 - \tan\varphi' \tan\beta)\sin 2\beta} \quad \text{..... (5.6)}$$

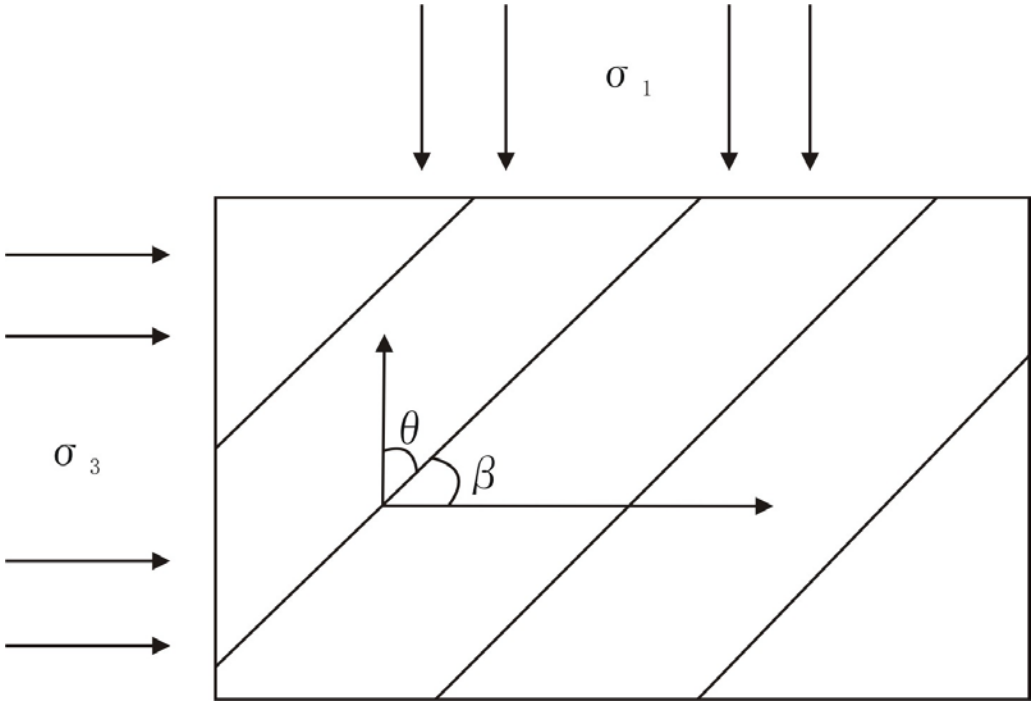

Fig.5.9 Joint Strikes in the Formation

From the previous equations, the condition for failure along the joints is that the left part is bigger than the right of the equation (Eqn.5.6). The potential for slip can then be determined by defining T_f as:

$$T_f = \sigma_1 - \sigma_3 - \frac{2(\tau_s + \sigma_3 \tan\varphi')}{(1 - \tan\varphi' \cot\beta)\sin 2\beta} \quad \text{..... (5.7)}$$

When the value of T_f is larger than 0, joint slip will occur.

By considering the varied in situ stresses around the hydraulic fracture, the failure potentials of joints in rock formations can be plotted.

For this two dimensional analysis, to compare with the structural permeability diagram, the critical pore pressure to initiate slip for a joint is studied and shown in Fig.5.10 (Nygren and Ghassemi, 2005).

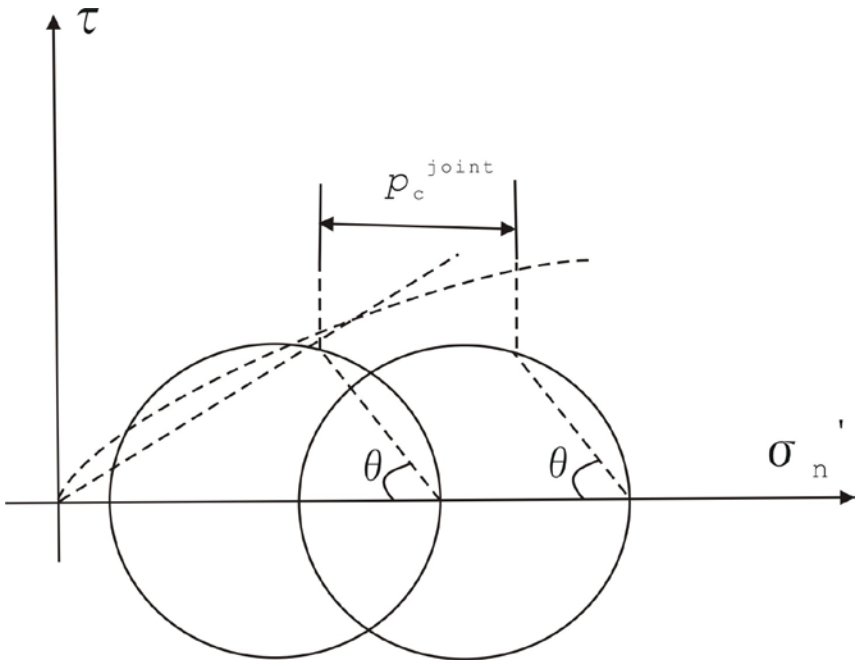

Fig.5.10 The Critical Pore Pressure for Joints (Nygren and Ghassemi, 2005)

The additional pore pressure needed to activate the joints in Fig.5.9 can be estimated by the following equation (Nygren and Ghassemi, 2005).

$$p_c^{joint} = \sigma_3 + 2S_0\left[\sin^2(90-\beta) - \frac{\sin(90-\beta)\cos(90-\beta)}{\tan\phi}\right] \quad \text{..... (5.8)}$$

in which: $S_0 = (\sigma_1 - \sigma_3)/2$.

5.3 Case Study for Barnett Shale

The model we set can be applied to check the stimulation of hydrocarbons after hydraulic fracturing operations. In our study, a field case of Barnett Shale is investigated.

The hydraulic fracture in Barnett Shale is considered a stabilized fracture after stimulation of water injection.

In the Barnett Shale, microseismic bursts are caused by shear failure on planes of weakness well outside the central fracture plane (Palmer *et al.,* 2007). Shear slip or failure along planes of weakness is instigated by pore pressure increases during injection of fracturing fluid.

As suggested by Palmer *et al.* (2007), during a fracture treatment, several things occur synergistically in the reservoir:

- From the central fracture, pressure is transmitted along natural fractures that are open (or partially open), so that pore pressure increases during fracturing operations;
- The elevated pressure causes the variations of pore pressure and in situ stresses shear or tensile failure, and enhances the permeability (especially if several small tensile fractures coalesce into a large shear fracture);
- The pressure is transmitted faster/further along the enhanced perm channels;
- The enhanced permeability depends on the pressure transient, and the pressure transient depends on the enhanced perm (i.e. they are coupled)

In tight gas reservoirs, the pore pressure is transmitted via natural fractures, because the transmission via the matrix is too slow with very low permeability. Therefore, Palmer *et al.* (2007) assumed there is a central fracture plane, oriented vertically, and that this fracture plane is the source of the pressure transient that spreads out into the reservoir, and induces shear or tensile failure.

Palmer *et al.* (2007) used the simplest slippage criterion - the linear friction law, defined by the shear strength of the weak plane and by the coefficient of friction. In their work, they have assumed for the Barnett Shale cohesion of 100 psi and friction angle of

31°. At the same time, they ignored the actual orientation of the weak planes, by assuming there are enough planes in the preferred orientation for failure that these planes dominate and govern the elliptical zone of failure.

In our study, we examined the method for critical pore pressure (Nygren and Ghassemi, 2005); the slip map of joints for various joint orientations is plotted as the pore pressure needed to reactivate the joints VS joint orientations. Fig.5.11 shows the critical pore pressure gradient for various joint orientations and friction angles.

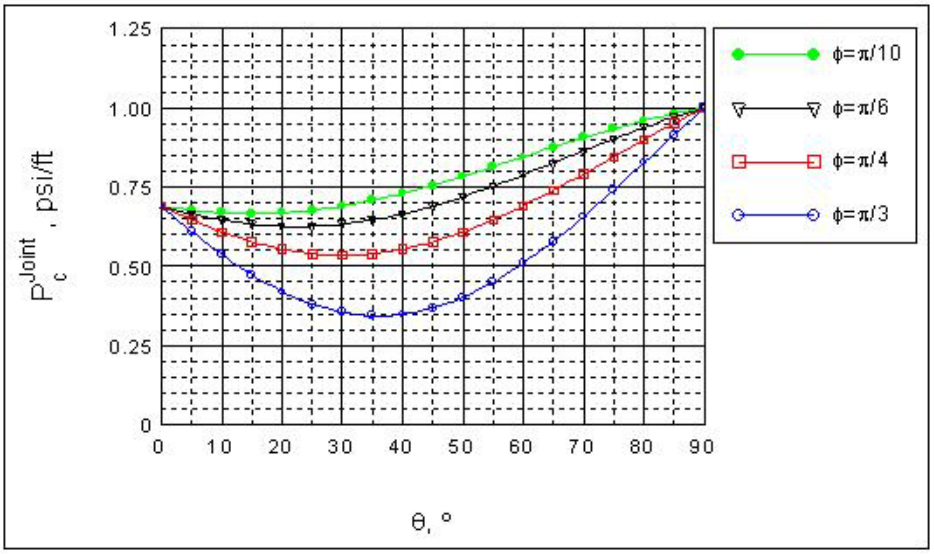

Fig.5.11 Critical Pore Pressure for Various Joints Orientations and Friction Angles

The stresses variations of Barnett Shale include the vertical stress in *z* direction by considering the induced vertical stress as Eqn.5.9.

$$\sigma_z = \sigma_v + (\Delta\sigma_x + \Delta\sigma_y)v \quad \text{..... (5.9)}$$

in which *v* is Poisson's ratio and:

$$\Delta\sigma_x = \Delta\sigma_{Px} + \Delta\sigma_{Tx} + \Delta\sigma_{Fx} \quad \text{..... (5.10)}$$

$$\Delta\sigma_y = \Delta\sigma_{Py} + \Delta\sigma_{Ty} + \Delta\sigma_{Fy} \quad \text{..... (5.11)}$$

The induced stresses by thermoelasticity are neglected because the temperature variations are relatively small in Barnett Shale. The in situ stresses profile away from the central fracture face at shut in for the case of net pressure 900 psi and permeability 1md with the parameters from Table.3.2 are plotted in Fig.5.12.

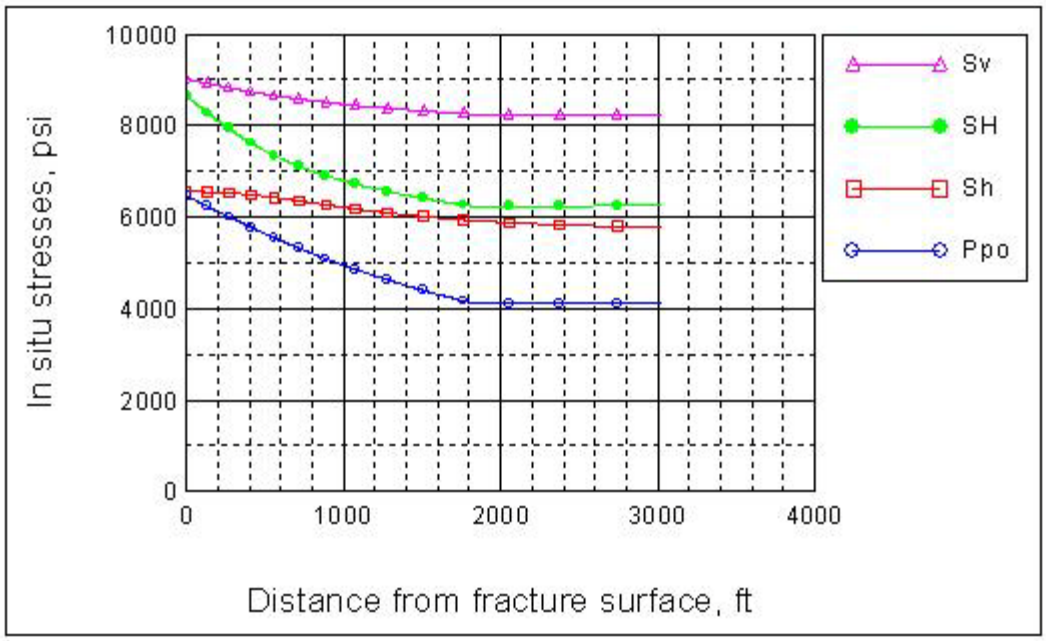

Fig.5.12 In Situ Stresses Profile away from the Central Fracture Face at Shut-in for the Case of Pnet=900 psi and K=1md

To verify the study, the in situ stresses profile away from the central fracture face at shut in for the case of net pressure 902 psi and permeability 0.99 md with the parameters from Table.3.2 are plotted in Fig.5.13 (Palmer *et al.*, 2007). Through the comparison between Fig.5.12 and Fig.5.13, we get the similar results and the validation

of our program.

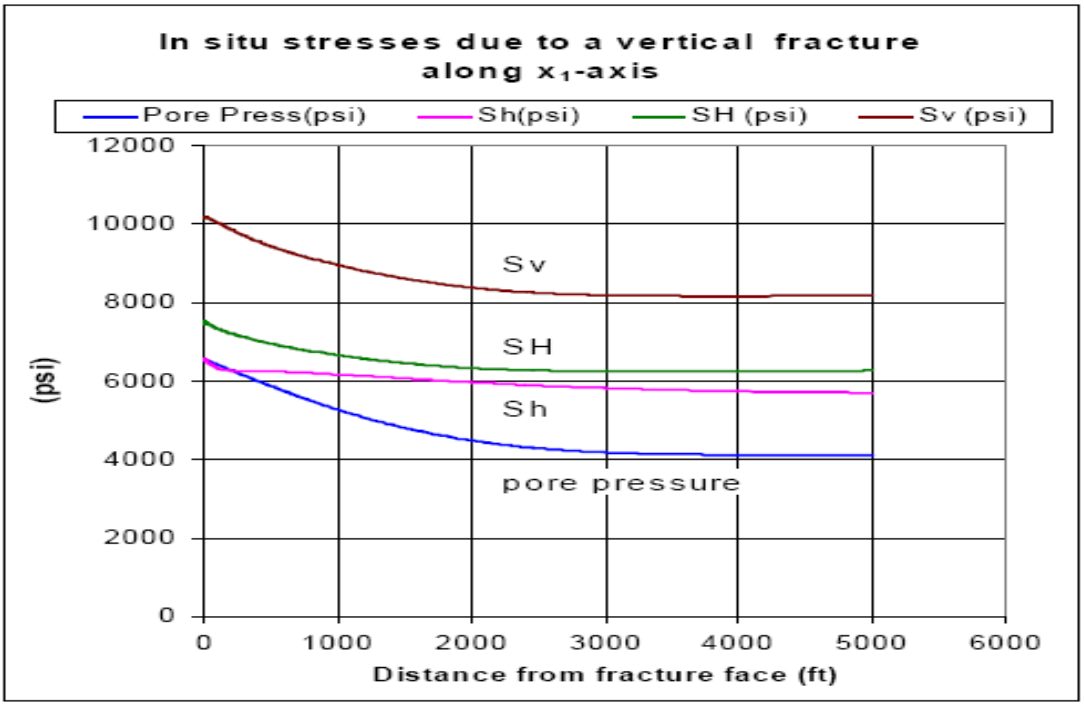

Fig.5.13 In Situ Stresses Profile away from the Central Fracture Face at Shut-in for the Case of Pnet=902 psi and K=0.99md (Palmer *et al.*, 2007)

Fig.5.14 shows us the pore pressure distribution around the fracture in Barnett Shale at water flooding time t=9 hours. The maximum pore pressure lies around the fracture surface, with a value of 6558 psi. The pore pressure is elliptically distributed around the fracture surface and is decreasing from the central fracture to the reservoir formation.

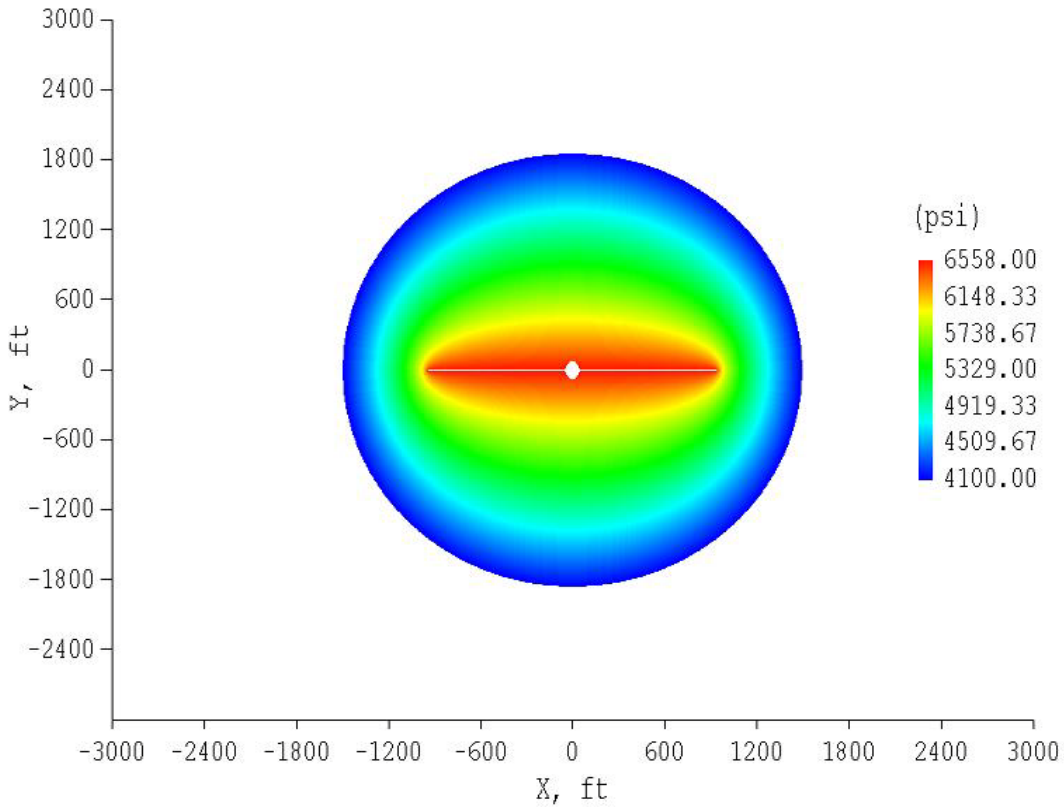

Fig.5.14 Pore Pressure Distribution around the Fracture (t=9 hours for Barnett Shale)

Fig.5.15 and Fig.5.16 are the stress distributions around the fracture in *X* and *Y*-directions. The stresses variations are calculated by induced stresses from pore pressure and fracture compression. With the parameters in Table 3.2 the stresses at any point around the fracture could be estimated.

With stresses distributions, the slip of joints can be investigated. In our study, different from what Palmer (Palmer *et al.,* 2007) did, we used Mohr-Coulomb failure criterion to determine the sliding of joints in rock formation around the hydraulically induced fracture.

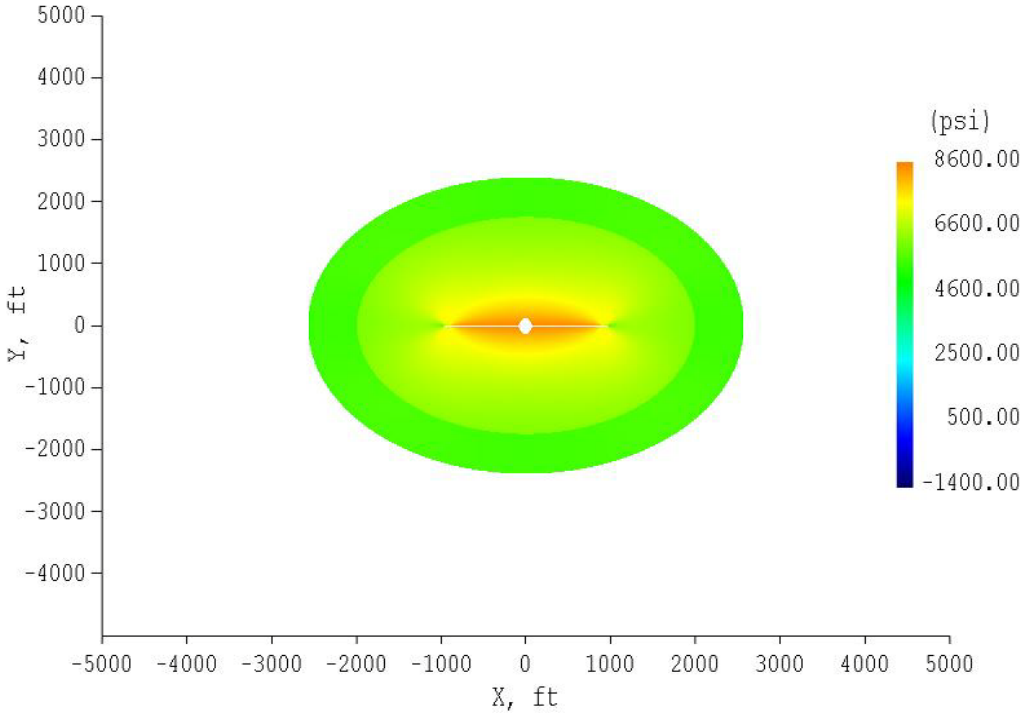

Fig.5.15 Stress Distribution around the Fracture in X-Direction

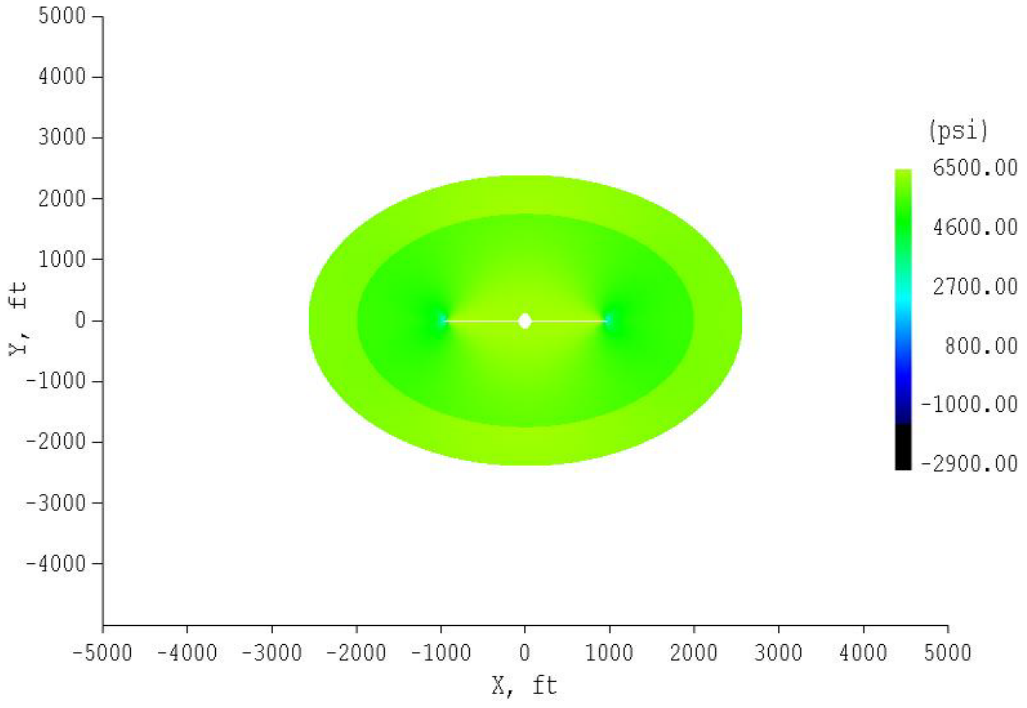

Fig.5.16 Stress Distribution around the Fracture in Y-Direction

As shown in the previous section, the failure criterion has been improved by considering all of the three principal stresses. Using Eqn.5.7 and assuming the angle β is given as $\pi/4$. The failure potentials of joints around the fracture can be plotted as Fig. 5.17.

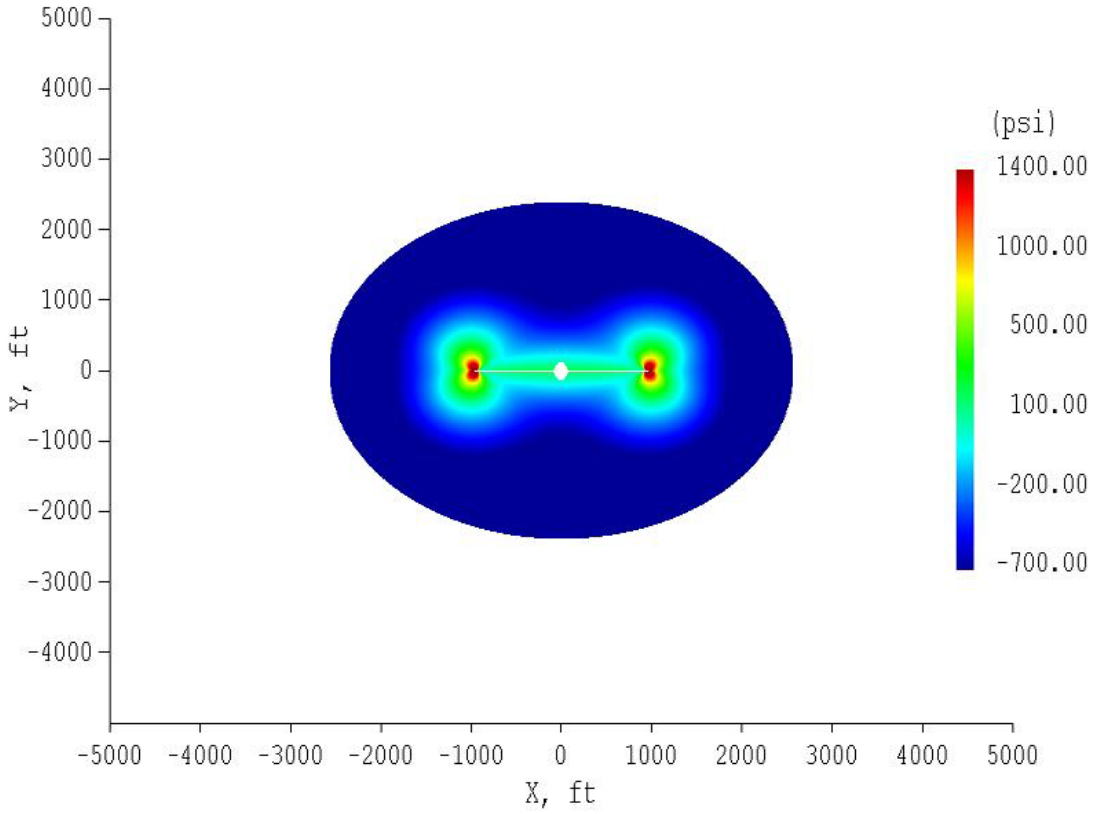

Fig.5.17 Failure Potentials for One set of Joints around Hydraulic Fracture (K=1md, Pnet=900 Psi)

Fig.5.17 shows the failure potentials for fixed joints orientations. If we don't know the orientations of joints in the rock formations, the failed reservoir volume is not easy to estimate. To simplify the calculation of failed reservoir volume and failed

distance, the failure of rock mass is investigated using Mohr-Coulomb criterion and assuming the in situ stresses are fixed. Therefore, the rock mass will fail due to the pore pressure increase after hydraulic stimulation.

The methodology of predicting the permeability in the failed region around a fracture is based on the following trial and error procedure (Palmer *et al.*, 2007):

1). An injection permeability K is guessed.

2). For a selected net fracture pressure (in the range 0 to 900 psi), the failed reservoir volume is predicted.

3). K is varied until FRV matches the particular trendline of stimulated reservoir volume (from induced seismcity) at the given net fracturing pressures.

In our study, the trendlines of the stimulated reservoir volume at given net fracturing pressures are selected and read from the Palmer's paper (Fig.5.18).

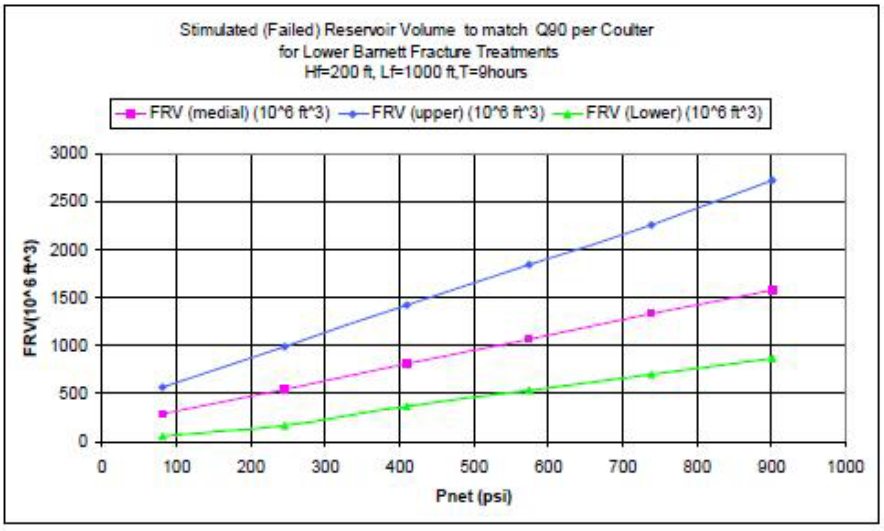

Fig.5.18 Trendlines for Failed Reservoir Volume (FRV=SRV) vs Net Fracture Pressure (Palmer *et al.*, 2007)

From previous work, we know that the elliptically distributed pore pressure is decreasing from the fracture surface to the far field (Muskat, 1937). The position of the pore pressure contour small enough such that the joints will not slip marks the boundary of the failure zone the treating pressure can create.

If we assume the failed distance is uniform along the fracture height, therefore, we can estimate the failed reservoir volume as (Fig.5.19 and Fig.5.20):

$$FRV = \pi y_d x_d h \quad \text{..... (5.12)}$$

Where y_d is the failed distance, and x_d is the failed distance in X direction, and h is assumed equal to the fracture height H_f.

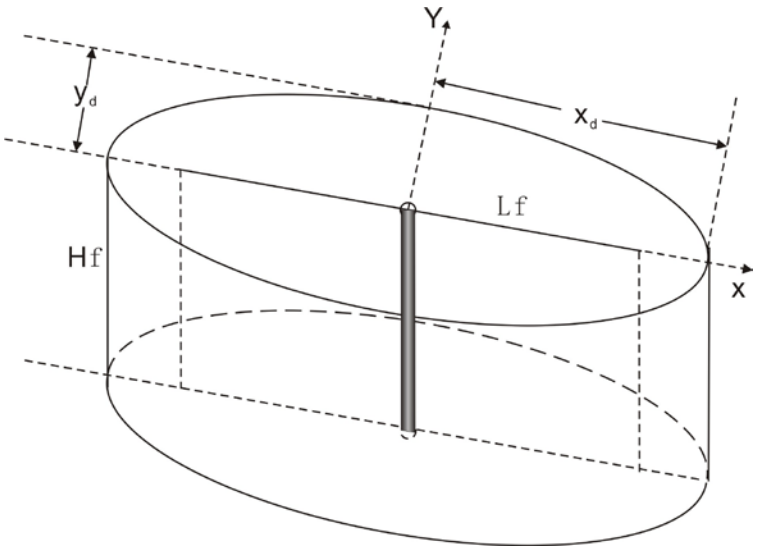

Fig.5.19 Estimation Method for Failed Reservoir Volume (for Vertical Well)

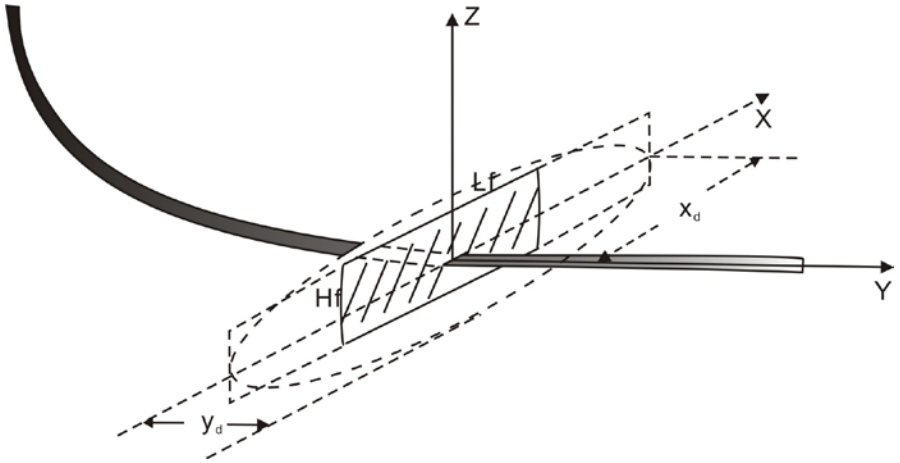

Fig.5.20 Estimation Method for Failed Reservoir Volume (for Horizontal Well)

Using the parameters for Barnett Shale in Table.3.2, the failed distance normal to the fracture surface is plotted in Fig.5.21.

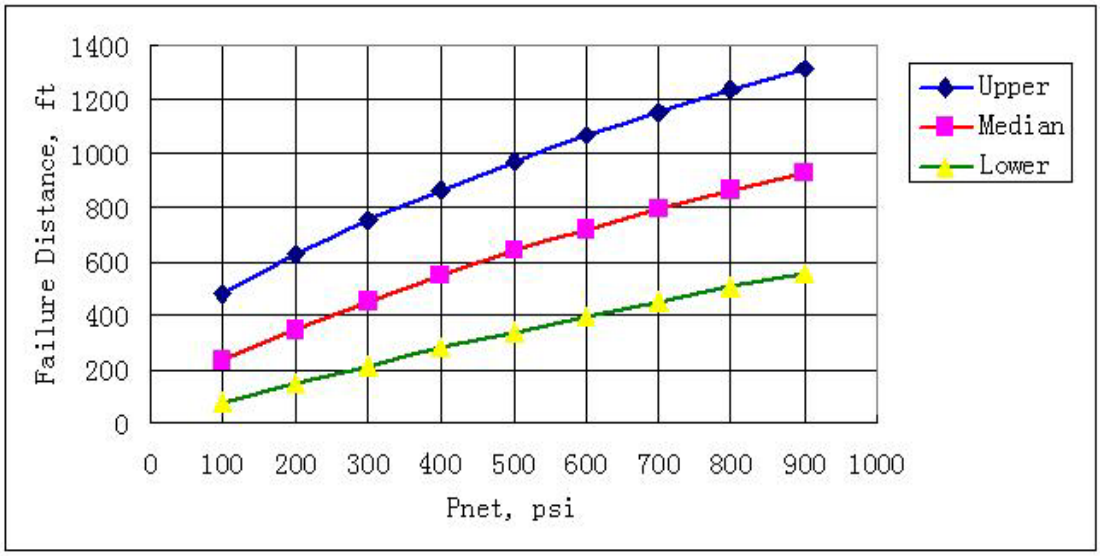

Fig.5.21 Estimated Failed Distance Normal to the Fracture Surface

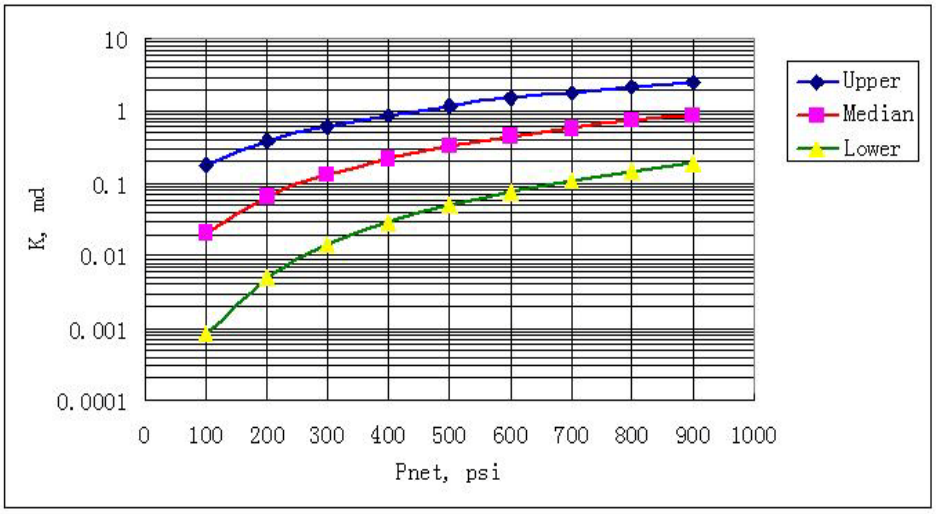

Fig.5.22 Calculated Enhanced Permeability for Barnett Shale

Knowing the failed distance, the failed reservoir volume can be calculated from equation 5.12. And by matching Fig.5.18 (Using data for a given net pressure from Fig.5.18), the enhanced permeability with net pressure is plotted in Fig.5.23.

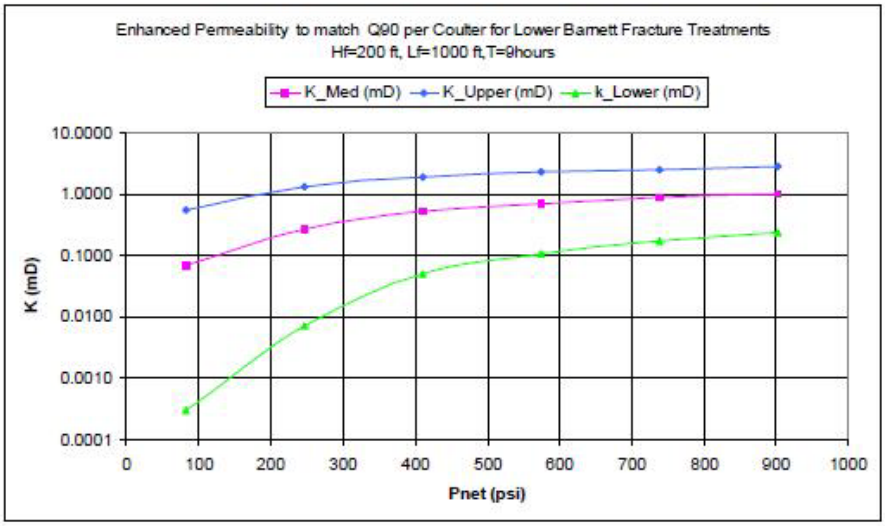

Fig.5.23 Enhanced Permeability during Injection to Match FRV for Lower Barnett Shale Fracture Treatments (Palmer *et al.*, 2007)

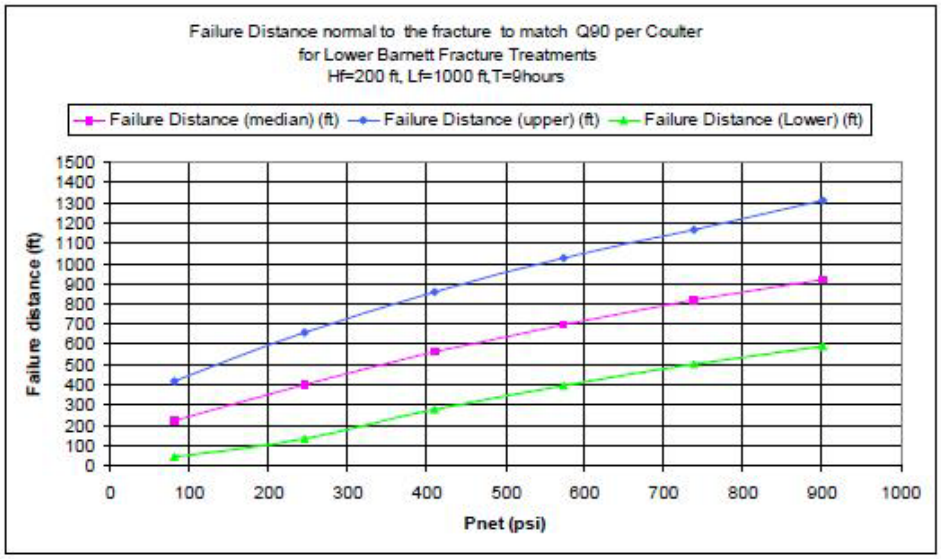

Fig.5.24 Failure Distance Normal to Central Fracture Face to Match FRV for Lower Barnett Shale Fracture Treatments (Palmer *et al.*, 2007)

Fig.5.23 and Fig.5.24 are the results of Palmer *et al*. (2007), by compare with Fig.5.21 and Fig.5.22; we can see that the difference between them can be neglect able.

5.4 Conclusions

In this section, we develop a model simulating the slip of joints around a hydraulically induced fracture from a single well in an infinite reservoir. Similarly to Perkins and Gonzalez (1985) and Koning (1985) the model allows the leak-off distribution in the formation to be two-dimensional with the pressure transient moving elliptically outward into the reservoir with respect to the growing fracture.

With a certain length of a water flood fracture, the extent of the cooled and flooded zones can be estimated. The methodology of Perkins and Gonzalez (1985) and Koning (1985) is used to calculate the dimensions of the elliptical regions, bottom-hole pressures (BHP's), and extent of the flood front as when the fracture length is reached.

The pore pressure and the stress changes at any point around the fracture caused by poroelasticiy and fracture compression are also determined.

By using the Mohr-Coulomb failure criterion, we can estimate the slip of joints in the formation around the fracture by considering the effects from pore pressure and fracture compression. The structural permeability diagram is constructed to investigate the required pore pressure to reactivate the joints around the hydraulic fracture. The failure potential for a certain set of joints is studied with considering the variations of in situ conditions. If given more assumptions, the failed reservoir volume can also be estimated by this model, and if we know the actual failed reservoir volume, we can get the enhanced permeability by the hydraulic fracture. Finally, with the data from Barnett Shale, the model is verified.

This model can also be used in other types of petroleum reservoirs as well as geothermal reservoirs.

6 SUMMARY, CONCLUSIONS AND DISCUSSION

6.1 Summary

In this research, the traditional two dimensional hydraulic fracturing propagation models are reviewed, the propagation and recession of a poroelastic PKN hydraulic fracturing model are studied, and the pore pressure and stresses distributions around a hydraulically induced fracture are researched and plotted as figures.

In my study, the distributions of pore pressure and stresses around a fracture is of interest in conventional hydraulic fracturing, fracturing during water-flooding of petroleum reservoirs, and injection/extraction operation in a geothermal reservoir. The stress and pore pressure fields are affected by: poroelastic, thermoelastic phenomena as well as by fracture opening under the combined action of applied pressure and in-situ stress. The development of two models is described in this study. One is a model of water-flood induced fracture from a single well in an infinite reservoir (Perkins and Gonzalez, 1985; Koning, 1985); it calculates the length of a water flood fracture and the extent of the cooled and flooded zones. The model allows the leak-off distribution in the formation to be two-dimensional with the pressure transient moving elliptically outward into the reservoir with respect to the growing fracture. The thermoelastic stresses are calculated by considering a cooled region of fixed thickness and of elliptical cross section. The methodology of Perkins and Gonzalez (1985) is used for calculating the fracture lengths, bottomhole pressures (BHP's), and elliptical shapes of the flood front as the injection process proceeds. However, in contrast to Perkins and Gonzalez (1985) and Koning (1985) who gave only the calculation of poroelastic changes in reservoir stress at the fracture face for a quasi steady-state pressure profile, the model allows calculation of

the pore pressure and in situ stress changes at any point around the fracture caused by thermoelasticity, poroelasticity, and fracture compression. The second model calculates the stress and pore pressure distribution around a fracture of a given length under the action of applied internal pressure and in-situ stresses as well as their variation due to cooling and pore pressure changes. It also calculates the failure potentials and slip map of joints around the fracture to determine the zone of tensile and shear failure. This is of interest in interpretation of micro-seismicity in hydraulic fracturing and in assessing permeability variation around a stimulation zone.

6.2 Conclusions

The following conclusions are drawn from this study.

1. Poroelasticity can cause a significant increase in fracturing pressure, with little effects on the fracture length and width during the fracture propagation and recession process.
2. We develop a model for calculating the length of a water-flood induced fracture from a single well in an infinite reservoir. Similarly to Perkins and Gonzalez (1985) and Koning (1985) the model allows the leak-off distribution in the formation to be two-dimensional with the pressure transient moving elliptically outward into the reservoir with respect to the growing fracture. The model calculates the length of a water flood fracture and the extent of the cooled and flooded zones. The methodology of Perkins and Gonzalez (1985) and Koning (1985) is used to calculate the fracture length, bottom-hole pressures (BHP's), and extent of the flood front as the injection process proceeds. We also calculate

the pore pressure and the stress changes at any point around the fracture caused by thermoelasticity, poroelasticity and fracture compression.

3. By using the Mohr-Coulomb failure criterion, we can estimate the failure potentials of joints and the critical pore pressure to activate joints, and if we know the failed reservoir volume, we can get the enhanced permeability by the stimulation of hydraulic fracturing operations. And this model can also be used in other types of petroleum reservoirs.

6.3 Recommendations

In the future work, the pore pressure and stresses distributions around a hydraulic fracture in P3D should be investigated.

More work should be focused on the applications for increasing the permeability of unconventional gas reservoirs.

NOMENCLATURE

a_0 and b_0 = major and minor axis of cool region ellipse (L)

a_1 and b_1 = major and minor axis of water flood ellipse (L)

a_R and b_R = major and minor axis of the elliptical zone extending to the far-field (L)

A =drainage area (L^2)

C_f = formation compressibility

C_t = system compressibility at initial reservoir conditions,

D = formation depth, (L)

E = Young's modulus

G = shear modulus of rock formation

G_f =fluid pressure gradient

h_f =fracture height, (L)

H =pay zone thickness, (L)

H_f =gross fracture height, (L)

i = time-step interval

i_{pf} =the injection rate per zone

J =pseudosteady-state productivity index, dimensionless

k =formation permeability,

k/μ =permeability/viscosity ratio

K =cohesion modulus

K_c =critical stress-intensity factor

L =length, (L)

L_f =optimal fracture half-length, (L)

$L_{(t)}$=fracture half-length at time t, (L)

p = pressure

p_0 =pressure at the wellbore

p_{ave} = reservoir average pressure

p_{BHT} = bottomhole treatment pressure

p_f =fracture pressure

p_i= initial pressure

$p(0,t)$ =pressure at the wellbore at time t

$p(X,t)$ =pressure at coordinate X at time t

Δp =pressure drop

Δp_1= difference in pressure between water flood and far-field boundaries

Δp_2= difference in pressure between cool front and water flood front

Δp_3= difference in pressure between fracture surface and cool front

Δp_f= difference in pressure between fracture surface and cool front

q =fracturing fluid flow rate

q_0 =injection rate

$q(0,t)$ =injection rate at the wellbore (x=0) at time t

r_e =reservoir drainage radius, (L)

r_w =wellbore radius, (L)

S_w =water saturation

S_{wi} =initial water saturation

t =time point during a fracture treatment

T_f =fracture temperature, ^oF

T_{pc} =pseudocritical fracture temperature, ºF

T_{pr} =reduced temperature, ºF

V =volume, ft^3

V_p =volume of proppant in pay, ft^3

V_{pf} =volume of propped fracture, ft^3

V_r =reservoir drainage volume, ft^3

w =fracture width, ft

w_j =level weighting factor

wk_f =fracture conductivity, md-ft

w_{opt}=optimal fracture width, ft

$W_{(x,t)}$ =width in elliptical fracture at time t at location X, ft

X =coordinate along direction of fracture propagation

$\Delta\sigma$ =in-situ stress differential between the potential barrier and the payzone, psi

μ_g =gas viscosity, cp

ν =Poisson's ratio

ρ =density of the fracturing fluid

σ_h =in-situ normal rock stress perpendicular to fracture face, psi

ϕ =porosity, %

REFERENCES

Abé, H., Mura, T., and Keer, L.M. 1976. Growth Rate of a Penny-Shaped Crack in Hydraulic Fracturing of Rocks. *J. Geophys. Res.* **81**. DOI: 10.1029/JB081i029p05335

Biot, M.A. 1941. General Theory of Three-Dimensional Consolidation. *Journal of Applied Physics* **12** (2): 155-164.

Cleary, M.P. 1980. Comprehensive Design Formulae for Hydraulic Fracturing. Paper presented at the SPE Annual Technical Conference and Exhibition, Dallas, Texas. 1980 Copyright 1980, American Institute of Mining, Metallurgical, and Petroleum Engineers, Inc. 9259-MS.

Daneshy, A.A. 1973. On the Design of Vertical Hydraulic Fractures. *SPE Journal of Petroleum Technology* **25** (1): 83-97. DOI: 10.2118/3654-pa

Detournay, E., Cheng, A.H.D., and Mclennan, J.D. 1990. A Poroelastic Pkn Hydraulic Fracture Model Based on an Explicit Moving Mesh Algorithm. *Journal of Energy Resources Technology-Transactions of the Asme* **112** (4): 224-230.

Economides, M.J. and Nolte, K.G. 2000. *Reservoir Stimulation*. Chichester, England ; New York: Wiley. Original edition. ISBN 0471491926 (acid-free paper).

Geertsma, J. 1957. The Effect of Fluid Pressure Decline on Volumetric Changes of Porous Rocks. *Petroleum Transactions American Institute of Mining Metallurgical and Petroleum Engineers* **210**: 331-340.

Geertsma, J. 1966. Problems of Rock Mechanics in Petroleum Production Engineering. Paper presented at the Proc. 1st Cong. of the Intl. Soc. of Rock Mech., Lisbon 585-594.

Geertsma, J. and Klerk, F.d. 1969. A Rapid Method of Predicting Width and Extent of Hydraulically Induced Fractures. *SPE Journal of Petroleum Technology* **21** (12): 1571-1581. DOI: 10.2118/2458-pa

Ghassemi, A. and Suresh Kumar, G. 2007. Changes in Fracture Aperture and Fluid Pressure Due to Thermal Stress and Silica Dissolution/Precipitation Induced by Heat Extraction from Subsurface Rocks. *Geothermics* **36** (2): 115-140.

Ghassemi, A., Tarasovs, S., and Cheng, A.H.-D. 2005. Integral Equation Solution of Heat Extraction-Induced Thermal Stress in Enhanced Geothermal Reservoirs. *International Journal for Numerical and Analytical Methods in Geomechanics* **29** (8): 829-844.

Ghassemi, A., Tarasovs, S., and Cheng, A.H.D. 2007. A 3-D Study of the Effects of Thermomechanical Loads on Fracture Slip in Enhanced Geothermal Reservoirs. *International Journal of Rock Mechanics and Mining Sciences* **44** (8): 1132-1148.

Ghassemi, A. and Zhang, Q. 2006. Porothermoelastic Analysis of the Response of a Stationary Crack Using the Displacement Discontinuity Method. *Journal of Engineering Mechanics* **132** (1): 26-33.

Jaeger, J.C. and Cook, N.G.W. 1979. *Fundamentals of Rock Mechanics*. Science Paperbacks. London: Chapman and Hall. Original edition. ISBN 0412220105 (pbk.).

Jaeger, J.C., Cook, N.G.W., and Zimmerman, R.W. 2007. *Fundamentals of Rock Mechanics*. Malden, MA: Blackwell Pub. Original edition. ISBN 9780632057597 (pbk. alk. paper).

Khristianovitch, S.A. and Zheltov, Y.P. 1955. Hydraulic Fracture of an Oil-Bearing Bed. . *Izvest. Akad. Nauk SSR, OTN* **5**: 3-41.

Koning, E.J.L. 1985. Fractured Water Injection Wells - Analytical Modelling of Fracture Propagation. Society of Petroleum Engineers 14684-MS.

Legarth, B., Huenges, E., and Zimmermann, G. 2005. Hydraulic Fracturing in a Sedimentary Geothermal Reservoir: Results and Implications. *International Journal of Rock Mechanics and Mining Sciences* **42** (7-8): 1028-1041.

Maugis, D. 1992. Stresses and Displacements around Cracks and Elliptical Cavities: Exact Solutions. *Engineering Fracture Mechanics* **43** (2): 217-255.

Murphy, H. 1983. Hot Dry Rock Reservoir Development and Testing in the USA. In *Mechanics of Elastic and Inelastic Solids 5, Hydraulic Fracturing and Geothermal Energy*, ed. Namet-Nasser, S., Abé, H., and Hirakawa, S., Boston: Martinus Nijhoff Publishers.

Muskat, M. and Wyckoff, R.D. 1937. *The Flow of Homogeneous Fluids through Porous Media*. International Series in Physics. New York: McGraw-Hill. Original edition. ISBN.

Nordgren, R.P. 1972. Propagation of a Vertical Hydraulic Fracture. *SPE Journal* **12** (4): 306-314. DOI: 10.2118/3009-pa

Nygren, A. and Ghassemi, A. 2006. Poroelastic and Thermoelastic Effects of Injection into a Geothermal Reservoir. Paper presented at the Golden Rocks 2006, The 41st U.S. Symposium on Rock Mechanics (USRMS), Golden, CO. American Rock Mechanics Association 06-1053.

Palciauskas, V.V. and Domenico, P.A. 1982. Characterization of Drained and Undrained Response of Thermally Loaded Repository Rocks. *Water Resour. Res.* **18**. DOI: 10.1029/WR018i002p00281

Palisch, T.T., Vincent, M.C., and Handren, P.J. 2008. Slickwater Fracturing – Food for Thought. Paper presented at the SPE Annual Technical Conference and Exhibition, Denver, CO, USA. Society of Petroleum Engineers 115766-MS.

Palmer, I.D., Moschovidis, Z.A., and Cameron, J.R. 2005. Coal Failure and Consequences for Coalbed Methane Wells. Paper presented at the SPE Annual Technical Conference and Exhibition, Dallas, TX. Society of Petroleum Engineers 96872-MS.

Palmer, I.D., Moschovidis, Z.A., and Cameron, J.R. 2007. Modeling Shear Failure and Stimulation of the Barnett Shale after Hydraulic Fracturing. Paper presented at the SPE Hydraulic Fracturing Technology Conference, College Station, Texas, U.S.A. Society of Petroleum Engineers 106113-MS.

Perkins, T.K. and Gonzalez, J.A. 1985. The Effect of Thermoelastic Stresses on Injection Well Fracturing. *SPE Journal* **25** (1): 78-88. DOI: 10.2118/11332-pa

Perkins, T.K. and Kern, L.R. 1961. Widths of Hydraulic Fractures. *SPE Journal of Petroleum Technology* **13** (9): 937-949. DOI: 10.2118/89-pa

Pollard, D.D. and Segall, P. 1987. Theoretical Displacements and Stresses near Fractures Rock: With Applications to Faults, Joints, Veins, Dikes, and Solution Surfaces. In Atkinson, B.K., ed., *Fracture Mechanics of Rocks*, New York: Academic Press.

Rice, J.R. and Cleary, M.P. 1976. Some Basic Stress Diffusion Solutions for Fluid-Saturated Elastic Porous Media with Compressible Constituents. *Rev. Geophys.* **14**. DOI: 10.1029/RG014i002p00227

Settari, A. 1980. Simulation of Hydraulic Fracturing Processes. *SPE Journal* **20** (6): 487-500. DOI: 10.2118/7693-pa

Shin, K., Sugawara, K., and Okubo, S. 2001. Application of Weibull's Theory to Estimating in Situ Maximum Stress [Sigma]H by Hydrofracturing. *International Journal of Rock Mechanics and Mining Sciences* **38** (3): 413-420.

Sneddon, I.N. and Lowengrub, M. 1969. *Crack Problems in the Classical Theory of Elasticity*. The Siam Series in Applied Mathematics. New York: Wiley. Original edition. ISBN.

Timoshenko, S. and Goodier, J.N. 1951. *Theory of Elasticity*. Engineering Societies Monographs. New York: McGraw-Hill. Original edition. ISBN.

Valkó, P. and Economides, M.J. 1995. *Hydraulic Fracture Mechanics*. Chichester ; Toronto: Wiley. Original edition. ISBN 0471956643.

Veatch Jr., R.W. 1983a. Overview of Current Hydraulic Fracturing Design and Treatment Technology--Part 1. *SPE Journal of Petroleum Technology* **35** (4): 677-687. DOI: 10.2118/10039-pa

Veatch Jr., R.W. 1983b. Overview of Current Hydraulic Fracturing Design and Treatment Technology-Part 2. *SPE Journal of Petroleum Technology* **35** (5): 853-864. DOI: 10.2118/11922-pa

Warpinski, N.R. and Branagan, P.T. 1989. Altered-Stress Fracturing. *SPE Journal of Petroleum Technology* **41** (9): 990-997. DOI: 10.2118/17533-pa

Warpinski, N.R. and Teufel, L.W. 1987. Influence of Geologic Discontinuities on Hydraulic Fracture Propagation (Includes Associated Papers 17011 and 17074). *SPE Journal of Petroleum Technology* **39** (2): 209-220. DOI: 10.2118/13224-pa

Warpinski, N.R., Wolhart, S.L., and Wright, C.A. 2001. Analysis and Prediction of Microseismicity Induced by Hydraulic Fracturing. Paper presented at the SPE Annual Technical Conference and Exhibition, New Orleans, Louisiana. Copyright 2001, Society of Petroleum Engineers Inc. 71649-.

Yew, C.H. 1997. *Mechanics of Hydraulic Fracturing*. Houston, Tex.: Gulf Pub. Original edition. ISBN 0884154742 (alk. paper).

APPENDIX A

MECHANICS OF TRADITIONAL 2D HYDRAULIC FRACTURE PROPAGATION MODELS

The mechanics of traditional 2D hydraulic fracture propagation models are reviewed in the following.

First, let's come to the PKN model, the maximum width in the elliptical fracture is given by Eqn.1.1 (from Perkins and Kern 1961).

$$w_{(X,t)} = \frac{(1-\nu) h_f \left(p_f - \sigma_h \right)}{G} \quad \text{..... (A.1)}$$

where ν is the Poisson's ratio, σ_h the minimum in-situ rock stress perpendicular to the fracture face, and *G* the shear modulus of the rock formation.

The term *X* is the coordinate along the direction of fracture propagation. The pressure drop in the *X* direction is determined by the flow resistance in a narrow, elliptical flow channel.

$$\frac{\partial \Delta p}{\partial x} = \frac{-64}{\pi} \frac{q\mu}{w^3 H} \quad \text{..... (A.2)}$$

For the PKN model, the fluid pressure at the propagating edge falls off towards the tip or leading edge. Thus for $x = L_f$, $p_f = \sigma_h$. This is based on the assumption that the fracture resistance or toughness at the tip is zero. Note that for a crack created and opened by a uniform internal pressure, the tip of the crack experiences infinite high tensile stresses. However, in this model, the stress-concentration problem at the tip is ignored.

Nordgren (1972) wrote the continuity equation:

$$\frac{\partial q}{\partial x} = -\frac{\pi h_f}{4} \frac{\partial w}{\partial t} \quad \text{..... (A.3)}$$

By using Eqn.A.1 to Eqn.A.3, we obtain a nonlinear partial-differential equation, Eqn.A.4, in terms of *w(X,t):*

$$\frac{G}{64(1-\nu)h_f \mu}\frac{\partial^2 w^2}{\partial X^2} - \frac{\partial w}{\partial t} = 0 \quad \text{..... (A.4)}$$

Consider the following initial conditions for Eqn.A.4:

$w(X, 0) = 0$

$w(X, t) = 0$ for $X \geq L(t)$

$q(0, t) = q_0$ for a one-sided fracture

Or

$q(0, t) = 0.5q_0$ for a two-sided fracture.

Finally, the shape of the fracture takes the form shown in Eqn.A.5.

$$w(X,t) = w(X,0)\left(1-\frac{X}{L}\right)^{0.25} \quad \text{..... (A.5)}$$

And the fracture volume is given by Eqn.A.6.

$$V = \frac{\pi}{5} L h_f w(0,t)\left(1-\frac{X}{L}\right) = q_0 t \quad \text{..... (A.6)}$$

For KGD model, the fluid pressure gradient in the propagation direction is determined by Eqn. A.7.

$$p(0,t) - p(x,t) = p_f - p = \frac{12\mu q_0}{h_f}\int_0^x \frac{1}{w^3(x,t)}\,dx \quad \text{..... (A.7)}$$

The equilibrium condition directed by applied mechanics is given by Eq. 4.59.

$$\int_0^L \frac{p(X,t)}{\sqrt{L^2 - x^2}}\,dx = \frac{\pi}{2}\sigma_h + \frac{K}{\sqrt{2L}} \quad \text{..... (A.8)}$$

where σ_h is the in-situ rock stress, perpendicular to the fracture face. K is the cohesion modulus.

Zheltov and Khristianovitch (1955) simplified the upper equations, which can be used to calculate the pressure distribution approximately.

$$p_f = p_0 \quad \text{..... (A.9)}$$

for $0 < \lambda < L_0/L$, and

$$p_f = 0 \quad \text{..... (A.10)}$$

for $L_0/L < \lambda < 1$, where p is the fluid pressure. The $\lambda = X/L$ is the dimensionless fracture coordinate.

Then the condition of "wetted" fracture length can be calculated from Eq. 4.62. This provides a good point to start the calculation, and this approximation is good enough to prevent further refinements.

$$\lambda_0 = \frac{L_0}{L} = \sin\frac{\pi}{2}\left(\frac{\sigma_h}{p_f}\frac{K_c}{p_f\sqrt{L}}\right) \quad \text{..... (A.11)}$$

The shape of the fracture in the horizontal plane is elliptical, with maximum width at the wellbore that can be calculated using Eqn.A.12.

$$w(0,t) = \frac{2(1-\nu)L\left(p_f - \sigma_h\right)}{G} \quad \text{..... (A.12)}$$

A good approximation to determine the fluid flow resistance in the fracture is Eqn. A.13.

$$\int_0^{\lambda_0} \frac{w^3(0,t)}{w^3(X,t)} d\lambda \approx \frac{7}{4}\left(1-\lambda_0^2\right)^{-\frac{1}{2}} \quad \text{..... (A.13)}$$

The fracture volume of one-sided fracture amounts can be calculated approximately by Eqn. A.13.

$$V = h_f L w(0,t)\int_0^1 \left(1-\lambda^2\right)^{\frac{1}{2}} d\lambda = \frac{\pi}{4} h_f L w(0,t) = q_0 t \quad \text{..... (A.14)}$$

After substituting Eqn. A.13 into Eqn. A.7 and linking with Eqn. A.14, we can finally obtain Eqns. A.15 and A.16

$$L(t) = 0.68\left[\frac{G q_0^3}{\mu(1+\nu)h_f^3}\right]^{\frac{1}{6}} t^{\frac{1}{3}} \quad \text{..... (A.15)}$$

$$w(0,t) = 1.87\left[\frac{(1+\nu)\mu q_0^3}{G h_f^3}\right] \mathrm{t}^{\frac{1}{3}} \quad \text{..... (A.16)}$$

APPENDIX B

POROELASTIC PKN MODEL

B.1 Mechanics of Poroelastic PKN Model

As discussed in Section 2, the poroelasticity in hydraulic fracture is induced by the leak-off of the fracturing fluid. The following will give the coupling mechanisms of poroelasticity.

1) Balance of Fluid Momentum:

$$\frac{\partial \Delta p}{\partial x} = -\frac{64}{\pi}\frac{q\mu}{w_m{}^3} = -\frac{\pi^2 q\mu}{w_{ave}{}^3} \quad \text{..... (B.1)}$$

where:

Δp: net pressure in the fracture

q: average flow rate per unit height of fracture, which is Q_0/h_f

Q_0: Injection Rate

w_m: max width of the fracture in the cross section

w_{ave}: average width of the fracture

H_f: fracture height

μ: fluid viscosity

Note: the meaning of symbols in this thesis from now on will be shown in the nomenclature later unless otherwise specified.

For a non-Newtonian fluid, the momentum equation for laminar flow of a power law fluid in a fracture is approximated by the one-dimensional equation from lubrication theory:

$$\frac{\partial p_f}{\partial x} = -\frac{2Kq\left|q\right|^{n-1}}{\psi^n w^{2n+1}} \quad \text{(B.2)}$$

where:

$$\psi = \frac{n}{2(2n+1)} \frac{\Gamma\left(\frac{4n+1}{2n}\right)}{\Gamma\left(\frac{5n+1}{2n}\right)} \left(\frac{2}{\sqrt{\pi}}\right)^{\frac{3n+2}{n}} \quad \text{(B.3)}$$

2) Local Fluid Mass Balance: (Continuity Equation)

$$\frac{\partial q}{\partial x} + \frac{\partial w_{ave}}{\partial t} + u = 0 \quad \text{(B.4)}$$

For steady and incompressible flow, the volume flow rate into a control volume must be equal to the volume flow rate out of the control volume, plus the volume leak-off rate.

u: fluid leak-off velocity accounting for both walls

3) Leak-Off Equation:

$$u = \frac{2C_l}{\sqrt{t - \tau(x)}} \quad \text{(B.5)}$$

C_l: leak-off coefficient

t: the lapse time since pumping starts

τ(x): the arrival time of fracture tip at location x.

4) Pressure-Width Relation: (without Poroelasticity)

$$w_{ave} = \frac{\pi(1-\nu)h_f \Delta p}{4G} = \frac{\pi}{4} w_m \quad \text{..... (B.6)}$$

If poroelasticity is considered: The average fracture width w_{ave} is composed of two contributions, w^e and w^p which reflect the existence of two different processes (Cheng, 1990; Boone, 1990)

$$w_{ave} = w^e + w^p \quad \text{..... (B.7)}$$

in which the first component w^e is controlled by the net stress $p=p_f-\sigma_0$, while w^p depends on the net pressure $\Delta p=p_f-p_0$. The poroelastic processes that are taking place in the permeability layer cause both w^e and w^p to be time-dependent. However, the time-dependednt contribution of w^e is typically overshadowed by that associated with w^p (Cheng, 1990). Hence it is approximated the net stress effect as being purely elastic

$$w^e = M_c(p_f - \sigma_0) \quad \text{..... (B.8)}$$

If the fluid pressure maintained constant, the time dependent width reduction w^p can be described as (Boone and Detournay, 1990)

$$w^p = -2\eta \Delta p M_c f(t^*) \quad \text{..... (B.9)}$$

where $f(t^*)$ is the evolution function which varies 0 and 1 approaches 0 and infinity, respectively. The symbol t^* denotes a dimensional fracture surface exposure time defined as

$$t^* = \frac{4c\left[t - \tau(x)\right]}{{h_f}^2} \quad \text{.....(B.10)}$$

c is the diffusivity coefficient.

$$c = \frac{\kappa}{\phi C_p} \quad \text{.....(B.11)}$$

Similarly, $f(t^*)$ is given by

$$f(t^*) = \frac{4}{\pi}\int_0^\infty erfc\left(\frac{y}{2\sqrt{t^*}}\right) g(y)dy \quad \text{.....(B.12)}$$

Where:

$$g(y) = 1 - \sqrt{\frac{y}{2}}\sqrt{\sqrt{4+y^2} - y} \quad \text{.....(B.13)}$$

The poroelastic contribution to the width change equation is derived on the assumption that the fracture surface is directly exposed to a fracturing fluid of same viscosity and compressibility as the reservoir fluid, and that the pore pressure difference Δp between the fracture face and the far-field is a constant in time. The leak-off velocity constituent with this set of assumption is given by (accounting for both walls)

$$u = \frac{2\kappa\Delta p}{\sqrt{\pi c\left(t - \tau(x)\right)}} \quad \text{.....(B.14)}$$

The actual leak-off process, however, is described by equation (B.5) with the leak-off coefficient C_l, a constant that takes into account difference in properties between the fracturing and the reservoir fluid and the buildup of a filter cake on the fracture wall. Assuming incompressibility of the fracturing fluid and ignoring the movement of the fracturing/reservoir fluid interface, the leak-off equation (B.5) can equivalently be written

in terms of the difference λ_p between the pressure at the fracturing/reservoir fluid interface and the far-field pore pressure.

$$u = \frac{2\kappa\lambda_p}{\sqrt{\pi c\left(t-\tau(x)\right)}} \quad \text{..... (B.15)}$$

where: $\sqrt{}$

$$\lambda_p = \frac{C_l\sqrt{\pi c}}{\kappa} \quad \text{..... (B.16)}$$

Using equation (B.14) and (B.15), the expression for the width change in equation (B.9) becomes

$$w^p = -2\eta\lambda_p M_c f(t^*) \quad \text{..... (B.17)}$$

Substituting equation (B.17) and (B.8) into (B.7) we get,

$$w = M_c\left(p_f - \sigma_0 - \sigma_B\right) \quad \text{..... (B.18)}$$

where:

$$\sigma_B = 2\eta\lambda_p f(t^*) \quad \text{..... (B.19)}$$

5) GLOBAL MASS BALANCE EQUATION

The fracture length, L is a function of time and not known a priori. The volume of the fracture is equal to the volume of fluid pumped minus the cumulative leak-off volume.

$$\int_0^{L(t)} w(x,t)dx + \int_0^{L}\int_0^{L(t')} u(x,t')dxdt' = \int_0^{t} q_o(t')dt' \quad \text{..... (B.20)}$$

where range $0 \le x \le L$

$q_o = Q_o / h_f$ is the fluid injection rate per unit height of the fracture.

6) Initial and Boundary Condition

The system of equations are supplemented by the boundary conditions

$$\begin{aligned} q(0,t) &= q_o(t); t > 0 \\ p(L(t),t) &= 0, t > 0 \end{aligned} \quad \text{..... (B.21)}$$

and the initial conditions

$$L(0) = 0 \text{ and } p(0,0) = 0 \quad \text{..... (B.22)}$$

The mathematical model is required to predict the evolution of the fracture length *L(t)*, and fracturing pressure $p_f(0,t) = p_f(0,t) + \sigma_o$,as well as the field variables $q(x,t), w(x,t), p(x,t)$ an $du(x,t)$.

B.2 Methodology

Finite difference method is used to solve the propagation and recession in this poroealstic PKN hydraulic model (Detournay *et al.*, 1990).

First, divide the fracture into n segments, that's totally n+1 node along the fracture, take *x1*=0 and W_{n+1}=0. On each node, a finite difference expression for the continuity equation can be obtained. For nodes from 2 to n, central difference expression is applied, while for the first node, forward difference expression is used. (No difference expression needed for the last node because W_{n+1}=0).

With respect to time from t^k to t^{k+1}, use of integration formula gives a linear tridiagonal system for $W_{i-1}{}^k$, W_i^k and $W_{i+1}{}^k$. Since $W_{i-1}{}^k$, W_i^k and $W_{i+1}{}^k$ are known, by

solving the tridiagonal system, we can obtain width increment ΔW_i^k of each node at time t^{k+1}, using standard numerical method. Thus the current width, length and volume of the fracture can be calculated accordingly.

The tridiagonal system is given:

$$\begin{aligned}&\left[\frac{\pi H}{4con}-\frac{\Delta t_k(2pn+2)(w_i^k)^{2pn+1}}{(\Delta x)^2}\right]\Delta w_i^k+\\&\left[\frac{\Delta t_k(pn+1)(w_{i-1}^k)^{2pn+1}}{(\Delta x)^2}\right]\Delta w_{i-1}^k+\left[\frac{\Delta t_k(pn+1)(w_{i+1}^k)^{2pn+1}}{(\Delta x)^2}\right]\Delta w_{i+1}^k \quad \text{..... (B.23)}\\&=\left[-\frac{\Delta t_k}{(\Delta x)^2}\right][(w_{i+1}^k)^{2pn+2}-2\ w_i^k)^{2pn+2}+(w_{i-1}^k)^{2pn+2}]\\&-\frac{4HCl}{con}\left(\sqrt{t_{k+1}-\tau_i}-\sqrt{t_k-\tau_i}\right)\end{aligned}$$

in which, the index i is from 2 to n.

$$con=-\frac{G\phi^{pn}\pi^{2pn+1}\mathrm{H}^{pn-1}}{2(2pn+2)K(1-\nu)4^{2pn+1}} \quad \text{..... (B.24)}$$

Here we use p_n in stead of the power law index n.

For node n=1,

$$\begin{aligned}&\left[-(2pn+2)(w_i^k)^{2pn+1}\right]\Delta w_i^k+[0]\Delta w_{i-1}^k+\left[(2pn+2)(w_{i+1}^k)^{2pn+1}\right]\Delta w_{i+1}^k \quad \text{.... (B.25)}\\&=\frac{\Delta xQ}{con}[(w_i^k)^{2pn+2}-(w_{i+1}^k)^{2pn+2}]\end{aligned}$$

Thus, for node 1 to node n along the fracture at time t^{k+1}, we obtain:

$$[b_i]\Delta w_i^k+[a_i]\Delta w_{i-1}^k+[c_i]\Delta w_{i+1}^k=[d_i] \quad \text{..... (B.26)}$$

In which, a_i, b_i, c_i and d_i can be expressed from equation (B.23-B.25).

B.3 Programming

A FORTRAN program is used to simulate the propagation of a hydraulic fracture with the effects from poroelasticity.

The flow chart of this program is shown in the following Fig.B.1.

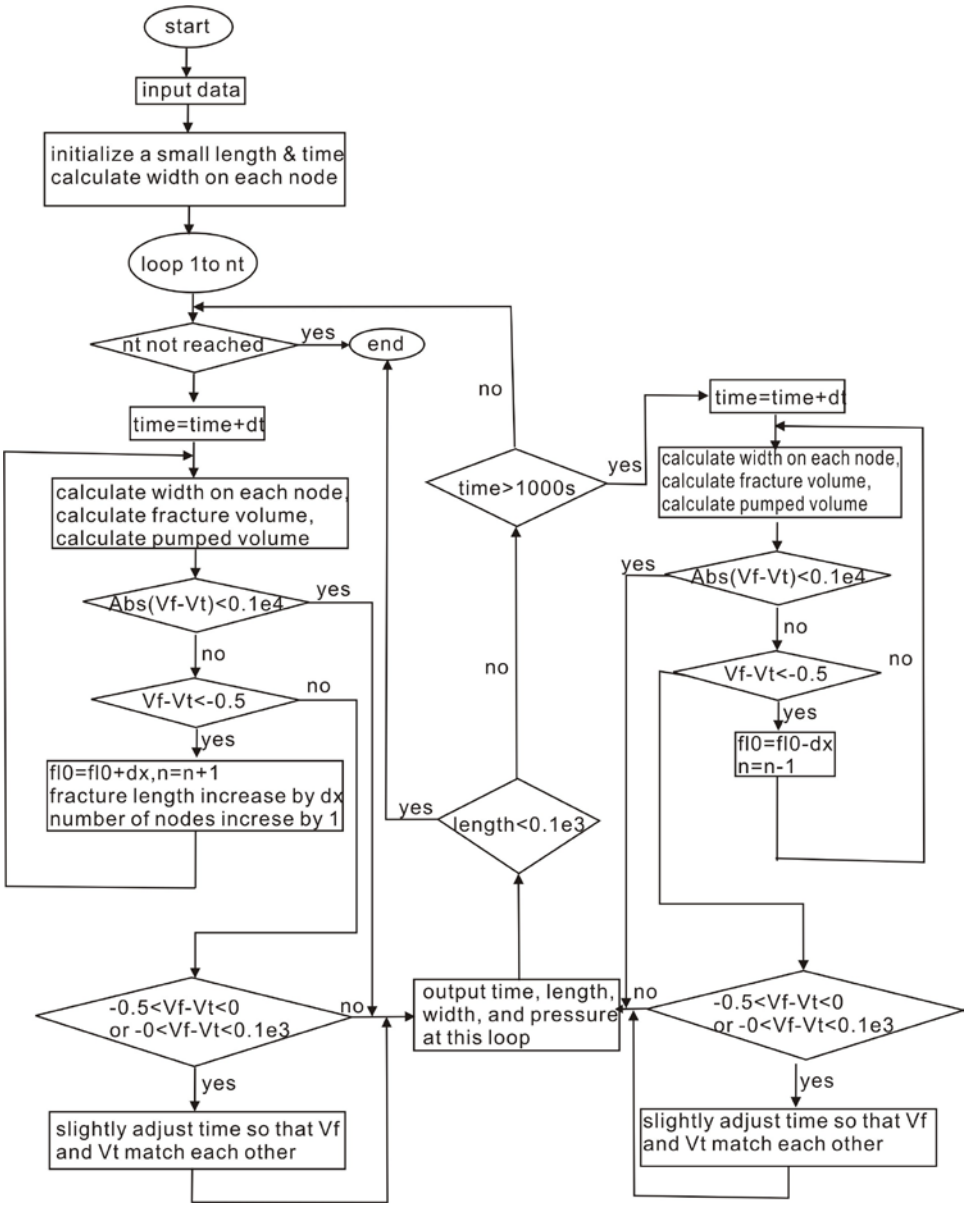

Fig.B.1 Flow Chart of Poroleastic PKN Model

B.4 Parameters Sensitivity Analysis

In order to investigate the effects of different values of parameters on the fracture propagation, the sensitivity of shear modulus and Power law constitutive constant *K*. The results are shown in the following figures.

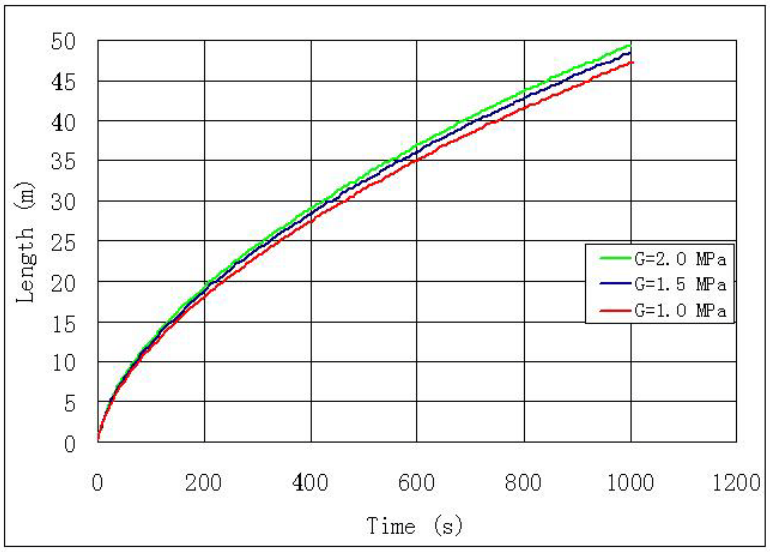

Fig.B.2 Sensitivity Analysis of G on Fracture Length

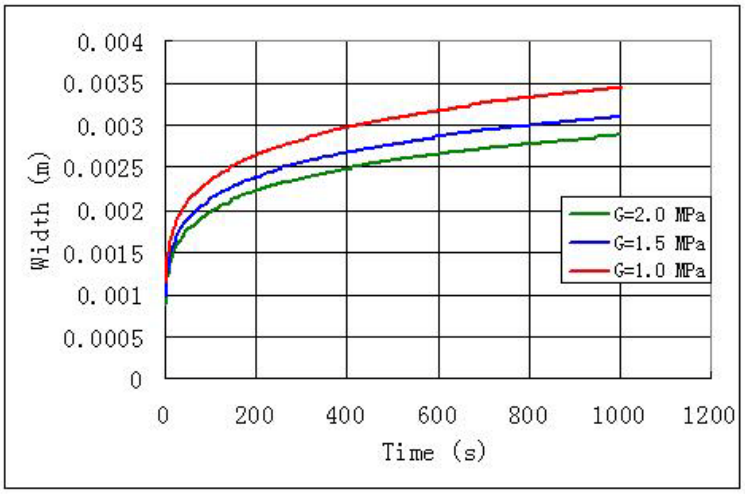

Fig.B.3 Sensitivity Analysis of G on Fracture Width

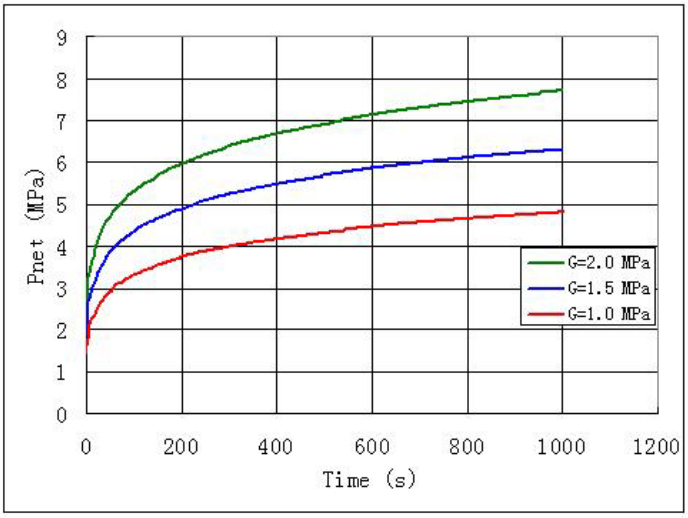

Fig.B.4 Sensitivity Analysis of G on Fracture Pressure

From the figures, we can see that the shear modulus has great effects on the fracture propagation, especially on fracture width and pressure, and have fewer effects on fracture length. The power law constitutive constant *K* has smaller effects on the fracture propagation, and almost no effects on fracture length.

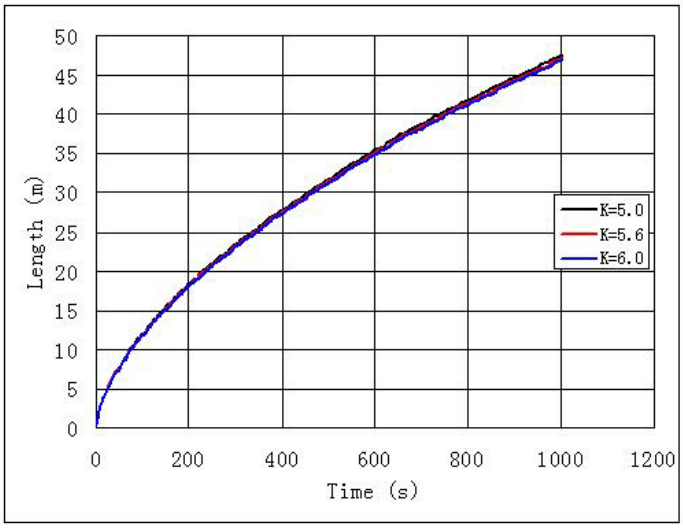

Fig.B.5 Sensitivity Analysis of K on Fracture Length

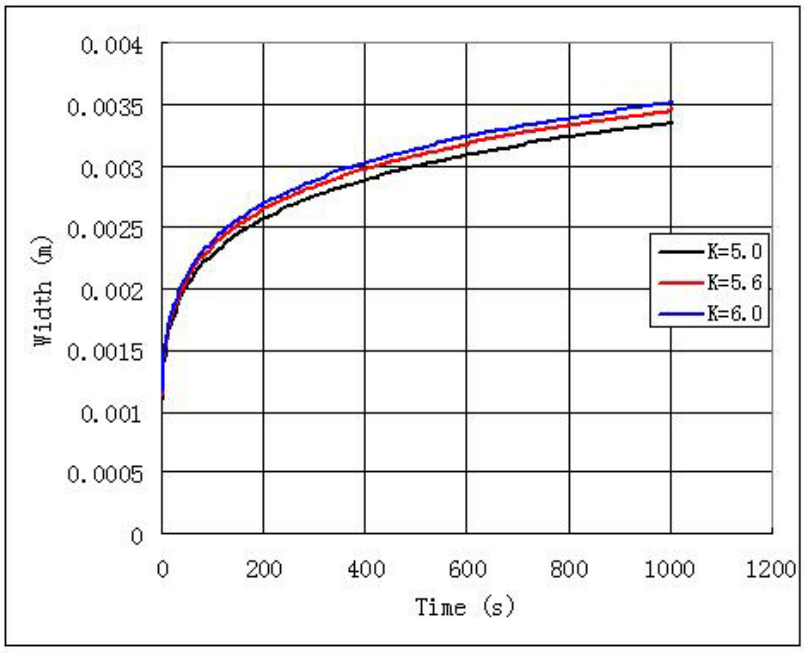

Fig.B.6 Sensitivity Analysis of K on Fracture Width

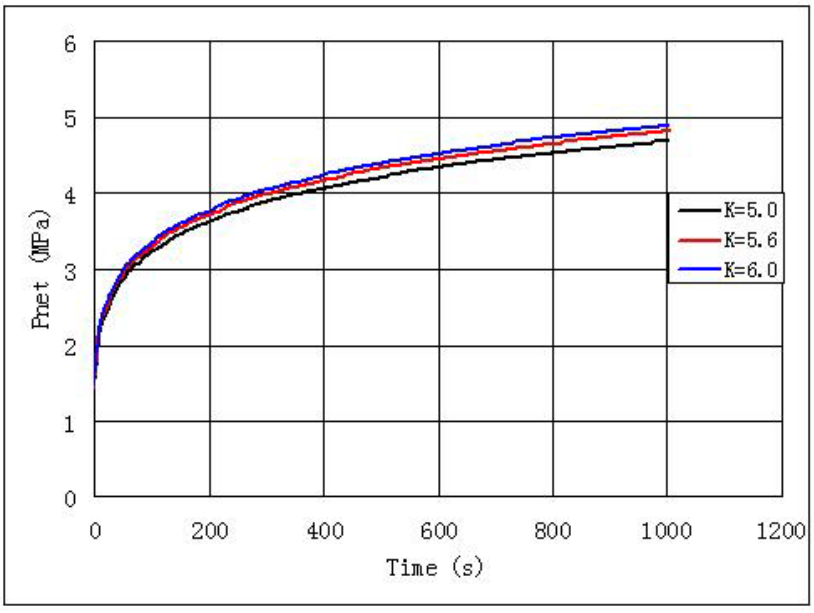

Fig.B.7 Sensitivity Analysis of K on Fracture Pressure

APPENDIX C

INDUCED STRESSES BY FRACTURE COMPRESSION

Stress field distributions around fracture are important in the conventional hydraulic fracturing; fracturing during water-flooding of petroleum reservoirs. As we know, the stresses around a fracture can be estimated from by adding four different parts: in situ original stresses, poroelastic induced stresses; thermoelastic induced stresses and induced stresses from fracture compression. In our former work, we have discussed the poroelastic induced stresses and the thermoelastic induced stresses, and also include the induced stresses by fracture compression in a comprehensive FORTRAN program. In order to examine the importance of induced stresses by fracture compression, a separate work has been done here. In this study, we reviewed several methods for the fracture compression induced stresses, and compared them with some other work. A FORTRAN program is used to get the contour plots for the distributions around fracture.

Since the fracture length is far greater than its width, we consider the fracture as a line crack. A concise review of elastic theory with applications to geology is found in the text by Jaeger and Cook (1979). The mathematical methods for crack theory are given in the book by Sneddon and Lowengrub (1969). Jaeger and Cook (1979) gave the methods for calculating the stresses changes around a flat elliptic crack. Pollard and Segall (1987) also gave out the expressions for the calculations of stresses field around crack. Also, another method for this problem is given by Norman R. Warpinski, and Paul T. Branagan in 1989.

In this study, the improved expressions on the basis of Jaeger and Cook (1979) for the calculation of the stress changes around an elliptic fracture due to the fracture are

given. The results from different methods can be compared with the work of D.Maugis (1992). In this report, the method from Pollard and Segall is selected in our program to calculate the effects of fracture pressurization. And the plots for special cases are given in this report.

1) Expressions from Jaeger and Cook

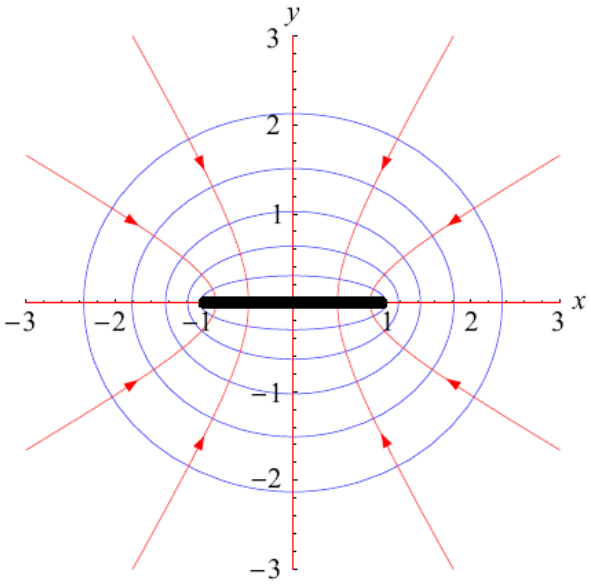

Fig.C.1 Elliptical Coordinate System

As shown in figure.C.1, considering the flat elliptic crack $\xi_0 = 0$, from J&C, for uniaxial stress P_2 at infinity inclined at β to the plane of the crack:

$$\sigma_\xi + \sigma_\eta = P_2 \cos 2\beta + \alpha P_2[(1-\cos 2\beta)\sinh 2\xi - \sin 2\beta \sin 2\eta] \ldots\ldots \quad (C.1)$$

$$\sigma_\xi - \sigma_\eta = \alpha P_2 \cos 2(\eta-\beta)\cosh 2\xi + \alpha^2 P_2\{(1-\cos 2\beta)\sinh 2\xi(\cos 2\eta - 1) \\ -\cos 2\beta\cosh 2\xi + \cos 2(\eta-\beta) - \cosh 2\xi \sin 2\beta \sin 2\eta\} \quad \text{(C.2)}$$

$$\tau_{\xi\eta} = P_2 \frac{\alpha}{2}\sin 2(\beta-\eta)\sinh 2\xi \\ +0.5\alpha^2 P_2\{\sinh 2\xi \sin 2\beta(\cos 2\eta - 1) \quad \text{..... (C.3)} \\ +\sin 2\eta(1-\cos 2\beta)(\cosh 2\xi - 1)\}$$

in which

$$\alpha = (\cosh 2\xi - \cos 2\eta)^{-1} \quad \text{..... (C.4)}$$

In order to check the equations we used in program, I firstly simplified the stresses on the axes Ox and Oy for the case $\beta = \frac{\pi}{2}$, and compared them with the plots in J&C: And the following plots shown are:

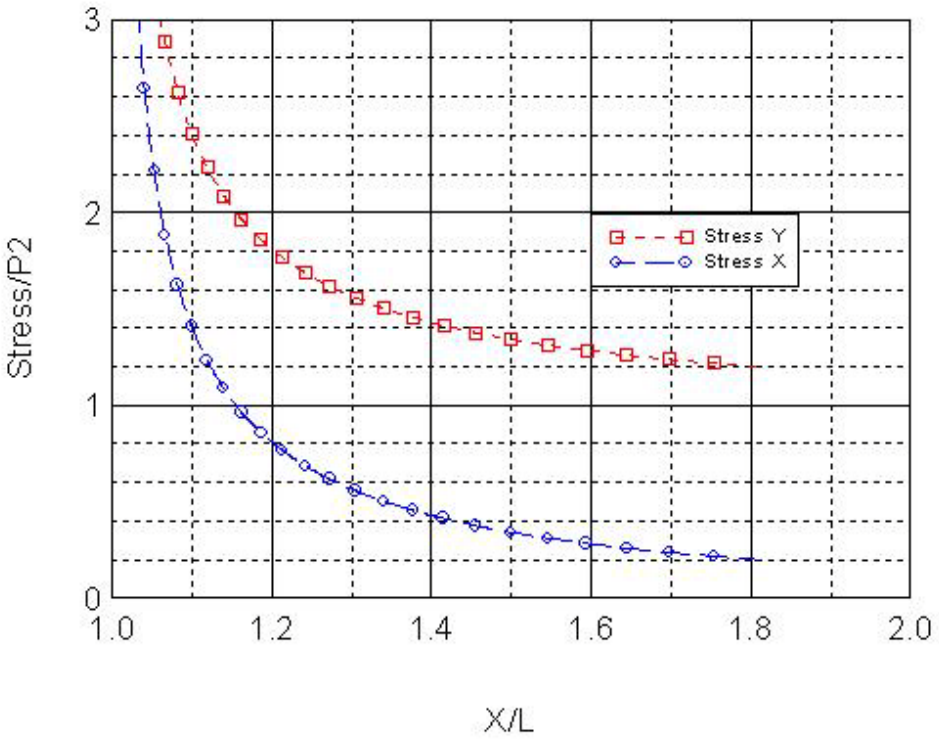

Fig.C.2 Stresses on the X-Axis

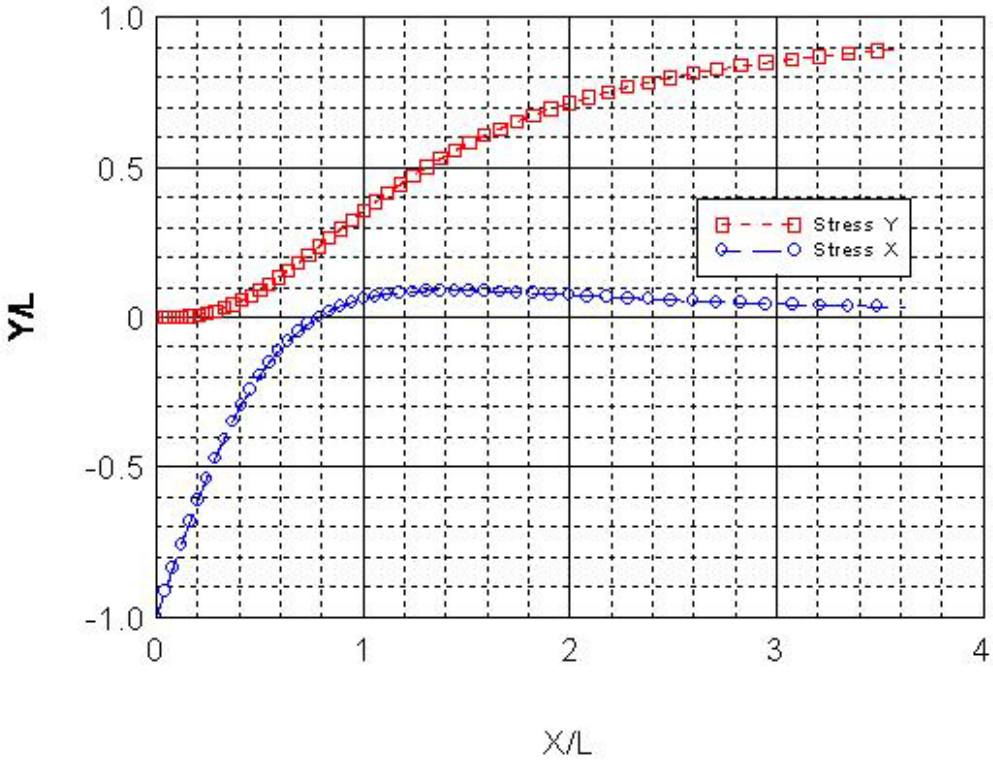

Fig.C.3 Stresses on the Y-Axis

In the plots are shown the stresses σ_x and σ_y respectively, how could we get these two values from σ_ξ and σ_η? We should use scale factors for the transform from different coordinate systems. A transform factor we used in calculating the induced stress by poro-thermo-elasticity for this is: $g = \sqrt{\frac{L^2}{2}(\cosh 2\xi - \cos 2\eta)}$

and: $\sigma_x = g^2 * \sigma_\xi$; $\sigma_y = g^2 \sigma_\eta$; $\sigma_{xy} = g^2 * \sigma_{\xi\eta}$;

However, in this problem, this factor is not right.

In fact, for the special directions: $\eta = 0$ and $\eta = \frac{\pi}{2}$; we get: $\sigma_{\xi\eta} = 0$

So, stresses on the a-axis are: $\sigma_x = \sigma_\xi$ and $\sigma_y = \sigma_\eta$

And, stresses on the a-axis are: $\sigma_x = \sigma_\eta$ and $\sigma_y = \sigma_\xi$

And this conclusion is right through comparing with the plots compared with what J&C got in their book (Fig.10.11.2, P268, 1979).

Then, the transformation factors in this problem are deduced in the following:

From J&C, we got the following equations:

$$\sigma_{\eta\eta} - \sigma_{\xi\xi} + 2i\sigma_{\xi\eta} = (\sigma_{yy} - \sigma_{xx} + 2i\sigma_{xy})e^{2i\theta} \quad \text{..... (C.5)}$$

$$\sigma_{\xi\xi} + \sigma_{\eta\eta} = \sigma_{yy} + \sigma_{xx} \quad \text{..... (C.6)}$$

where:

$$e^{2i\theta} = \cos 2\theta + i \sin 2\theta \quad \text{..... (C.7)}$$

$$\tan\theta = \frac{y}{x} = \frac{c \sinh\xi \sin\eta}{c \cosh\xi \cos\eta} \quad \text{..... (C.8)}$$

Subtract equation C.5 from C.6:

$$2(\sigma_{\xi\xi} - i\sigma_{\xi\eta}) = \sigma_{yy} + \sigma_{xx} - (\sigma_{yy} - \sigma_{xx} + 2i\sigma_{xy})e^{2i\theta} \quad \text{..... (C.9)}$$

So:

$$\begin{aligned} 2\sigma_{\xi\xi} - 2i\sigma_{\xi\eta} &= \sigma_{yy} + \sigma_{xx} - \sigma_{yy}\cos 2\theta + \sigma_{xx}\cos 2\theta \\ &-(2i\sigma_{xy})(\cos 2\theta + i\sin 2\theta) \\ &-(\sigma_{yy} - \sigma_{xx})(i\sin 2\theta) \end{aligned} \quad \text{..... (C.10)}$$

$$\begin{aligned} 2\sigma_{\xi\xi} - 2i\sigma_{\xi\eta} &= \sigma_{yy} + \sigma_{xx} - \sigma_{yy}\cos 2\theta + \sigma_{xx}\cos 2\theta \\ &+2\sigma_{xy}\sin 2\theta - 2i\sigma_{xy}\cos 2\theta - (\sigma_{yy} - \sigma_{xx})(i\sin 2\theta) \end{aligned} \quad \text{..... (C.11)}$$

Therefore:

$$2\sigma_{\xi\xi} = (\sigma_{yy} + \sigma_{xx}) - (\sigma_{yy} - \sigma_{xx})\cos 2\theta + 2\sigma_{xy}\sin 2\theta \quad \text{..... (C.12)}$$

$$-2i\sigma_{\eta\xi} = -(\sigma_{yy} - \sigma_{xx})i\sin 2\theta - 2i\sigma_{xy}\cos 2\theta$$

$$or: \quad \sigma_{\eta\xi} = \frac{1}{2}(\sigma_{yy} - \sigma_{xx})\sin 2\theta + \sigma_{xy}\cos 2\theta \quad \text{..... (C.13)}$$

We can also add C.5 to C.6, and get:

$$2\sigma_{\eta\eta} = (\sigma_{yy} + \sigma_{xx}) + (\sigma_{yy} - \sigma_{xx})\cos 2\theta - 2\sigma_{xy}\sin 2\theta \quad \text{..... (C.14)}$$

$$\sigma_{\eta\xi} = \frac{1}{2}(\sigma_{yy} - \sigma_{xx})\sin 2\theta + \sigma_{xy}\cos 2\theta \quad \text{..... (C.15)}$$

Then, equation C.14 times $\cos 2\theta$ and plus equation C.15 times $2\sin 2\theta$:

$$\sigma_{yy} - \sigma_{xx} = 2\sigma_{\eta\eta}\cos 2\theta + 2\sigma_{\xi\eta}\sin 2\theta - (\sigma_{\xi\xi} + \sigma_{\eta\eta})\cos 2\theta \quad \text{..... (C.16)}$$

The same process, we can get:

$$\begin{aligned}\sigma_{yy} &= \sigma_{\eta\eta}\cos 2\theta + \sigma_{\xi\eta}\sin 2\theta + (\sigma_{\xi\xi} + \sigma_{\eta\eta})\sin^2\theta \\ &= \sigma_{\eta\eta} + \sigma_{\xi\eta}\sin 2\theta + (\sigma_{\xi\xi} - \sigma_{\eta\eta})\sin^2\theta\end{aligned} \quad \text{..... (C.17)}$$

$$\sigma_{xx} = \sigma_{\xi\xi} - \sigma_{\xi\eta}\sin 2\theta - (\sigma_{\xi\xi} - \sigma_{\eta\eta})\sin^2\theta \quad \text{..... (C.18)}$$

$$\sigma_{xy} = (\sigma_{\xi\eta} - \frac{1}{2}(\sigma_{yy} - \sigma_{xx})\sin 2\theta)/\cos 2\theta \quad \text{..... (C.19)}$$

We can put equations C.17 and C.18 into C.19 to get the expression for σ_{xy}.

Then, we can get the total principal stresses around the crack by stresses transformation:

$$\sigma_1 = \frac{1}{2}(\sigma_x + \sigma_y) + [\frac{1}{4}(\sigma_x - \sigma_y)^2 + \sigma_{xy}{}^2]^{1/2} \quad \text{..... (C.20)}$$

$$\sigma_2 = \frac{1}{2}(\sigma_x + \sigma_y) - [\frac{1}{4}(\sigma_x - \sigma_y)^2 + \sigma_{xy}{}^2]^{1/2} \quad \text{..... (C.21)}$$

And the maximum shear stresses distribution around a fracture can be given by:

$$\tau = \frac{1}{2}(\sigma_1 - \sigma_2) \quad \text{..... (C.22)}$$

Mean normal stress is given:

$$\sigma = \frac{1}{2}(\sigma_1 + \sigma_2) \quad \text{..... (C.23)}$$

These equations are checked in program and plots are given for comparison. Here the maximum shear stress and mean normal stress for the case of uni-axial normal stress p are given in the following:

Sign convention for the stresses: compressive as positive, and tensional as negative, and pore pressure as positive.

The uni-axial tension stress (-1 MPa) at infinity perpendicular to the crack, using these equations I plot the distributions of maximum shear stress, mean normal stress:

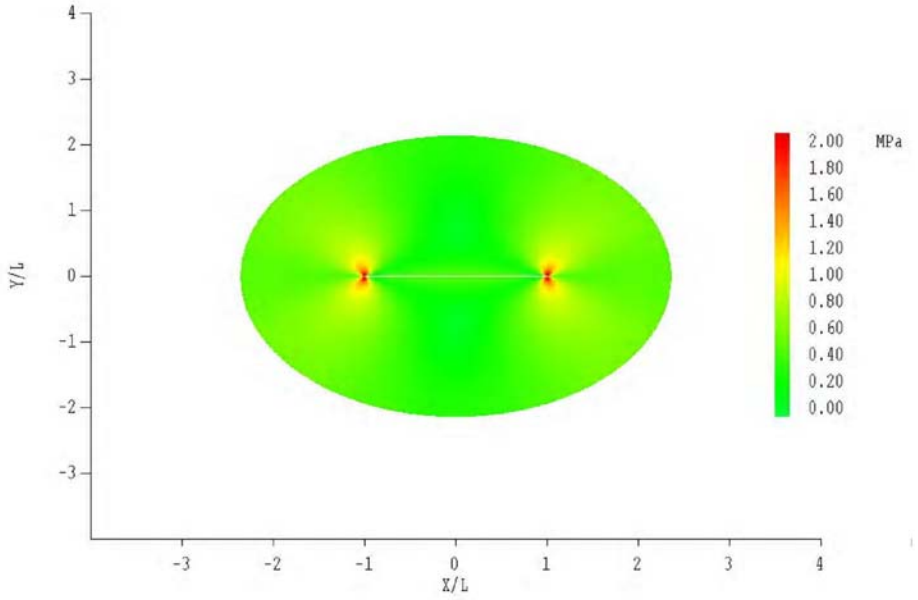

Fig.C.4 Maximum Shear Stress

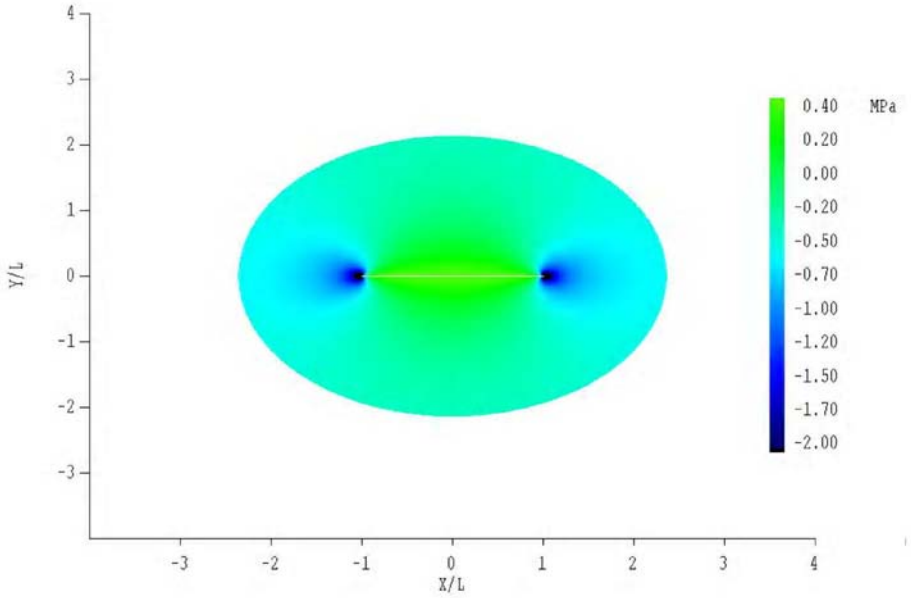

Fig.C.5 Mean Normal Stress

In fact, after setting the same color scales, the figures we got from this program are totally the same with what we got from the other methods such as the following method.

2) Method from Pollard and Segall

Pollard and Segall (1987) have reported the general expressions for the stress field about the crack.

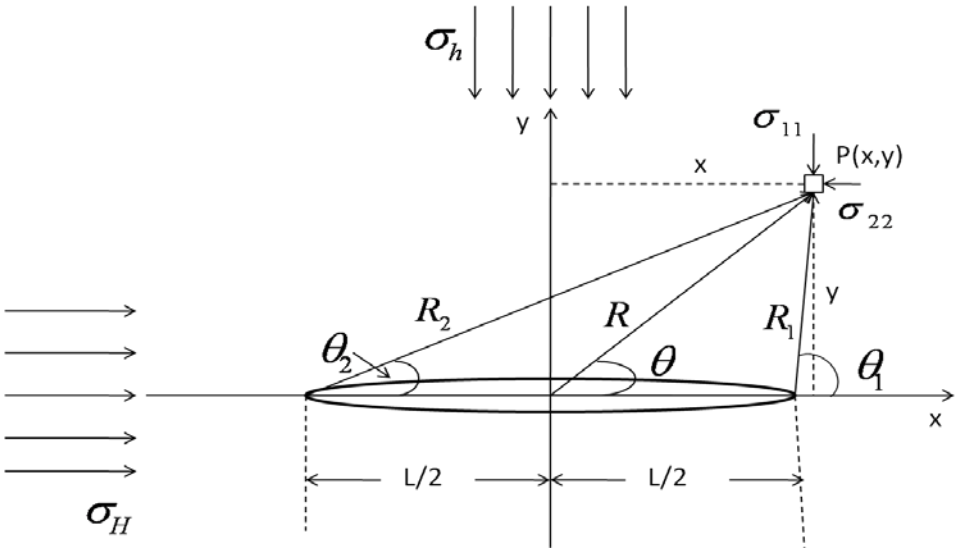

Fig.C.6 Stresses Changes due to Fracture Compression

In order to compare with the expressions in Warpinski, I used the same 2-D crack with the expressions from Pollard and Segall (1987), and transformed them into x-y coordinates system:

$$\sigma_{xx} = \sigma_{22} + \Delta\sigma_I [Rr^{-1} * \cos(\theta - \Theta) - 1 - (L/2)^2 Rr^{-3} \sin\theta \sin 3\Theta] \\ + \Delta\sigma_{II} [2Rr^{-1} * \sin(\theta - \Theta) - (L/2)^2 Rr^{-3} \sin\theta \cos 3\Theta] \quad \text{(C.24)}$$

$$\sigma_{yy} = \sigma_{11} + \Delta\sigma_I[Rr^{-1} * \cos(\theta - \Theta) - 1 + (L/2)^2 Rr^{-3} \sin\theta \sin 3\Theta] + \Delta\sigma_{II}[(L/2)^2 Rr^{-3} \sin\theta \cos 3\Theta] \quad \text{(C.25)}$$

$$\sigma_{xy} = \sigma_{12} + \Delta\sigma_{II}[Rr^{-1} * \cos(\theta - \Theta) - 1 - (L/2)^2 Rr^{-3} \sin\theta \sin 3\Theta] + \Delta\sigma_I[(L/2)^2 Rr^{-3} \sin\theta \cos 3\Theta] \quad \text{(C.26)}$$

in which σ_{11} is the remote stress normal to the crack, σ_{22} is the remote parallel stress, and σ_{12} is the remote shear stress. $[\Delta\sigma_I, \Delta\sigma_{II}]=[(\sigma_{11} - \sigma_{11}^{c}),(\sigma_{12} - \sigma_{12}^{c})]$ in which σ_{11}^{c} refers to the normal stress on the crack internal surface, and σ_{12}^{c} refers to the shear stress on the crack internal. L is the crack length, and the geometric relations are given by the following equations: (as shown in the upper figure)

$$R = \sqrt{x^2 + y^2}\ , \theta = \tan^{-1}(y/x) \quad \text{(C.27)}$$

$$R_1 = \sqrt{y^2 + (\frac{L}{2} - x)^2}\ ,\ \theta_1 = \tan^{-1}[y/(x - L/2)] \quad \text{(C.28)}$$

$$R_2 = \sqrt{y^2 + (x + L/2)^2}\ ,\ \theta_2 = \tan^{-1}[y/(x + L/2)] \quad \text{(C.29)}$$

$$r = (R_1 R_2)^{1/2} \text{ and } \Theta = (\theta_1 + \theta_2)/2 \quad \text{(C.30)}$$

Negative values of θ, θ_1, and θ_2 should be replaced by $\pi+\theta$, $\pi+\theta_1$, and $\pi+\theta_2$ respectively, because these angles are in $(0, \pi)$.

We should note that the stresses in equations C.24-C.26 are the total stress field around the crack i.e., they include the in-situ stresses.

A special case is researched in this study; we use unit tension to test the results. Given conditions for the upper equations:

$$\sigma_{11} = -1 \quad MPa \quad \text{.....} \quad \text{(C.31)}$$

$$\sigma_{22} = \sigma_{12} = \sigma_{12}^{c} = \sigma_{11}^{c} = 0 \quad MPa \quad \text{.....} \quad \text{(C.32)}$$

That means the condition only has unit normal remote stress on the crack without other stresses and internal pressure.

The results of stresses distribution around the crack are given in the following figures. Note that if the input data are changed, the program needs modified in order to get right color scales.

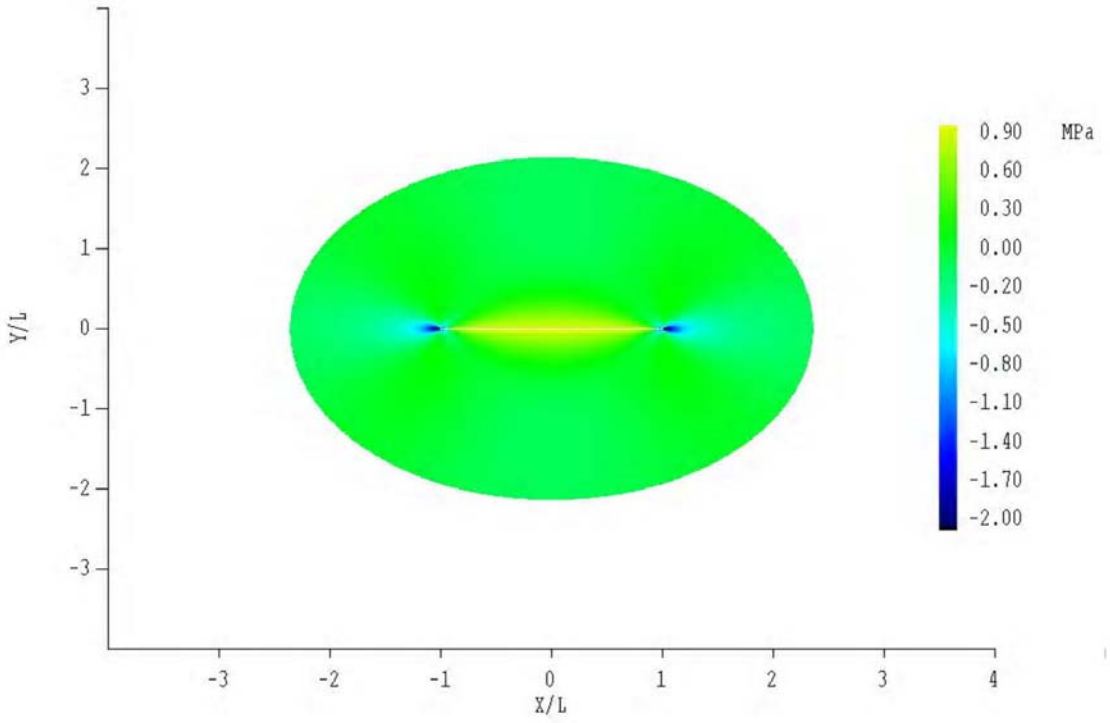

Fig.C.7 Induced Stress around Crack ($\Delta\sigma_{xx}$)

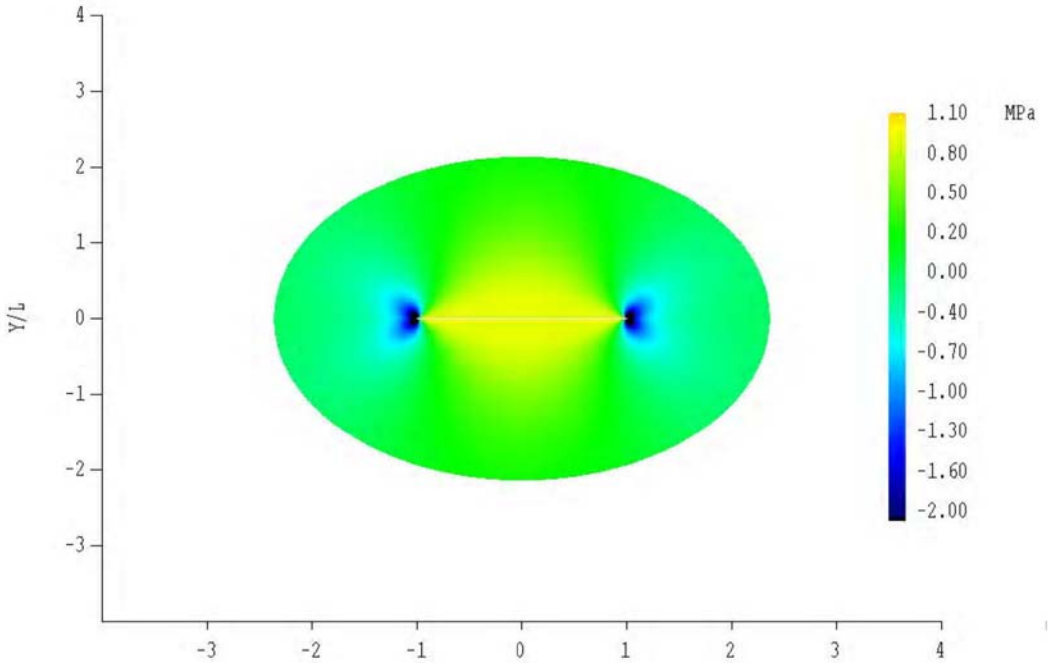

Fig.C.8 Induced Stress around Crack ($\Delta\sigma_{yy}$)

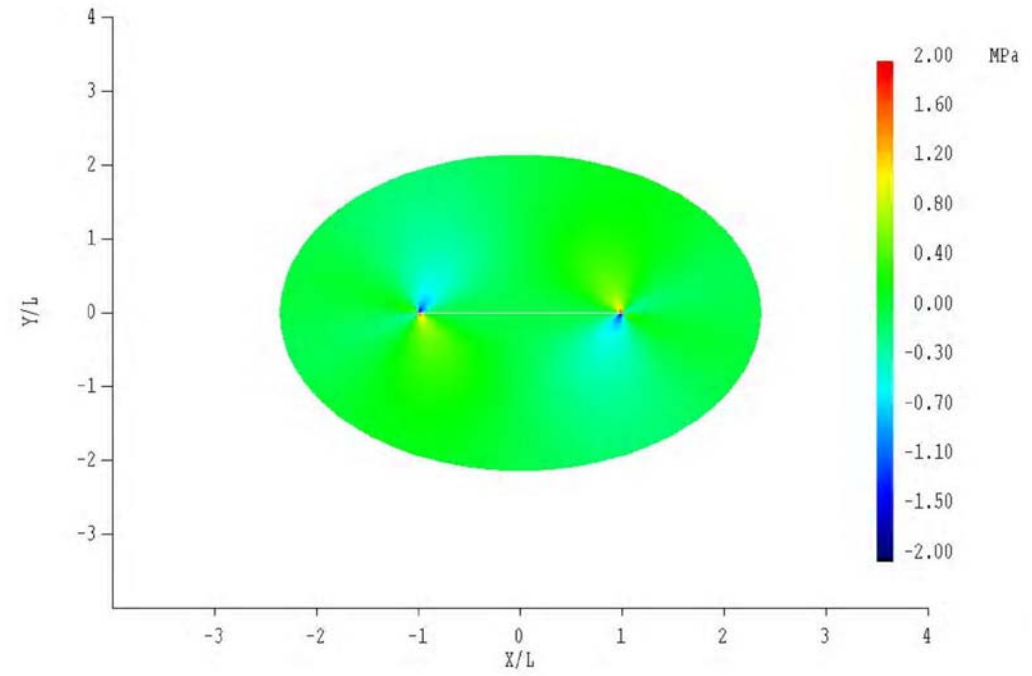

Fig.C.9 Induced Stress around Crack ($\Delta\sigma_{xy}$)

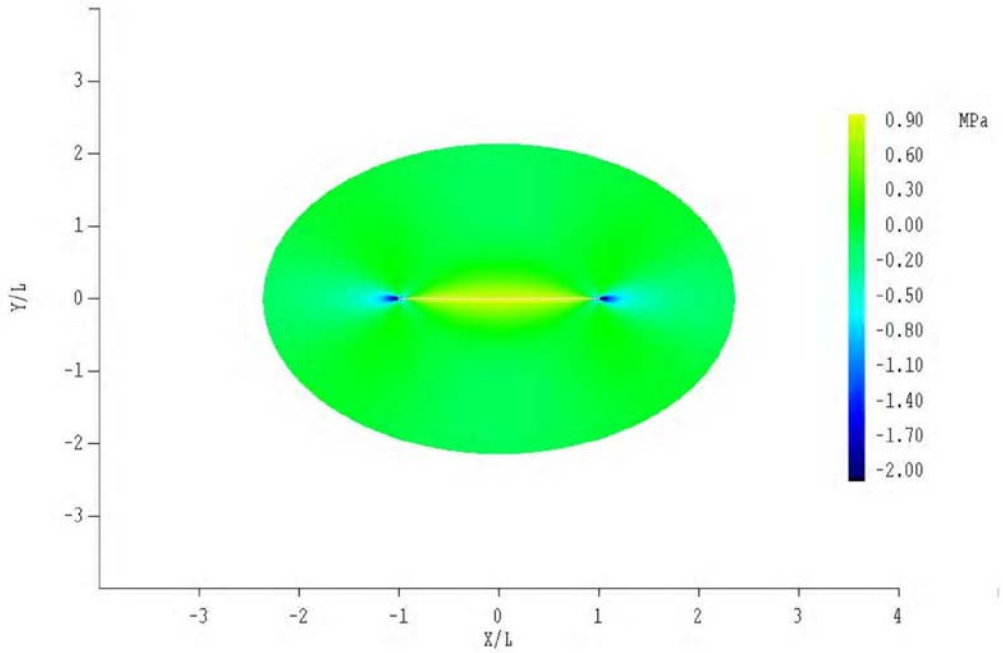

Fig.C.10 Total Stress around Crack (σ_{xx})

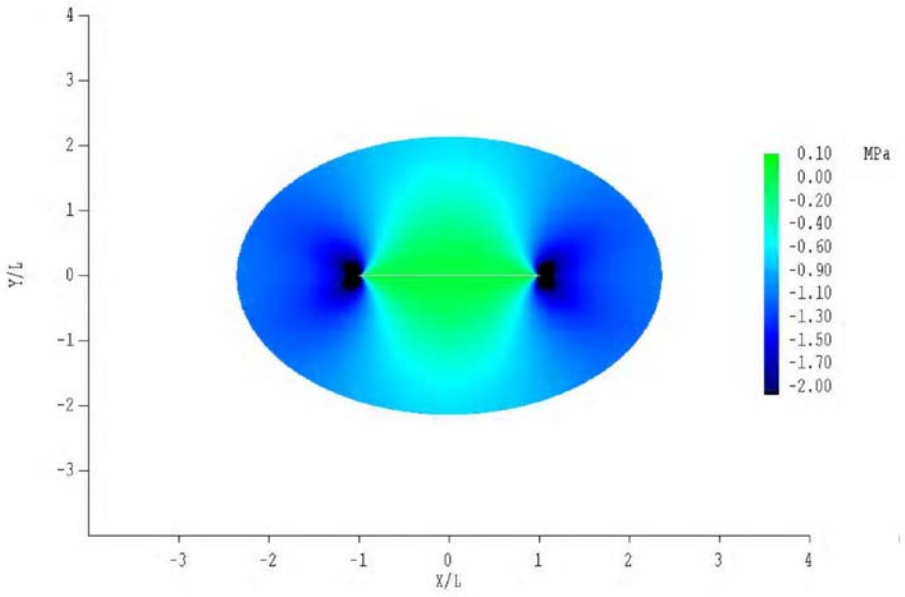

Fig.C.11 Total Stress around Crack (σ_{yy})

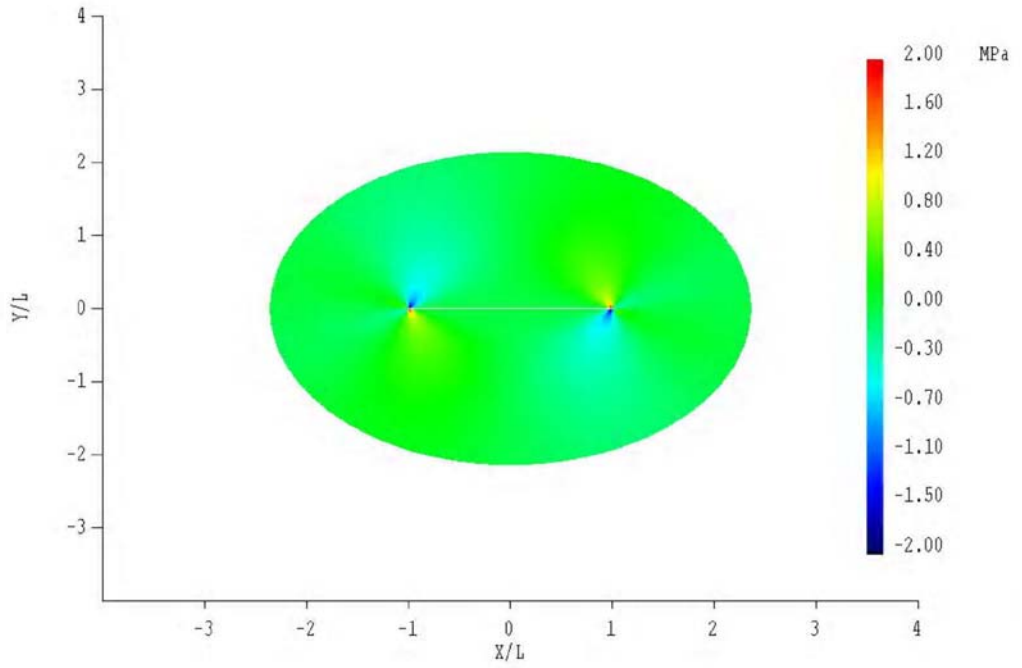

Fig.C.12 Total Stress around Crack (σ_{xy})

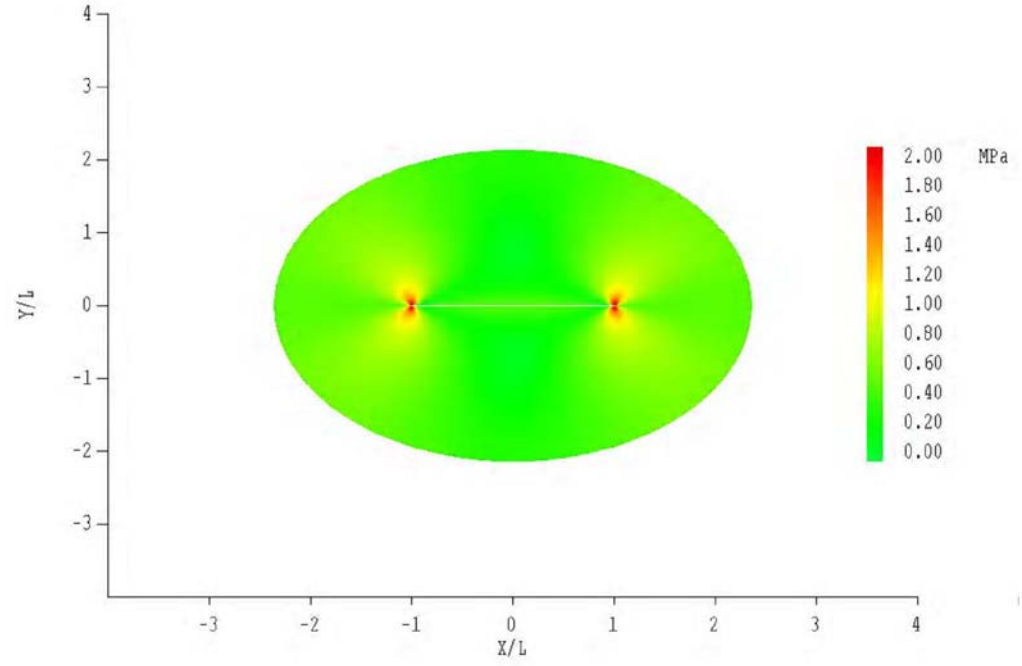

Fig.C.13 Maximum Shear Stress

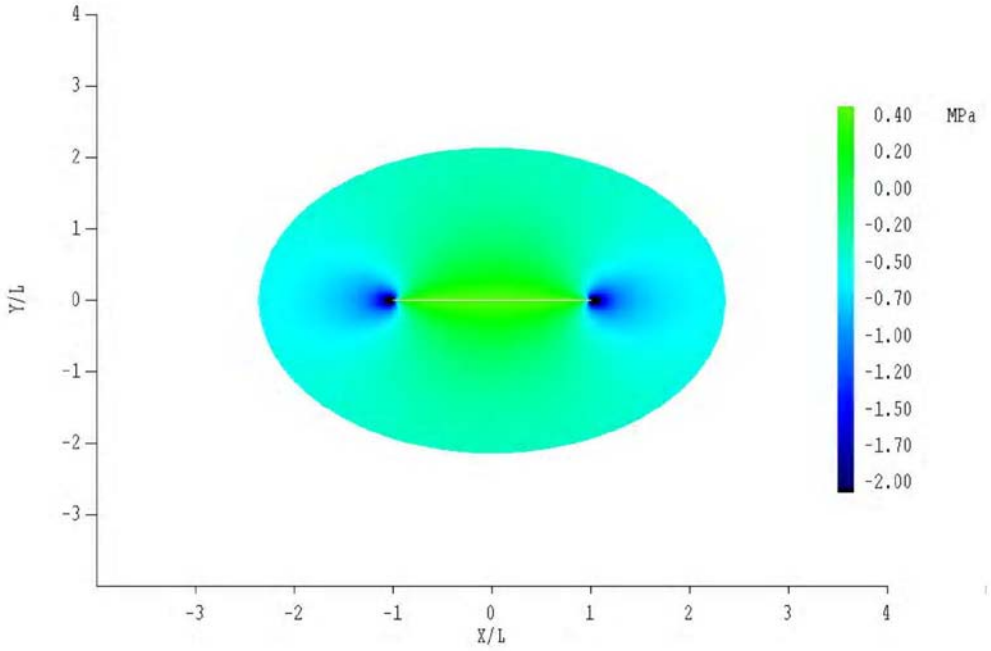

Fig.C.14 Mean Normal Stress

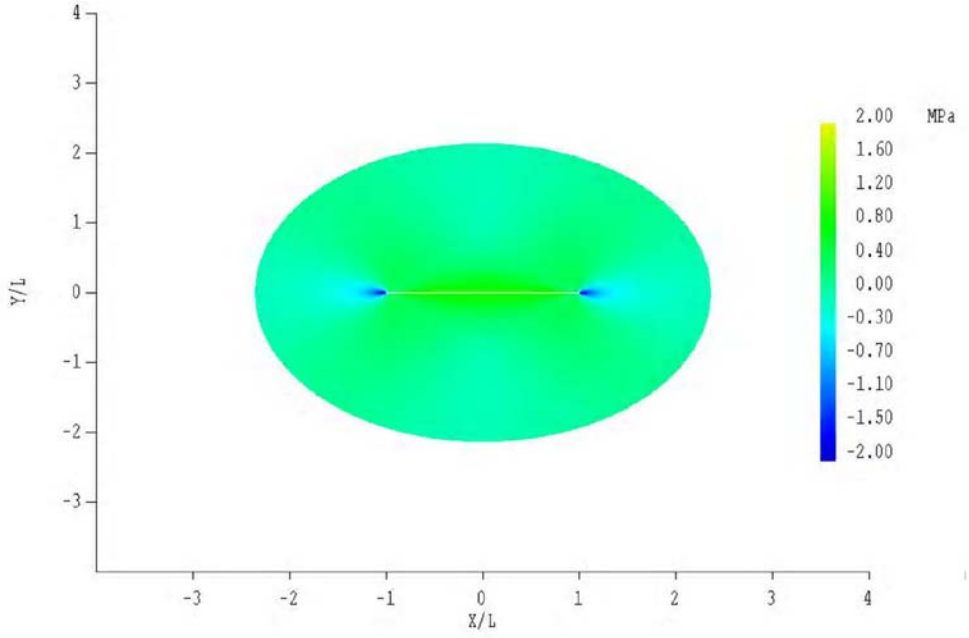

Fig.C.15 Maximum Principal Stress

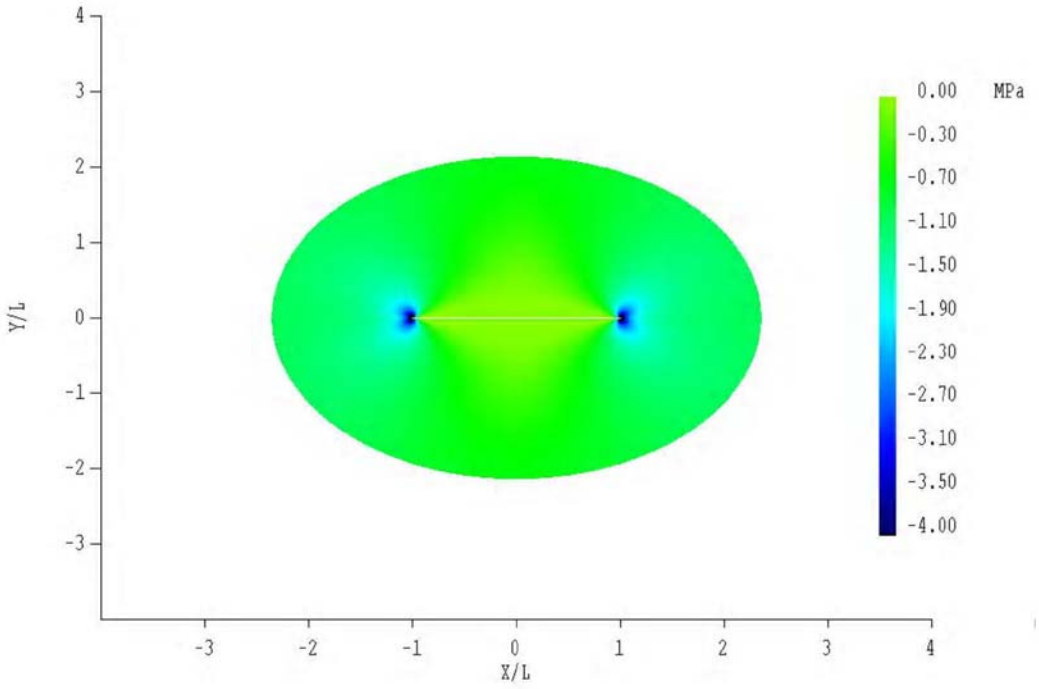

Fig.C.16 Minimum Principal Stress

3) Conclusions:

In this study, we examined the methods used to find the induced stresses by fracture compression, and several special load cases are checked. The unit tension case is calculated and plotted in the report.

The method given by Jaeger and Cook is compared with the method by Pollard and Segall, and both methods give the same results, which illustrated the expressions we deduced from Jaeger and Cook are correct.

The program for fracture compression can be used individually, as well as combined with other programs. It can also be a part in a more complex program.

APPENDIX D

EQUATIONS USED FROM PERKINS AND KONG'S PAPER

1) Calculating Bottom hole Pressure:

$$P_{iwf} = P_R + \Delta P_1 + \Delta P_2 + \Delta P_3 + \overline{\Delta P_f} \quad \text{..... (D.1)}$$

In which:

$$\Delta P_1 = \frac{0.5\times(\mathrm{Ln}(\mathrm{K}\times \mathrm{t}/(\phi\times\mu\times \mathrm{c_t}\times(0.5\times \mathrm{r}^2))+0.80907)}{1-0.5\times(\mathrm{Ln}(\mathrm{K}\times \mathrm{t}/(\phi\times\mu\times \mathrm{c_t}\times(0.5\times \mathrm{r}^2))+0.80907)}(\Delta P_2) \quad \text{..... (D.2)}$$

and

$$P_D(\xi,\eta,t_{DL}) = \frac{P_i - P(\xi,\eta,t)}{P_i - P_{wf}} \quad \text{..... (D.3)}$$

and $\mathrm{P_D} = 0.5\times(\mathrm{Ln}(\mathrm{K}\times \mathrm{t}/(\phi\times\mu\times \mathrm{c_t}\times(0.5\times \mathrm{r}^2))+0.80907)$

In which P_i is the initial reservoir pressure, and P_{wf} is the pressure at the inner boundary, as shown in the plan view of Fig.3.1: the inner boundary is the hot/cold boundary, and the outer boundary is the water/oil boundary.

So, here

$$P_D(\xi,\eta,t_{DL}) = \frac{P_i - P(\xi,\eta,t)}{P_i - P_{wf}} = \frac{\Delta P_1}{\Delta P_1 + \Delta P_2} \quad \text{..... (D.4)}$$

then,

$$\Delta P_1 = \Delta P_2 \times P_D/(1-P_D) = \frac{0.5\times(\mathrm{Ln}(\mathrm{K}\times \mathrm{t}/(\phi\times\mu\times \mathrm{c_t}\times(0.5\times \mathrm{r}^2))+0.80907)}{1-0.5\times(\mathrm{Ln}(\mathrm{K}\times \mathrm{t}/(\phi\times\mu\times \mathrm{c_t}\times(0.5\times \mathrm{r}^2))+0.80907)}(\Delta P_2) \quad \text{(D.5)}$$

in which C_t is the total compressibility. The most reasonable value of r appears to be a_1. However, Kucuk and Brigham (1979.) did not mention a criterion for selection of r

except that it should be large enough; On the other hand, they also provided a different expression for pressure that does not require *r*. namely:

$$P_{wD} = \frac{1}{2}(\ln t_{DL} + 2.19537) \quad \text{..... (D.6)}$$

in which:

$$t_{DL} = \frac{3.6 * 10^{-6} k_o t}{\phi \mu c_t L^2} \quad \text{..... (D.7)}$$

$$\Delta P_1 = \frac{q\mu}{7.2 * 10^{-6} \pi k_o h} P_{wD} \quad \text{..... (D.8)}$$

As will be seen, the results from the previous Eqn. are closer to those of P&G. This might be because ΔP_1 in the latter equation is equal to the sum of ΔP_1, ΔP_2 and ΔP_3, so that the accuracy is less than the separated calculation.

ΔP_2 and ΔP_3 are calculated from the following equations:

$$\Delta P_2 = i_w \mu_w \ln(\frac{a_1 + b_1}{a_0 + b_0}) / (2\pi k k_{rw} h) \quad \text{..... (D.9)}$$

$$\Delta P_3 = i_w \mu_w \ln(\frac{a_0 + b_0}{L_f}) / (2\pi k k_{rw} h) \quad \text{..... (D.10)}$$

$$\Delta \overline{P}_f = 0.00074[\frac{i_w \mu_w L_f E^3}{(1-\upsilon^2)^3 h^4}]^{1/4} \quad \text{..... (D.11)}$$

2) Calculating the semi-axes of the cool region and flooded zone:

$$W_i = Qt \quad \text{..... (D.12)}$$

$$V_{wt} = W_i / (\phi * (1 - S_{or} - S_{wi})) \quad \text{..... (D.13)}$$

$$Vc = \frac{\rho_w C_w W_i}{\rho_{gr} C_{gr} (1-\phi) + \rho_w C_w \phi (1 - S_{or}) + \rho_o C_o \phi S_o r} \quad \text{..... (D.14)}$$

$$F1 = 2*Vc/(\pi*h*L_f{}^2) + 0.5*\sqrt{(\frac{4Vc}{\pi L_f{}^2 h})^2 + 4} \quad \text{..... (D.15)}$$

$$F2 = 2*V_{wt}/(\pi*h*L_f{}^2) + 0.5*\sqrt{(\frac{4V_{wt}}{\pi L_f{}^2 h})^2 + 4} \quad \text{..... (D.16)}$$

$$a_0 = L_f*(\sqrt{F1} + \frac{1}{\sqrt{F1}})/2 \quad \text{..... (D.17)}$$

$$b_0 = L_f*(\sqrt{F1} - \frac{1}{\sqrt{F1}})/2 \quad \text{..... (D.18)}$$

$$a_1 = L_f*(\sqrt{F2} + \frac{1}{\sqrt{F2}})/2 \quad \text{..... (D.19)}$$

$$b_1 = L_f*(\sqrt{F2} - \frac{1}{\sqrt{F2}})/2 \quad \text{..... (D.20)}$$

3) Calculating Fracture Length:

$$P_1 = \sigma_1 + \sqrt{\frac{\pi UE}{2(1-\upsilon^2)r_f}} \quad \text{..... (D.21)}$$

in which:

$$P_1 = P_{iwf} - 3\Delta P_f \quad \text{..... (D.22)}$$

$$\sigma_1 = (\sigma_H)_{\min} + \Delta\sigma_{1T} + \Delta\sigma_{1P} \quad \text{..... (D.23)}$$

in which $\Delta\sigma_{1T}$ and $\Delta\sigma_{1P}$ are calculated from the following equations:

$$\frac{(1-\nu)\Delta\sigma_{1T}}{E\beta\Delta T} = \frac{(b_0/a_0)}{1+(b_0/a_0)} + [\frac{1}{1+(b_0/a_0)}]$$
$$\times(1/\{1+\tfrac{1}{2}[1.45(\frac{h}{2b_0})^{0.9} + 0.35(\frac{h}{2b_0})^2] \quad \text{..... (D.24)}$$
$$\times[1+(\frac{b_0}{a_0})^{0.774}]\})$$

$$\frac{(1-\nu)\Delta\sigma_{1P}}{EJ\Delta P} = \frac{(b_0/a_0)}{1+(b_0/a_0)} + [\frac{1}{1+(b_0/a_0)}]$$
$$\times(1/\{1+[1.45(\frac{h}{2b_0})^{0.9} + 0.35(\frac{h}{2b_0})^2] \quad \text{..... (D.25)}$$
$$\times[1+(1-\frac{b_0}{a_0})^{1.36}]\})$$

$$J = \frac{1-2\upsilon}{E} - \frac{c_{gr}}{3} \quad \text{..... (D.26)}$$

4) The Bisection method for finding L_f is as the following:

Over some interval the function is known to pass through zero because it changes sign. Evaluate the function at the interval's midpoint and examine its sign. Use the midpoint to replace whichever limit that yields the same sign for F(x). After each iteration, the bounds containing the root decrease by a factor of two. If after *n* iterations the root is known to be within an interval of size ε_n, then after the next iteration it will be bracketed within an interval of size

$$\varepsilon_{n+1} = \varepsilon_n / 2 \quad \text{..... (D.27)}$$

Repeat the process until ε_n is less than a small number such as 1.0E-06. The corresponding value of x is the root of the function, i.e. the fracture length L_f.

For the problem at hand the function is *F(x)* =LHS-RHS. To find the root, select L_f=X_1 which makes $F(x_1)<0$ while L_f=X_2 which makes $F(x_2)>0$. A root will be bracketed in the interval (X_1, X_2). In this study, the assumed data are X_1=0.6 and X_2=1.0E04.

VITA

Name:	Jun Ge
Permanent Address:	Harold Vance Department of Petroleum Engineering, 3116 TAMU, College Station, TX 77843-3116
Email Address:	junge78@gmail.com
Education:	Chinese University of Geosciences, WuHan, HuBei, China B.S., Geology, June 2000
	Peking University, Beijing, China M.S., Economic Geology, July 2003
	Texas A&M University, College Station, Texas, USA M.S., Petroleum Engineering, December 2009
Affiliation:	Society of Petroleum Engineers